In compliance with the
Canadian Privacy Legislation
some supporting forms
may have been removed from
this dissertation.

While these forms may be included
in the document page count,
their removal does not represent
any loss of content from the dissertation.

University of Alberta

Ultrafast Carrier Dynamics in Silicon Thin Films Using Visible Pump – Terahertz Probe Experiments

by

©

Kristine P.H. Lui

A thesis submitted to the Faculty of Graduate Studies and Research in partial fulfillment of the requirements for the degree of Doctor of Philosophy.

Department of Physics

Edmonton, Alberta

Fall 2003

Canadä

University of Alberta

Library Release Form

Name of Author:	Kristine P.H. Lui
Title of Thesis:	Ultrafast Carrier Dynamics in Silicon Thin Films Using Visible Pump – Terahertz Probe Experiments
Degree:	Doctor of Philosophy
Year this Degree Granted:	2003

Permission is hereby granted to the University of Alberta Library to reproduce single copies of this thesis and to lend or sell such copies for private, scholarly or scientific research purposes only.

The author reserves all other publication and other rights in association with the copyright in the thesis, and except as hereinbefore provided neither the thesis nor any substantial portion thereof may be printed or otherwise reproduced in any material form whatever without the author's prior written permission.

Canada

July 23, 2003

University of Alberta

Faculty of Graduate Studies and Research

The undersigned certify that they have read, and recommend to the Faculty of Graduate Studies and Research for acceptance, a thesis entitled **Ultrafast Carrier Dynamics in Silicon Thin Films Using Visible Pump – Terahertz Probe Experiments** submitted by **Kristine P.H. Lui** in partial fulfillment of the requirements for the degree of Ph.D.

Dr. Rik Tykwinski

Date: _JULY 9, 2003_

To

Zebra Osmanthus
A tiger without compare

Preface

A Rhyme about Terahertz

Terahertz radiation
in the IR section
is a trillion cycles
per second longitudinal
(300 microns
equals one cycle long).

-- *But how do we make*
IR that doesn't bake?

A dash of bismo-pepto
and lasers femto.
Add a crystal - zinc telleride -
(Careful! Watch your eyes!)
rectified electro-optically
and we have terahertz, magically!

-- *But do we know it's there?*
Patience, friend! Listen here:

For detect we must!
In zinc telleride we trust!
Terahertz rotates **P**.
("Polarisation", jargon-less-ly.)
A femtosecond pulse gate,
arives none too late;
it goes from linear to elliptical
and separates vectorial.
-- *Can we see these two?*
Yes! Photodiodes to the rescue!
Only two are needed;
and their difference is heeded.
A zero difference says,
"Nothing's here! O fooey fuzz!"
Otherwise we can see
our terahertz's burly
amplitude's measure.

-- *Phew! I'm all reassured!*
Now we have pulses far
in the infrared bar.

-- *So what? Who cares?*
I'd rather cuddle teddy bears!

But ho! Just wait!
Your curiosity we'll satiate.
One of the perks
of pulses terahertz
is its energy is weak,
so no major system's tweaked.
Super- and semiconductors galore!
Chemical vibrations, and more!

Now you have a short intro
to the quirky terahertz world.
-- *Yippee! Hurrah! A new wave*
has come this day to save!
Thank you! Thank you!
And now the show's through.

May 2002

Abstract

A terahertz time-domain spectroscopy system was constructed and characterised in the Ultrafast Spectroscopy Laboratory. This system was then used as a probe beam for pump-probe experiments to help elucidate physics of carrier dynamics in silicon-on-sapphire systems. Specifically, ion-implanted silicon thin films on sapphire substrates and an amorphous silicon thin film on sapphire were investigated. Results from these studies point to the presence of a single carrier relaxation channel in silicon thin film systems. Preliminary 400 nm pump – THz probe experiments have also been performed on silicon nanocrystals in a sapphire substrate. Using a digital filter to mimic convolution issues with the data, a new analysis technique has been shown viable for use in this relatively new laboratory group. Furthermore, the terahertz system is now ready for use not only as a probe beam in a pump-probe experimental configuration, but has also been shown to be a useful far-infrared linear spectroscopy source.

Acknowledgements

Table of Contents

TABLE OF CONTENTS

List of Tables

LIST OF TABLES

List of Figures

LIST OF FIGURES

LIST OF FIGURES

LIST OF FIGURES

Chapter 1

Introduction

1.1 Terahertz Radiation

Many materials have interesting resonant frequencies in the far-infrared regime. These include vibrational levels in molecules, phonon energies in semiconductors, and Cooper pair binding energies in superconductors. Strong coherent sources of far-infrared (FIR) radiation have long been sought to study these materials. The advent of the free-electron laser (FEL) to generate FIR coherently propelled experiments to a new radiation regime [3]. Free electron lasers use a beam of relativistic electrons to generate coherent radiation in an alternating magnetic field [4]. The wavelength of this radiation is dependent on the amplitude and frequency of the applied magnetic field. FELs have the advantage of wavelength tunability and high peak power. However, these systems were generally cumbersome and difficult to use.

Technology was developed to readily produce terahertz pulses (1 THz = 10^{12} Hz) in the 1980's, and made this wavelength regime accessible to anyone interested in using coherent FIR pulses. Today, researchers are studying THz imaging as a tool to aid security and medical issues. More fundamental research

uses THz pulses in pump-probe experiments as a probe of material properties in superconductors and semiconductors, for example. THz pulses are advantageous as they allow for contact-free transient experiments. Furthermore, THz pulses have a broad bandwidth.

THz imaging acquires images of objects through visibly opaque materials. THz imaging can exploit phase shifts of the THz beam at different points of an object [5]; watermarks on various international currencies were imaged using phase shifts in THz pulses [6]. Other examples include the imaging of business cards inside envelopes and integrated circuits inside plastic chips [7]. Alternatively, amplitude transmission of the THz beam can be monitored to image organic materials. For instance, the changes in water content of a dry versus a newly cut leaf [7], and locations of tooth decay for dental purposes [8] have been identified using THz pulses.

In general, THz pulses are sub-picosecond pulses at full-width, half-maximum (FWHM) and with a bandwidth of a few THz, centred near 1 THz. THz emission can be thought of as resulting either from a surge in current, $E_{THz} \propto \partial J/\partial t$, or from changes in polarisation, $E_{THz} \propto \partial^2 P/\partial t^2$. The current surge method was introduced by Auston et. al. [9] as radiation from a Hertzian dipole, and is often referred to as an Auston switch. The transient polarisation method exploits optical rectification (OR) in a non-centro-symmetric crystal. Both the current surge method and the optical rectification method can be exploited to generate and to detect THz pulses. In fact, $\partial J/\partial t$ has been used to explain far infrared (FIR) emission from biased, large aperture sources and intrinsic surface depletion fields in addition to photoconductive dipole switches [10].

Femtosecond laser pulses are required for THz generation and detection. In the current surge method, the femtosecond beam creates free carriers in the semiconductor substrate which travel quickly across a biased transmission line

patterned on the semiconductor. Optical rectification of femtosecond pulses in a nonlinear crystal can also generate THz pulses. THz detection in both methods exploits analogous processes. In either case, the time delay between the arrival of the THz pulse and the arrival of the femtosecond detection pulse can be controlled so as to measure the entirety of the THz pulse shape. This is achievable only because the processes governing the detection are nearly instantaneous (very short when compared to the THz pulse width). A detailed discussion of THz generation and detection techniques is given in Chapter 2.

THz pulses have shown to be very useful for linear spectroscopy in the far-infrared regime. Finding the complex index of refraction, $\kappa = n + ik$, for the far-infrared range before the advent of easily-produced THz pulses required the use of Kramers-Kronig relations [11],

$$n(\omega) = 1 + P \int_{-\infty}^{+\infty} \frac{d\omega'}{\pi} \frac{k(\omega')}{\omega' - \omega}, k(\omega) = -P \int_{-\infty}^{+\infty} \frac{d\omega'}{\pi} \frac{n(\omega') - 1}{\omega' - \omega}. \tag{1.1}$$

Note Equations 1.1 are entangled (where the P refers to a principal value integral). To find $\kappa(\omega)$, one must know one of the above equations, and the reflectivity at all wavelengths [11],

$$r(\omega) = \left| \frac{1 - \kappa}{1 + \kappa} \right|^2. \tag{1.2}$$

For a sample with no absorption, the transmissivity is simply

$$t(\omega) = 1 - r(\omega). \tag{1.3}$$

Measuring the wavelength-dependent index of refraction required much transmissivity data taken with a large range of wavelengths. THz linear spectroscopy

is much simpler in that detection is coherent; that is, amplitude and phase information are acquired simultaneously. Kramers-Kronig relations are then not needed, making index of refraction much simpler to gather. Indeed, many groups have reported dielectric functions, indices of refraction, and complex conductivities in the far-infrared regime for many materials.

Complex dielectric functions and frequency-dependent conductivities can be measured simultaneously because of the coherent detection afforded by THz time-domain spectroscopy (THz-TDS). For example, the complex dielectric function was measured for $CdTe$ thin films between 0.2 and 6 THz [12], Si, $GaAs$ and Ge as well as various substrate materials (such as sapphire, quartz and fused silica) [13]. Complex conductivities of various superconductors have also been measured using THz-TDS, including Nb [14] and Pb [15]. In addition, THz linear spectroscopy has been used to elucidate dynamic properties such as photoconductivity in $InGaAs$ [16] and carrier dynamics of low-temperature-grown $GaAs$ [17]. An indepth review of THz-TDS is given by Nuss and Orenstein [18].

THz pulses are often used as probe beams in pump-probe experiments to study dynamical processes. Because of their low energies, THz pulses are sensitive to the conductivity in the sample; they are ideal for examining ultrafast carrier dynamics in materials. Furthermore, this is a non-contact method of measuring the transient conductivity in samples, eliminating complications arising from deposited contacts.

The next few sections give some background on the Drude theory of metals, the silicon-on-sapphire systems to be investigated, and pump-probe experiments.

1.2 Drude Theory

Metals are a special class of solids, whose properties play an important role in the understanding of some transient properties. P. Drude built a kinetic

theory to describe transport in metals [11], modelling the metal lattice as a set of stationary ion cores surrounded by a dilute electron gas. The basic Drude theory assumes no interaction between an electron and any other electrons nor with any ion core. Furthermore, electron-electron collisions are considered to be instantaneous, while the time between collisions, τ_d, variously called the damping time, collision time, scattering time or the mean free time, is considered to be independent of the electrons position and velocity.

From Ohm's Law, the current, $\vec{j}$, in a metal due to an applied electric field, $\vec{E}$, is

$$\vec{j} = \left(\frac{ne^2\tau_d}{m}\right) \vec{E}. \tag{1.4}$$

This defines the conductivity, σ, of the material:

$$\vec{j} = \sigma\vec{E} \tag{1.5}$$

where σ is

$$\sigma_o = \frac{ne^2\tau_d}{m}. \tag{1.6}$$

The direct current conductivity σ_o is proportional to the number of carriers, n, the fundamental electric charge e, and the relaxation time τ_d, while it is inversely proportional to the electron mass m. The discussion here focusses on electrons, but can be generalised to holes also. The electron mobility in the material, $\mu = e\tau_d/m$, can also be used to define the direct current conductivity,

$$\sigma_o = ne\mu. \tag{1.7}$$

In a pure metal, electron-electron scattering is the only contribution to the damping time. However, should lattice defects or impurities be introduced into the

material, τ_d decreases, hence the electron's mobility μ also decreases, thereby lowering the electrical conductivity of the material.

Eq. 1.6 and 1.7 refer to the frequency-independent, or direct current (DC) conductivity. Accounting for frequency-dependence, the alternating current (AC) conductivity, $\sigma(\omega)$, is

$$\sigma(\omega) = \frac{\sigma_o}{1 - i\omega\tau}. \tag{1.8}$$

The AC electrical conductivity contains both real and imaginary parts in general. If $\omega\tau \ll 1$, then $\sigma(\omega) \rightarrow \sigma_o$, and we recover the DC electrical conductivity, where σ is entirely real. Note that a generalised Drude model, where

$$\sigma(\omega) = \frac{\sigma_o}{\left(1 - (i\omega\tau)^{1-\alpha}\right)^\beta}, \tag{1.9}$$

has been used to describe metallic-like systems [19, 20]. In Eq. 1.9, $\alpha = 0$ reduces the generalised Drude model to the Cole-Davidson Model, while $\beta = 1$ recovers the Cole-Cole Model. Both these conditions, $\alpha = 0$ and $\beta = 1$, reduces Eq. 1.9 to the simple Drude Model.

The dielectric function, $\epsilon(\omega)$, is related to the AC conductivity by

$$\epsilon(\omega) = 1 + \frac{4\pi i \sigma}{\omega}, \tag{1.10}$$

and is also related to the index of refraction, κ,

$$\kappa = \sqrt{\epsilon} = n + ik. \tag{1.11}$$

The dieletric function for $\omega\tau \gg 1$ can be written as

$$\epsilon(\omega) = 1 - \omega_p^2/\omega^2, \tag{1.12}$$

where

$$\omega_p^2 = \frac{4\pi n e^2}{m} \tag{1.13}$$

defines the plasma frequency.

While the Drude model describes metals fairly well, it generally cannot be applied to other materials. However, semiconductors can be made transiently conductive enough to be described by the Drude model. Possible methods for the presence of free carriers in semiconductors include thermal excitation, electrical injection via transmission lines, and photoexcitation, where a laser pulse excites carriers high into the conduction band. As injected free carriers in a semiconductor relax back to their equilibrium state, the Drude model can be used to describe their mobility.

In the remainder of this chapter, the concept of a pump-probe experiment will be outlined. In these experiments, insulating semiconductor materials, such as the silicon-on-sapphire systems described in Section 1.3, are made momentarily metallic through the photogeneration of charge carriers when an intense laser pulse pumps charge carriers to the conduction band. A weaker (probe) pulse examines the state of these charge carriers at some time after excitation. By varying the time delay between pump and probe pulses, a dynamic picture of carrier relaxation processes in the sample is obtained. In other words, the increase in charge carriers increases the plasma frequency, ω_p, sufficiently to reduce the transmission of the probe beam. By monitoring the time-dependence of the probe beam transmission, information on characteristic carrier relaxation time constants and carrier mobility values will be elucidated. In the experiments described here, the probe beam is a short pulse in the far-infrared regime of the electromagnetic spectrum. It will be referred to as the *terahertz beam* (for its central frequency is 10^{12} Hz), and is described in detail in Section 1.1. A short

review of visible pump – terahertz probe experiments is given in Section 1.4.

1.3 Silicon-on-Sapphire Systems

Lattice-damaged silicon-on-insulator continues to be of interest for its fast relaxation mechanisms and high mobility values. Defects present in the damaged lattice structure trap mobile charge carriers, decreasing the relaxation times of these carriers. Hopping between trapped states is expected to be the dominant transport mechanism [21, 22]. However, defects can also decrease the carrier mobility of the material. Optimization involves a compromise between fast relaxation time and high carrier mobility.

1.3.1 Radiation-Damaged Silicon-on-Sapphire

Ion implantation is a versatile method by which to incorporate lattice defects into a material since virtually any atom can be implanted into any other material. One can imagine that excessive damage would amorphize a thin film. Ion-implanted, or radiation-damaged (RD) silicon-on-sapphire consists of a thin film of crystalline Si (c-Si) on a crystalline sapphire substrate. The thin film is then bombarded with ions in doses on the order of $10^{12} - 10^{16}$ cm^{-2} and energies on the order of 100 keV. Implantation of an ion with several energies aid in keeping the distribution of lattice damage uniform within the depth of the film.

Liu et. al. [23] demonstrated the amorphization of crystalline silicon thin films with Si^+ implantation at doses greater than 10^{14} cm^{-2}, while no amorphization could be attained for any dose of B^+ implantation. Since the atomic mass of O is between that of Si and B, amorphization of Si with O^+ implantation requires a larger dose than amorphization with Si^+ implantation. Indeed, Doany et. al. [24] reported that relaxation time constants saturated at 0.6 ps (indicative of

amorphization) when the O^+ implantation dose exceeded 10^{15} cm^{-2}.

1.3.2 Amorphous Silicon

Amorphous silicon (a-Si) has generated much interest in recent decades, both for its potential application to fast-switching devices (see for example Ref. [25]) and for its use in solar cells [26]. Several methods used to produce a-Si samples include self-implantation into crystalline silicon, vapor deposition, sputtering, and glow discharge [27]. Hydrogenated amorphous silicon (a-Si:H), prepared via glow discharge of silane gas, has been extensively studied. For recent examples, see Refs. [28–32]. Less work, however, has been devoted to the study of carrier dynamics in non-hydrogenated amorphous silicon.

In an a-Si film, silicon atoms are covalently bonded in a continuous random network. Both shallow traps (extended band tail states) and deep traps (defects such as dangling bonds) may be present in amorphous films. Shallow traps, while playing a dominant role in photoluminescence [33], have smaller carrier capture cross sections, and are expected to be unimportant in picosecond-scale photoconductivity experiments. Although the average density in a-Si is similar to that of c-Si, large voids in the film (resembling holes in Swiss cheese) leave unsatisfied silicon bonds, giving rise to localized, deep trap states within the band gap. These are vacancy defects [34] and electron spin resonance measurements indicate these types of defect densities are on the order of $10^{19} - 10^{20}$ cm^{-3} [35]. In hydrogenated a-Si, H^+ fill these voids and passivate the dangling bonds, thereby reducing the number of localized deep trap states and increasing relaxation time constants.

1.4   Visible Pump – THz Probe Experiments

Visible pump beams and THz probe beams have been used in pump-probe experiments to study carrier dynamics in a wide variety of materials [36], including semiconductors, superconductors, quantum wells, and nanocrystals. Details of such experiments would require an entire book, but I will outline a few examples here.

Many groups have studied *GaAs* using visible pump – THz probe experiments. One of the first was used to demonstrate the viability of a THz probe, and found the conductivity risetime constant to be $\sim$1.5 ps when 6×10^{18} cm^{-3} carriers were excited by a 630 nm pump beam [37]. Further studies showed a fast risetime, followed by a slower risetime; this gradual risetime was attributed to an increased carrier conductivity as carriers settled from L and X valleys to the higher mobility Γ valley [38,39].

Low-temperature grown *GaAs* is often deposited by molecular beam epitaxy, where the substrate is kept between 180 and 300ºC during sample deposition [20]. Annealing the samples precipitates *As* clusters and increases the carrier mobility from several cm^2/Vs by two orders of magnitude. The relaxation time constant is reduced from the bulk *GaAs* wafer value to 2.1 ps picoseconds [20]. Furthermore, Beard *et. al.* [19] noted the frequency-dependent conductivity was initially influenced by phonons, settling towards Drude-like behaviour within 3 ps of the initial pump pulse arrival at the sample.

Visible pump – THz probe experiments have also been conducted on semi-insulating *GaAs* (resistivity greater than 10^8 Ω·cm) [40]. Here, the transient complex permittivity was calculated using an iterative method. Schall and Uhd Jepsen [40] showed an apparent negative time shift of the THz pulse in the excited sample due to the frequency-dependent transmission and a phase shift at the air-*GaAs* interface.

In addition to $GaAs$, visible pump – THz probe experiments have been conducted on semiconductors such as InP [39], $ZnTe$ and $CdTe$ [41]. Groeneveld and Grischkowsky conducted visible pump – THz probe experiments on $GaAs/AlGaAs$ quantum wells [42], showing free electron decay to the lowest excitonic state within 100-150 ps. Excitons, on the other hand, have lifetimes on the order of 250 ps in these quantum well systems.

Because of their sensitivity to low-energy dynamics, THz probes are quite useful in studying dynamics in superconductors. In particular, the induced changes in the real and imaginary conductivity can be measured, allowing for the elucidation of both quasiparticle and superconducting pair dynamics [43]. For example, the temporal dependence in complex conductivity and the dynamical influence of the superconducting gap and the pseudogap were studied in the high-transition-temperature superconductors $YBa_2Cu_3O_{7-\delta}$ [44, 45] and $Y_{1-x}Pr_xBa_2Cu_3O_7$ [46]. An excellent review of optical pump – THz probe studies of ultrafast dynamics in superconductors is given in Ref. [43].

In addition to semiconductor and superconductor systems, visible pump – THz probe experiments have been performed on an organic molecular crystal [47]. Debate over the nature of charge transport and the source of primary photoexitations in these systems continues. In Ref. [47], optical pump – THz probe experiments were conducted on a functionalised pentacene molecule in the Ultrafast Spectroscopy Laboratory, where a 800 nm pump beam was used to photoexcite the pentancene, while a THz beam was used to probe the carrier dynamics of the system at various temeratures. This work suggested that the photogeneration of mobile carriers is the primary source of photoconduction.

This thesis describes the first pump-probe study of carrier dynamics in radiation-damaged silicon-on-sapphire (RD-SOS) and amorphous silicon (a-Si) thin films

using a 400 nm pump pulse and a THz probe beam [1, 48, 49]. The characteristic relaxation time constants in the three samples are measured for various temperatures and with various pump fluences. Using a Drude model, the effective free carrier mobility for all three samples are extracted and the transient carrier density is investigated.

Chapter 2

Terahertz Generation and Detection

First, let's take a brief foray into THz generation and detection methods. Photoconductive (Auston) switches will be described first, followed by a more comprehensive discussion on optical rectification, the method used in the Ultrafast Spectroscopy Laboratory. Specifically, the nonlinear optical effect, optical rectification, which generates the THz field, will be described, as well as electro-optic sampling, which is used to detect THz pulses using non-centrosymmetric crystals.

2.1 Auston Switches

2.1.1 Basic Mechanism for Generation and Detection

Devices using the current surge method for generating THz pulses, $E_{THz} \propto \partial J/\partial t$, are known as "Auston switches", named after D.H. Auston [9], or generically as "photoconductive switches". An Auston switch is shown in Figure 2.1. An applied electric field across patterned transmission lines on a semiconductor substrate accelectrates photogenerated charge carriers. This is the current surge

which results in an electromagnetic pulse in the THz region of the spectrum. Typically, the bias voltage, V, is on the order of 100 V, and the separation between the electrodes, d, is on the order of tens of microns. Many semiconductors have been used as substrates for transmission lines, including silicon-on-sapphire, low-temperature and semi-insulating $GaAs$, doped $GaAs$, and InP [50].
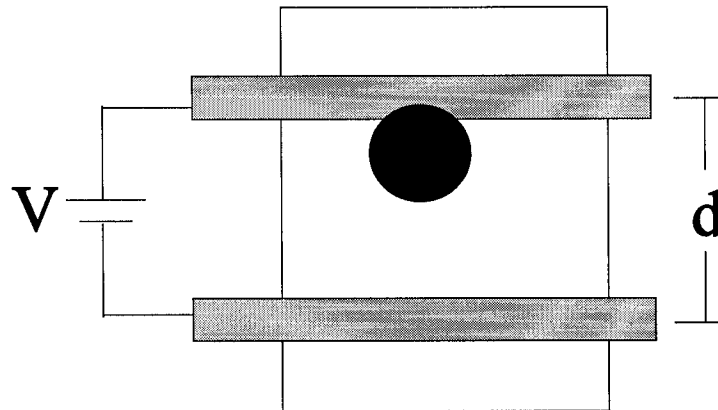
Figure 2.1:   Schematic of an Auston Switch THz generator. Transmission lines (shown as grey horizontal bars) are biased with an external potential. A femtosecond laser pulse (black circle) is focussed near the anode, generating free carriers in the substrate, and allowing for a sudden surge in current across the biased electrodes. Typical bias voltages, V, are on the order of 100s and 1000s of volts for traditional and large aperture Auston switches, respectively. The separation between the electrodes, d, is typically several 100s of microns for traditional THz sources, and several millimetres for large aperture sources.

The femtosecond laser beam is usually focused to create a larger current during the surge. This required a small electrode spacing, and caused the emitted THz beam to diverge. Measured divergences of 100 mrad [25] and 25 mrad [51] have been reported. The THz beam is collected by a truncated spherical semi-

conductor (usually Si) lens on the backface of the transmission line.

Detection of the THz beam is achieved with the reverse mechanism: the incoming THz pulse creates a potential across the detection transmission line. A femtosecond gating pulse is again used to generate free carriers on the transmission line substrate. Since the duration of the THz pulse is much longer than the gating femtosecond pulse, the THz field on the detection transmission line is effectively static (dc field). Thus the generated free carriers are moved across the transmission line; this resultant current (proportional to the THz electric field) is measured. A typical system incorporating Auston Switches for THz generation and detection is shown in Figure 2.2.

2.1.2 Improvements to the Basic Auston Switch

The first switches demonstrated the production of short microwave [52] and electrical [53] pulses using biased semiconductor gates. Several years later a microwave Auston switch was measured to emit coherent pulses with a FWHM of 2.8 ps [54], where a gated detector (in the form of a thin Ge slab which could be made transmissive in the microwave when excited with a laser pulse) had been used. The microwave Auston switch was used as a short probe of carrier dynamics in Cr-doped $GaAs$ in a contact-free measurement.

Improvements in transmission line patterning techniques and faster semiconductor substrates lead to shorter EM pulses emitted from Auston switches, and thus to wider bandwidths. The first THz emission from a photoconductive switch was also achieved by Auston [9].

Further experimentation with Auston switches have shown an enhanced THz emission when the laser pulse is focused near the anode of the biased transmission lines [50]. Possibly this is due to a trap-enhanced electric field present near the anode. The THz intensity is increased when pointed anodes are used, where the
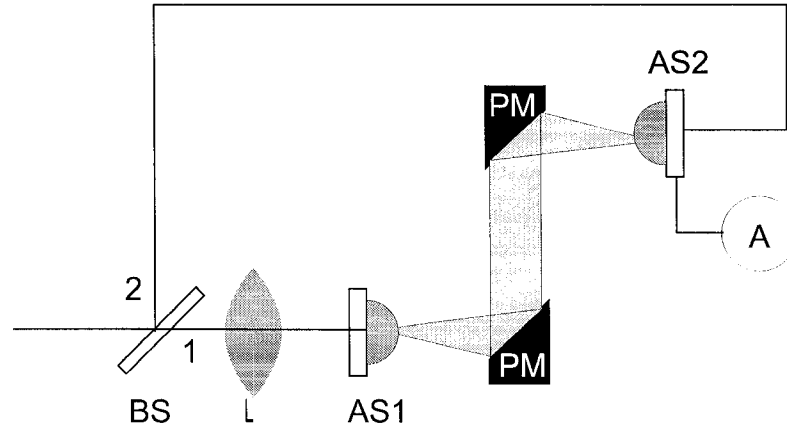
Figure 2.2: THz generator and detector using Auston switches. BS: Beam splitter, L: Lens, AS1: Auston switch THz generator, PM: Parabolic Mirror, AS2: Auston switch THz detector, A: ammeter. Beam 1 photogenerates charge carriers in AS1, while beam 2 detects the THz emission at AS2. The Auston switches each have a truncated spherical silicon lens for collimation of the THz beam. The THz pulse applies an electric field on the switch detector when a femtosecond pulse creates free carriers on the switch substrate. The current measured across the detector electrodes is proportional to the THz electric field.

electric field experiences a singularity near this point [50].

McGowan and Grischkowsky showed the existence of both near-field and far-field THz emission when using a silicon-on-sapphire photoconductive switch [55]. In fact, there are two near-field components: one in the air and one along the surface of the substrate. Only the far-field emission is freely propagating, however.

Using a GaAs-on-silicon receiver, a higher bandwidth emission (5 THz) was demonstrated [56]. This novel material was shown to have a short carrier lifetime of 3 ps superimposed on an unquantified long relaxation time constant.

In the past decade, the use of *large aperture* Auston switches has been more commonplace. In these switches, the gap in the transmission line is on a macroscopic scale, typically on the order of several millimetres. The femtosecond charging beam need not be focused onto the semiconductor substrate; neither does the emitted THz beam need much collimation, as the emitted EM radiation is mainly contained about a small cone in the forward direction collinear with that of the incident femtosecond beam. This makes for easier optics alignment as compared with the traditional Auston switch THz sources, as the large aperture source can be removed temporarily from the setup, and the propagation of the femtosecond pulse will follow closely to that of the emitted THz pulse. However, in order to achieve similar electric fields as compared with traditional Auston switch sources, high voltage (typically 10^3 V) is needed to bias the large aperture switches.

2.2 Optical Rectification and Electro-optic Detection

2.2.1 Optical Rectification

Optical rectification (OR) is a specific case of difference frequency generation (DFG). In DFG, different frequencies present in a short laser pulse can beat together, yielding low-frequency modes. In fact, OR of femtosecond laser pulses can span from nearly dc to mid-infrared wavelengths [57].

OR was first observed in 1962 by Bass [58] with the excitation of KDP and KD_2P with a ruby laser. DC signals of 200 μV to 1 mV were measured and attributed to a net time average of polarization within the crystal. Optical rectification in $LiTaO_3$ was first described in 1984 [59] in terms of non-classical Čerenkov radiation. In 1992, Chuang et. al. [60] proposed a model to explain

measurements of far-infrared emission resulting from OR. Furthermore, they show that the modulation of FIR intensity with sample orientation is further evidence for a $\chi^{(2)}$ process; such a phenomenon could not be readily explained in a current surge picture.

Consider that the polarisation, P, is related to the applied electric field, E, by the susceptibility, χ, and the permittivity of free space, ϵ_o:

$$P = \epsilon_o \chi E. \tag{2.1}$$

Eq. 2.1 can be expanded in powers of E if the applied electric field is not too large, giving:

$$P = \epsilon_o[\chi^{(1)}E + \chi^{(2)}E^2 + \chi^{(3)}E^3 + ...]. \tag{2.2}$$

Allowing for an oscillating applied field, $E(\omega) = E_o cos(\omega t)$, and using trigonometric identities $cos^2\theta = (1 + cos2\theta)/2$ and $cos^3\theta = (cos3\theta + 3cos\theta)/4$, the polarisability can be written as:

$$
\begin{aligned}
P = \ & \epsilon_o \chi^{(2)} E_o^2/2 \\
& + \epsilon_o(\chi^{(1)} + \frac{3}{4}\chi^{(3)} E_o^2)E_o cos(\omega t) \\
& + \epsilon_o \chi^{(2)} \frac{E_o^2}{2} cos(2\omega t) \\
& + \epsilon_o \chi^{(3)} E_o^3 cos(3\omega t) + \ldots .
\end{aligned}
\tag{2.3}
$$

The first term in Eq. 2.3 describes OR; note the dependence on the applied intensity E_o^2. The second term in Eq. 2.3 contains the applied field frequency, and describes processes such as the nonlinear index of refraction, self-phase modulation, and self-focussing. The third and fourth terms in Eq. 2.3 contain twice and thrice the applied field frequency ω, and respectively describe second harmonic generation and third harmonic generation.

Since OR is proportional to $\chi^{(2)}$, a non-centro-symmetric crystal is necessary to produce this phenomenon. The THz electric field is emitted due to the change in polarisation within the crystal, $E_{THz} \propto \partial^2 P/\partial t^2$. In Eq. 2.3, the applied electric field amplitude is time-dependent, hence the emitted THz field appears as a pulse in time.

THz pulses emitted with this method are collinear with the THz-generation femtosecond pulse; a normal incidence arrangment makes for easy alignment of ensuing optics. Whether the freely-propagating THz pulse was emitted from the bulk or the surface of a non-centrosymmetric crystal was debated for several years [15], and resolved in 1995 as originating from the bulk of the crystal [61].

While the second order nonlinearlity $\chi^{(2)}$ is the main contributor to THz emission, there is experimental evidence for contributions from higher nonlinearities under certain conditions and in some materials. For example, $LiTaO_3$ was shown to emit THz radiation through a $\chi^{(3)}$ process [38, 59].

2.2.2 Electro-optic Sampling

Electro-optic sampling (EOS) (also known as electro-optic detection) is the reverse process of OR. The THz electric field includes a transient birefringence in a non-linear crystal. If the crystal is probed by a short, weak femtosecond laser pulse, the induced birefringence can be measured. Since the induced birefringence is proportional to the THz electric field, and the femtosecond pulse is much shorter than the THz pulse, the entire THz pulse shape can be mapped out by varying the time delay between the two pulses.

In particular, EOS measures phase modulation using ellipsometry by passing the gating pulse through a nonlinear crystal, a quarter wave plate, and a Wollaston prism [62]. The $\lambda/4$-plate gives a $\pi/2$ phase delay, and is often referred to as a "compensator" for this reason. The compensator provides an optical bias

which linearises the detection response in the EOS crystal. (Some scattering from the EOS crystal remains after the compensator, indicating the random phase of the scattered light.) The Wollaston polariser separates the intensities of the two components of the ensuing elliptically polarised light. If the two in-coming field components, E_x and E_y, are given by

$$E_x(\omega) = a_o(\omega)cos[k(\omega)z - \omega t] \tag{2.4}$$

$$E_y(\omega) = a_o(\omega)cos[k(\omega)z - \omega t + \phi(\omega)], \tag{2.5}$$

where $\phi(\omega)$ is the dephasing, then after the $\lambda/4$-plate the major $a(\omega)$ and minor $b(\omega)$ axes of the polarisation ellipse are

$$a(\omega) = a_o(\omega)[1 + \frac{1}{2}\phi(\omega)]$$

$$b(\omega) = a_o(\omega)[1 - \frac{1}{2}\phi(\omega)]. \tag{2.6}$$

The difference in polarisation intensities, $(A-B) = 1/2\epsilon_o c \int_0^{+\infty}(|a(\omega)|^2-|b(\omega)|^2)d\omega$, is measured after the Wollaston prism, and the difference signal is thus [63]

$$A - B = \epsilon_o cRe\left[\int_0^{+\infty}|a_o(\omega)|^2\phi(\omega)d\omega\right]. \tag{2.7}$$

Hence the detection of $(A - B)$ gives both amplitude, $|a_o(\omega)|$, and phase, $\phi(\omega)$, information. Noise due to the random phase of the scattered light in the EOS crystal is cancelled when balanced detection as described here is used. A typical THz setup using OR and EOS in a nonlinear crystal is depicted in Figure 2.3.

A detailed study of EOS has been conducted [63]. While these results were specific to detection via a $ZnTe$ crystal, they can be generalised to other EOS systems. It was found that the crystal can affect the measured shape and frequency spectrum of the THz pulse. In particular, three spectral filters were
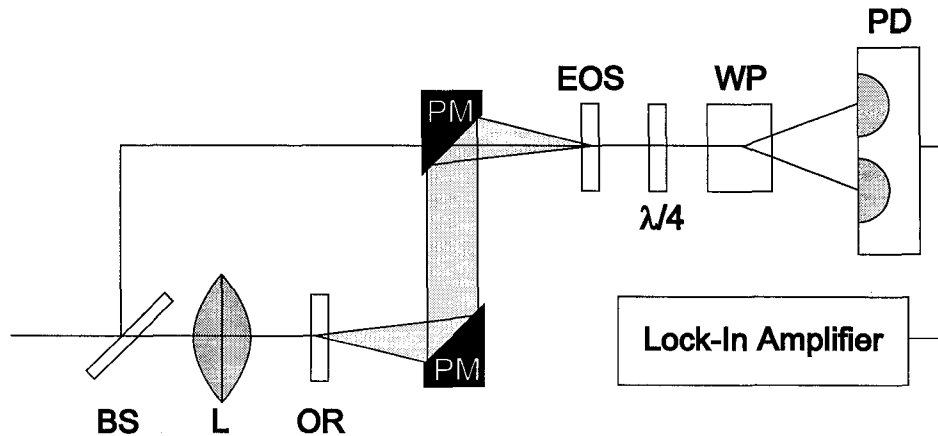
Figure 2.3: Layout for THz generation and detection with optical rectification and electro-optic sampling. BS: beamsplitter, L: bi-convex lens, OR: nonlinear crystal for optical rectification to generate the THz pulse, PM: gold-coated parabolic mirror, EOS: electro-optic sampling crystal, $\lambda/4$: quarter-wave plate, WP: Wollaston Prism, PD: balanced photo-detector.

found to contribute to THz shape change: (i) the frequency and bandwidth of the gating pulse, (ii) the frequency-dependence of the non-linear susceptibility of the detection crystal, and (iii) the thickness of the detection crystal.

Addressing (i), it was found that in the usual detection scenario, the bandwidth of the gating pulse is much smaller than its central frequency. In this case, the gating pulse does not affect the THz measurement. The frequency-dependent nonlinear susceptibility of the detection crystal (*i.e.* point (ii)) is a property of the crystalline material. The second order susceptibility in $ZnTe$ has a sharp peak at 5.3 THz; below 4 THz, the susceptibility, however, is nearly frequency-independent, as it is above 8 THz, so this spectral filter is not a concern for systems with a bandwidth less than 4 THz. The path length over which the

THz signal and the gating signal are phase-matched is an important factor in the measurement of the true THz pulse shape and spectrum (*i.e.* point (iii)). Thus a thinner crystal is better. (Figure 2 of Ref. [64] shows a gradual decline in the THz transmission from ~0.3–3 THz in a 2 mm *ZnTe* crystal, nearly constant transmission followed by a sharp drop-off in trasmission near 3 THz in a 0.5 mm *ZnTe* crystal, while the transmission bandwidth of a 0.1 mm *ZnTe* crystal extended to 4.4 THz.) On the other hand, the thicker the crystal, the longer the interaction length between the THz and the gating pulses, and thus the stronger the signal. Therefore, a compromise between the two competing processes is necessary.

In addition to *ZnTe*, various other materials have been used for the OR and EOS elements. Semiconductors such as ⟨111⟩ *GaAs*, *GaP* and *GaSb* have been shown to generate THz radiation [61]. However, no THz emission was observed for cubic crystals when the femtosecond beam was incident on the ⟨100⟩ face of the crystal. Quartz and *LiTaO₃* have also been used as the OR element. Nahata et. al. [65] demonstrated optical rectification in a poled polymer with greater efficiency than in a *LiNbO₃* crystal, and a photo-stability after 10 hours of continuous illumination. (*Poling* refers to the process of curing a crystal using an external electric field at elevated temperatures [66].) Extreme bandwidth tunability was demonstrated by Huber *et. al.* [67] using a 90 μm *GaSe* emitter; spectral peaks up to 41 THz were demonstrated with this system. Most important to the increase in bandwidth capability was the thinness of the emitter, which allowed for the phase coherence of the nonlinear polarizability and the THz electric field for the entire interaction length.

THz detection has been proven viable with poled polymers [68], *GaP* [69] and *GaSe* [67]. Wu and Zhang [70] demonstrated a superior signal-to-noise ratio when using *ZnTe* as the electo-optic sampling element, rather than radiation-

damaged silicon-on-sapphire. The organic crystal DAST (dimethyl amino 4-N-methylstilbazolium tosylate) has been used as both an emitter and a detector [71]. As an emitter, Han *et. al.* [71] showed DAST was capable of generating pulses with a bandwidth up to 20 THz.

A more complete list of THz generation and detection materials can be found in Ref. [61].

2.3 Auston Switches vs. Optical Rectification

There are advantages and disadvantages to each of the two main THz methods described in Sections 2.1 and 2.2. Since the current surge method can produce THz peak amplitudes which increase with increasing bias voltage, very high peak amplitudes can be achieved. However, the bandwidth is limited and peak frequencies above 1 THz are rare. This method is useful in applications where high THz amplitudes are more important than a short THz pulse width or wide THz bandwidth. Furthermore, in microscopic transmission line systems, semiconductor lenses are necessary to collimate the THz beam. These are not transparent in the visible wavelength range, making alignment more challenging.

With large aperture Auston switches, where the femtosecond generation beam is not focussed onto the transmission line substrate, the generated THz pulse has a low divergence and is collinear with the incoming femtosecond beam. This makes optical alignment with a diode laser feasible with the temporary removal of the transmission line element. However, large bias voltages are needed to give large enough THz signals for experimental purposes.

The waveforms generated by photoconductive switches are dependent on the frequency-response of the switch generator, its carrier lifetime, and momentum

relaxation time. This is contrasted with the THz waveform acquired from optical rectification, where the signal is dependent only on the frequency-response of the electro-optic crystal. Detection in both cases is dependent also on the THz electric field.

In addition, the optical rectification method for THz generation gives a fairly uniform frequency spectrum over a broad range, often up to several THz before beginning to taper off. This makes it a great system for spectroscopic applications. The bandwidth is found to be limited mostly by the absorption spectrum of the nonlinear crystals used for THz generation and detection.

There has been debate over the source of differences in the waveform shape between these two THz methods. Namely, many photoconductive switches show half-cycle waveforms, while optical rectification emits single-cycle traces. Park *et. al.* deduced that the frequency and lifetime response of photoconductive switches are responsible for the apparent half-cycle nature of these THz pulses [72].

2.4 Other THz Methods

Various other techniques for THz generation and detection have been proposed and are briefly described here. Photoionization in a variety of gases, including He and Ar [73], air [74], and N_2O [51], have been shown to emit radiation in the THz regime. These systems rely on up- or down-conversion within the gases for the far-infrared emission.

Quantum well structures can be used as THz emitters, where emission is thought to result from polarised excitons in the quantum well [75]. This is actually another manifestation of OR. The existence of excitons was used to show the presence of charge oscillations in quantum wells: the beating of light and heavy hole excitons results in optical rectification upon excitation from a pulsed laser source, and emits radiation in the THz regime [76]. The peak of the

THz was shown to be slightly tunable (1.4 to 2.6 THz) with the applied electric field [76].

Magnetic fields of several Tesla applied to *InAs* crystals have been shown to be viable THz sources [77, 78]. THz emission was studied with applied fields up to 5.5 T in *GaAs* and *InAs* [78]. Coupled cyclotron-plasma charge oscillations were cited to be the source of far-infrared emission. A photoconducting capacitor array has been demonstrated, and may be useful as a THz imaging source [79].

The following chapter will discuss the THz generation and detection system built for the Ultrafast Spectroscopy Laboratory in the University of Alberta's Physics Department.

Chapter 3

THz System in the USL

A permanent THz-probe setup was required in the Ultrafast Spectroscopy Laboratory (USL). Several preliminary versions were constructed to investigate ways by which to optimise the setup. The final setup includes possible future modification options, and was built for use both as a linear spectroscopy source and as a probe beam in pump-probe experiments. This section will describe the USL THz system and diagnostics which were undertaken to characterise the setup. First, however, a brief description of the laser system used for the THz generation and detection will be outlined.

3.1 The Laser System

Femtosecond laser pulses are needed to generate and detect THz pulses. In the USL, femtosecond pulses are first generated in a Kapteyn-Murnane (KM Labs) modelocked laser (also referred to as the *oscillator* or the *seed laser*). The lasing medium is a Ti-doped sapphire crystal which is pumped by a Millennia laser whose output wavelength is 532 nm. The modelocked laser outputs 30 fs pulses (FWHM) with a centre wavelength of 800 nm and a repetition rate of

90 MHz. These pulses are then fed into a multi-pass amplifier (the Odin system, from Quantronix), where they are first stretched both spectrally and temporally using a pair of gratings. A Pockels cell in the amplifier picks one pulse every millisecond. This pulse passes through the Ti:sapphire crystal eight (8) times, and then is compressed by a pair of gratings. The average laser output power is nominally 700 mW, 20% of which is used in the THz system. Of this 20%, 80% is used for THz generation, while the remaining power is used for THz detection. These femtosecond pulses arrive at the THz setup with a repetition rate of 1 kHz, a pulse duration of approximately 100 fs (FWHM) and a centre wavelength of 800 nm. A schematic of the laser system is shown in Figure 3.1(a).

3.2   Description of the THz Setup

The USL THz layout is shown in Figure 3.1(b). Emission is achieved through OR in a 0.5 mm-thick $ZnTe$ crystal. The THz is collected by a 1"-focal length gold parabolic mirror, and collimated with a 4"-focal length parabolic mirror. (All parabolic mirrors in the THz setup are gold-coated and have 2"-diameter apertures.) This beam-expansion system allows for a wider collimated THz beam (approximately 1" in diameter) and a tighter focus. Residual THz-generation beam is blocked by a thin piece of black polyethylene. The THz beam then passes through a focus and is recollimated with a pair of 3"-focal length gold parabolic mirrors; the THz focal spot (approximately 2 mm in diameter) allows for future modifications to the system. The THz beam then is focussed onto the sample with another 3"-focal length gold parabolic mirror, brought through a collimator, and is finally focussed onto the detection crystal. The THz beam is electro-optically detected in a 2 mm-thick $ZnTe$ crystal. The sampling beam (used for THz detection) passes through a small hole drilled through the final
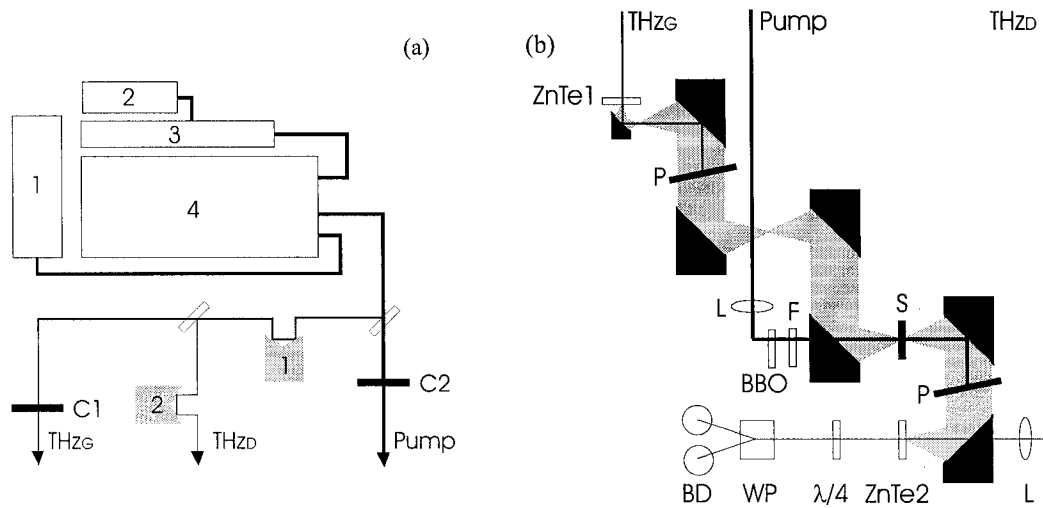
Figure 3.1:   (a) Schematic of the laser system in the Ultrafast Spectroscopy Lab. 1: Pump laser for the multipass amplifier, 2: Pump laser for the seed laser, 3: Kapteyn-Murnane Ti:Sapphire seed laser, 4: Odin multipass amplifier. Stage 1 is moved to delay the THz beam with respect to the pump beam in pump-probe exeriments, while stage 2 delays the THz-detection beam with respect to the THz-generation beam. The chopper (which has a beam chopping frequency of 270 Hz) is placed in position C1 for the experiments described in much of this document; in Chapter 6 the chopper is moved to position C2. The beam paths THz$_G$, THz$_D$ and Pump refer respectively to the THz generation beam, the THz detection beam, and the sample pump beam. (b) Schematic of the THz apparatus. The THz beam is generated at ZnTe1, while the THz beam is detected at ZnTe2. L: lens, P: polyethylene visible beam block, F: blue filter, BBO: β-barium borate crystal for second harmonic generation, $\lambda/4$: quarter-wave plate compensator, WP: Wollaston prism, and BD: balanced detector. The signals from the balanced detector are routed to an analog-to-digital conversion board, and measured via a LabVIEW program.

parabolic mirror, and is focused onto the $ZnTe$ detection crystal. The sampling and THz beams must overlap on the detection crystal for proper signal detection.

Ellipsometric THz detection is used in this setup (see Section 2.2.2). Under an external bias provided by the THz field, the detection beam polarisation is altered by the induced birefringence within the ZnTe crystal. A quarter-wave delay is imposed, and a Wollaston prism converts the phase modulation to an intensity modulation. The two components of polarization, A and B, are then detected in a pair of balanced photodiode-detectors, and the signals $(A - B)$ and $(A + B)$ are sent to lock-in amplifiers.

The detection beam is delayed with respect to the generation beam via the computer-controlled delay stage 2 (Melles Griot) in Figure 3.1(b). Because the THz pulse is much longer in duration than the detection pulse, the detection beam measures essentially a direct current electric field (due to the presence of the THz pulse) applied to the detection $ZnTe$ crystal. Varying the time delay between the THz and the detection beams allows for the mapping out of the entire THz electric field.

3.3   Data Acquisition: A LabVIEW Program

Time-domain data is acquired through a LabVIEW program written specifically for the experiments discussed in this document. The program acquires voltage inputs at user-specified time intervals for a certain duration. These are then written to a text file, with a filename of the form: $MMDDHHmm.dyy$, where MM is a two-letter month abbreviation, DD is the two-digit day of the month, $HHmm$ is the time of the write-out on a 24-hour clock, d is a spacer, and yy the two-digit year. For example, a data file acquired on April 20th, 2001 at 1:35pm would have the filename $Ap201335.d01$. The Labview control panel is shown in Figure 3.2. Fields in white can be altered by the user before each scan. Fields in

grey are parameters presented to the user by the program. With this program, one may obtain a single scan of a length in picoseconds, with a data point taken at time intervals specified by the user. Data is read from the data acquisition (analog-to-digital) (DAQ) board channel $A0$, while the reference input is through channel $A2$. (Channel $A1$ can is also recorded, but is not used in the experiments described in this document.) Each data point is divided by the reference point $(A0/A2)$ in order to remove large laser fluctuations from the data. Multiple scans can also be obtained and averaged; the output text file for the average and referenced data have filename extensions of $.avg$. A fast Fourier transform (FFT) may be performed on the data by toggling the appropriate button; this filename extension is $.fft$.

An example of THz time domain and frequency domain data, taken in a dry nitrogen atmosphere is given in Figure 3.3.

A large aperture photoconductive switch THz emitter was studied as an undergraduate project by Jeffrey Stollery. For information on this setup, see Ref. [80].

3.4   Absorption Spectra in Water and Silicon

Linear spectroscopy in the THz regime have been reported for a variety of materials [18]. Spectroscopic measurements give rise to a range of material properties, including complex conductivity, and refractive indices (see Chapter 1).

In the USL, standard THz spectroscopy was performed on water and silicon to show this capability with the experimental set-up. The absorption spectrum for water vapour was taken by transmitting the THz pulse through a humid enclosure, and referencing this trace with one taken in a dry gaseous nitrogen-flow environment. The time domain THz traces can be seen in Figure 3.4(a), and the corresponding spectra in Figure 3.4(b). Many water absorption lines could
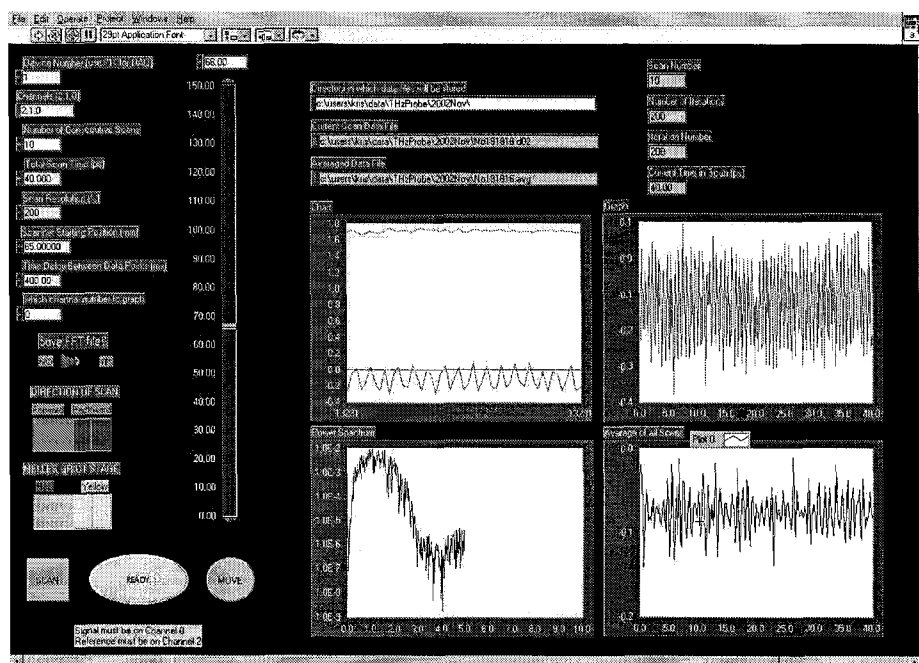
Figure 3.2:   The control panel for the LabVIEW program entitled "Pump Probe.VI". This program is used to acquire both THz scans and the pump-probe data described in Chapter 4.

be readily identified, as can be seen in Figure 3.4(c). Our data corroborate other published THz spectroscopy information for water absorption. (See for example Ref. [51].) Detailed THz spectroscopic studies on liquid water can be found in Ref. [81].

The absorption spectrum for a silicon wafer was taken. As can be seen in Fig. 3.5, Si has a frequency-independent low absorption for the 0.5-2.5 THz range. This agrees with Ref. [13], where THz spectroscopy showed a flat index of refraction in silicon from 0.2-2.0 THz of $n = 3.418$.
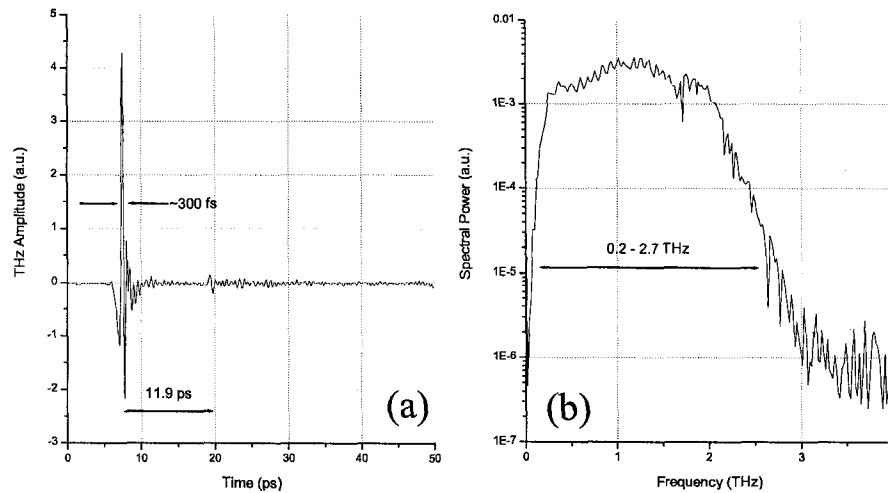
Figure 3.3: (a) THz signal in a nitrogen-rich environment and (b) its corresponding spectrum generated by the THz layout setup described in this section. The FWHM of the main pulse is less than 0.5 ps. Note the reflection of the THz pulse in (a) at ∼19 ps due to the detector crystal (thickness 1 mm in this figure). (b) The bandwidth is fairly uniform between 0.3 and 2.5 THz. This gives an indication of the usable bandwidth in this THz setup.

3.5 Calibration of the THz Electric Field

The THz electric field is rarely reported in descriptions of THz systems, possibly due to difficulties in this measurement. When reported, no description of procedure is given. The USL has calibrated the peak of the THz electric field of the experimental setup in the laboratory. An oscilloscope was used by F. Hegmann to measure the signals arriving at the two photodiodes in the balanced detector; these measurements were shown to be related to the THz electric field, E_{THz}.
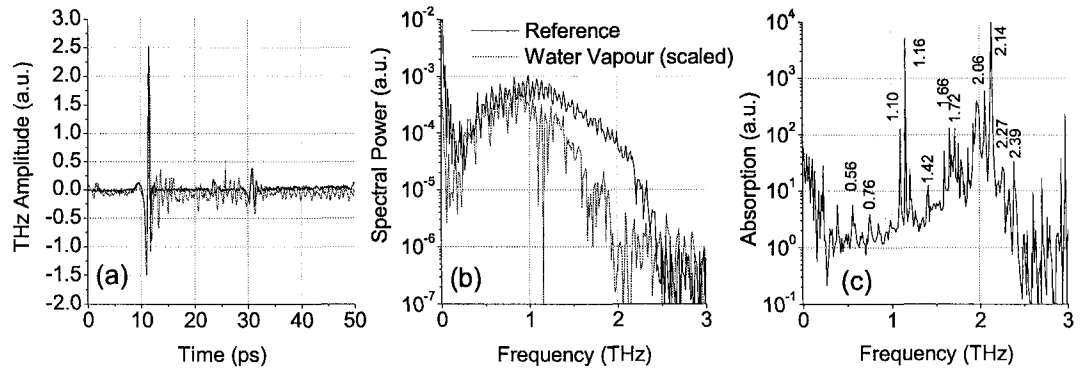
Figure 3.4: (a) THz time domain and (b) spectral data taken of water vapour and referenced to a dry nitrogen gas atmosphere. Oscillations in the water vapour data in (a) are a result of water vibrational energy absorption in the THz regime. (c) Water absorption lines are positively identified, where the labels are in THz. (Note: 1 THz $\sim$ 33.3 cm^{-1}.)

Using the index ellipsoid, E_{THz} was calculated from this oscilloscope measurement.

Voltages from the two photodiodes in the balanced detector (A and B) were read on an oscilloscope. (Recall from Section 2.2.2 that the two photodiodes are balanced (*i.e.* $A - B = 0$) in the absence of an external electric field.) The ratio of the THz peak amplitude ($A - B$) to the total output of the two photodiodes ($A + B$) was measured to be $(A - B)/(A + B) = 0.061 \pm 0.002$.

Planken *et.al.* calculated the orientation dependence of the THz pulse detection in $ZnTe$ [82]. Using their results to calculate the USL E_{THz} given the normalised phase shift, $(A - B)/(A + B)$, I find
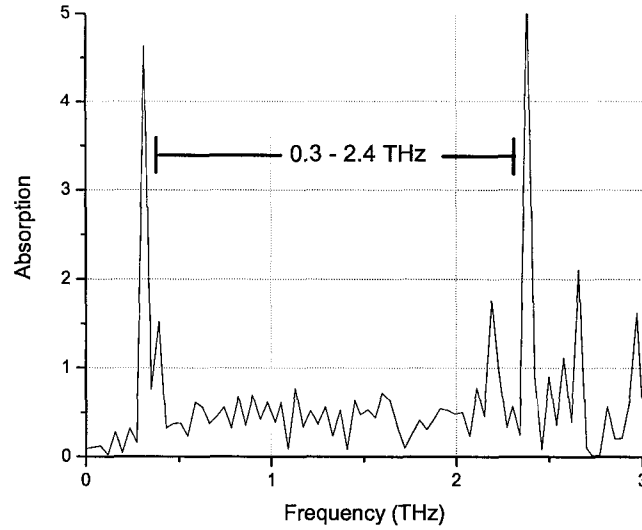
Figure 3.5:   A high-resistivity silicon wafer has essentially no THz absorption in the 0.3–2.4 THz range, as identified with linear THz spectroscopy. The spikes in the absorption graph near 0.3 and 2.4 THz are due to noise; the THz system in the Ultrafast Spectroscopy Laboratory has a useful frequency range between 0.3–2.4 THz.

$$E_{THz} = \frac{\lambda}{\pi n^3 r_{41} d (cos\alpha \ sin2\theta + 2sin\alpha \ cos2\theta)} \left(\frac{A - B}{A + B}\right), \qquad (3.1)$$

where r_{41} is the electro-optic coefficient of $ZnTe$ at the detection wavelength λ, d is the crystal thickness, α and θ are the angles of the detection and THz polarisations with respect to the $ZnTe$ $\langle 001 \rangle$ axis as seen in Figure 3.6. Eq. 3.1 assumes the use of $\langle 110 \rangle ZnTe$, and that the detection beam, E_p, and THz beam, E_{THz}, both propagate along the crystal's $\langle 110 \rangle$ axis.
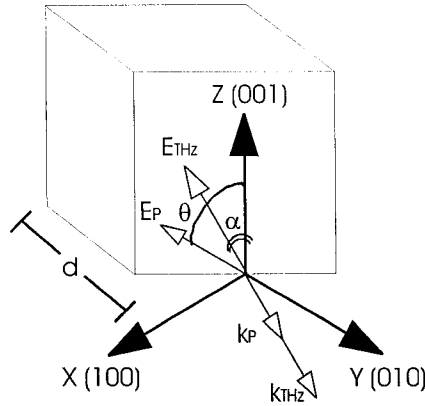
Figure 3.6:   Axes and angles definitions for Eq. 3.1 to calculate the THz electric field as detected via electro-optic sampling in a $ZnTe$ crystal of thickness d. Propagation of both the detection $\vec{k}_p$ and THz $\vec{k}_{THz}$ beams is along the $\langle 110 \rangle$ direction, while their polarisations, E_p and E_{THz}, relative to the crystal's $\langle 001 \rangle$ axis are θ and α, respectively.

In the USL, the $ZnTe$ crystal used for THz detection is $d = 2\ mm$ thick and its index of refraction at the detection wavelength of $\lambda = 800\ nm$ is $n = 2.85$. For r_{41} at 800 nm, a linear interpolation between known values was made. At 1090 nm $r_{41} = 3.9 \times 10^{-12}\ m/V$ and at 589 nm $r_{41} = 4.51 \times 10^{-12}\ m/V$; thus, $r_{41} = 4.25 \times 10^{-12}\ m/V$ was used for a wavelength of 800 nm. Using $(A-B)/(A+B) = 0.061\pm0.002$ from the oscilloscope measurement, and knowing that the detection and THz beams are parallel to each other and are 35° from the $\langle 001 \rangle$ crystal axis (Figure 3.7, the THz peak amplitude is calculated to be 680 ± 30 V/cm.

For completeness, Figure 3.8 displays the THz peak electric field as a function of $(A - B)/(A + B)$ and the angle between the THz field and the $ZnTe$ $\langle 001 \rangle$ axis. This graph is based on Eq. 3.1, and assumes the THz and detection beam
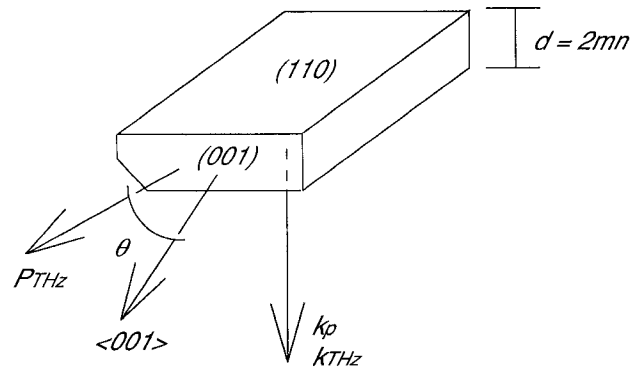
Figure 3.7: The *ZnTe* detection crystal orientation in the Ultrafast Spectroscopy Laboratory's THz setup. Both the THz beam and the gating beam travel along the crystal's ⟨110⟩ direction, while the THz beam polarisation is $\theta=35°$ from the crystal's ⟨001⟩ axis.

polarisations are parallel.

In-Situ Method

While the oscilloscope measurement was used to calibrate the THz electric field, it is not viable in day-to-day operation since the photodiodes need to be disconnected from the lock-in amplifier to make the oscilloscope measurement; an in-situ method of measuring the THz electric field was wanting. Fortuitously, the difference and sum of the two photodiodes are measured by the lock-in amplifiers as well. Note that the sum of the intensities observed by the two photodiodes, $(A+B)$, is electronically summed. Because of the electronics involved, this is less than the value obtained if each photodiode output were measured and manually added. However, based on lock-in amplifier readings, the electronically summed value is approximately 5-10% less than the actual sum of the two photodiode

outputs.

Typically, $A - B = 5.6$ mV, while $A + B = 10.8$ mV; hence $(A-B)/(A+B) = 0.5185$. From Eq. 3.1, this translates to a THz peak amplitude of 5774 V/cm.

The discrepancy between the oscilloscope measurement and that of the lock-in amplifier is not fully understood. Possibly it is an artifact resulting from the difference in reference frequencies in the two lock-in amplifiers: one for the A and B signals, which are then electronically subtracted in the amplifier, and the second for the $(A + B)$ signal. The first amplifier is referenced to 270 Hz while second amplifier for the $(A + B)$ signal is referenced to 1080 Hz. This may affect the lock-in averaging of signals, leading to the described discrepancy.

From the measurements of the THz peak electric field described in this section, a calibration factor of 8.49 is calculated. That is, the lock-in amplfier measurement of the THz electric field is expected to be a factor of 8.49 larger than the actual value.

A separate set of photodiodes used in a balanced detection system is used in the same laboratory for Kerr signal experiments [83]. A similar method to that described in this section was used to measure the signals received. A factor of 8.3 between the lock-in amplifier calculation method and the oscilloscope method was found.

In this chapter, a THz generation and detection system designed, built, calibrated, and tested for the Ultrafast Spectroscopy Lab as described. THz radiation is generated via optical rectification and detected electro-optically in $ZnTe$ crystals. Terahertz linear spectroscopy was shown to be viable with the examples of water and silicon absorption. In addition, the THz peak amplitude was calibrated to be 680 $\pm$ 30 V/cm with a lock-in amplifier calibration factor of 8.49.

In addition to linear far-infrared spectroscopy, THz pulses have also been used to study dynamics in various materials. The rest of this document will describe experiments which use THz pulses as a probe of carrier relaxation mechanisms in silicon-on-sapphire systems.
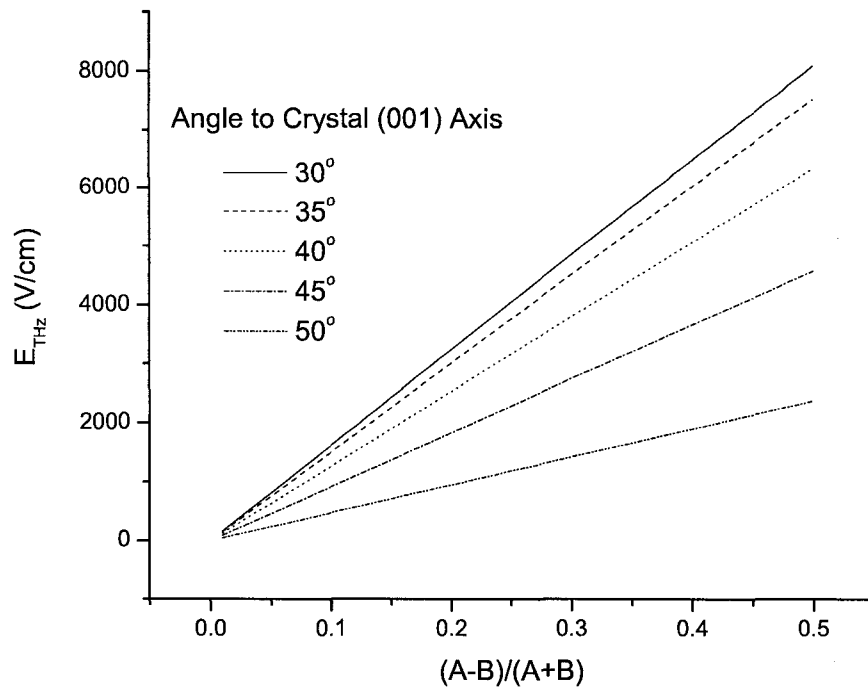
Figure 3.8: This graph displays the THz electric field as a function of induced birefringence as measured by balanced photodiodes, $(A - B)/(A + B)$, based on Eq. 3.1. Various THz beam polarisation angles (equal to the detection beam polarisation angles) with respect to the $ZnTe$ $\langle 001 \rangle$ axis are represented.

Chapter 4

Experimental Procedure

In this chapter, I will outline the apparatus and materials used specifically in the 400 nm pump – THz probe experiments, and describe data acquisition and analysis routines.

4.1   400 nm Pump – THz Probe Apparatus

The second harmonic (400 nm wavelength) of the amplified Ti:sapphire laser was generated through a type-I β-barium borate (BBO) crystal and used as the pump beam (see Figure 3.1). The THz generation beam was chopped at 270 Hz to allow for lock-in detection. The pump and the THz probe beams pass through a 1 mm-diameter aperture, on which the sample is mounted. The 400 nm pump beam has a focus of $\sim$2 mm, hence the 1 mm aperture ensures uniform illumination of the sample. Since the THz focal width is just wider than 1 mm, the lowest frequencies are attenuated after the aperture, as seen in Figure 4.1. The pump fluence incident on the sample was varied using neutral density filters. Residual 400 nm pump beam after the sample is blocked with a thin black polyethylene sheet, while the THz beam is transmitted through the sample and focussed onto

the *ZnTe* detection crystal.
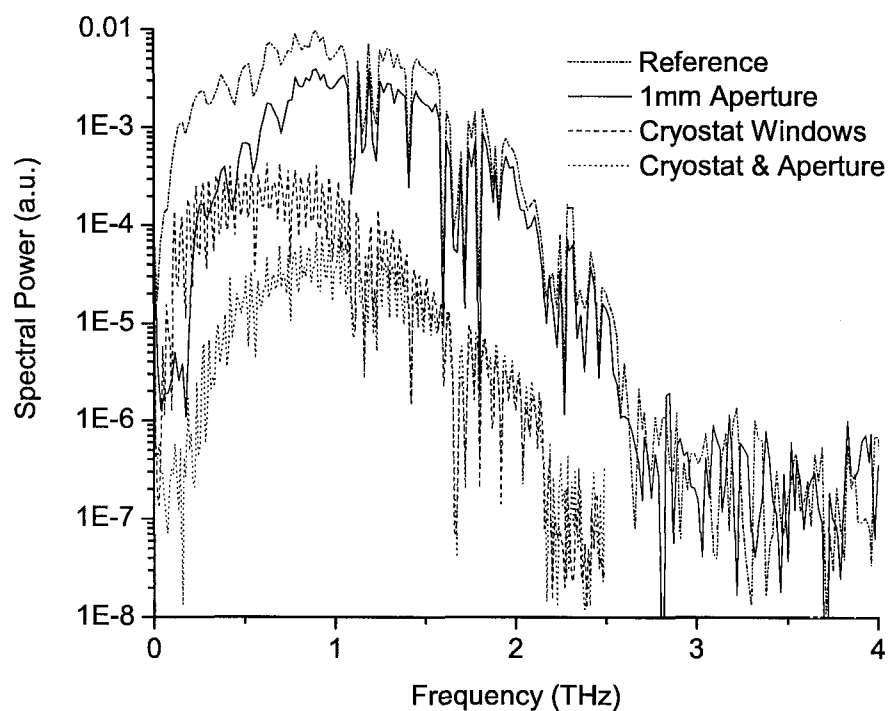
Figure 4.1: THz spectra showing losses due to the 1 mm aperture through which both the pump and THz beams pass, as well as losses due to the cryostat windows (where three are glass and one polypropylene). Note the low-frequency attenuation due to the aperture, while higher frequencies are diminished due to absorption in the cryostat windows.

4.2 Silicon-on-Sapphire

The original sample [1] was a moderately-damaged silicon-on-sapphire (SOS) sample (S1), and was O^+ implanted twice, each with a 1×10^{13} cm^{-2} dose, at ion energies of 100 keV and 200 keV. A heavily-damaged SOS sample (S2) underwent O^+ implantation with doses of 1×10^{15} cm^{-2} at 100 keV and of 2×10^{15} cm^{-2} at 200 keV. The amorphous silicon sample (S3) was deposited by electron-beam evaporation onto a piece of the same sapphire substrate as sample S1. (The substrate was etched with KOH prior to evaporation to remove the lattice-damaged Si film.) The silicon source was evaporated at a rate of 3 Å/s under an initial pressure of 10^{-6} torr. The evaporation pressure was low enough to avoid oxygen contamination (oxygen ions would passivate dangling bonds in a manner similar to the presence of hydrogen in a silicon thin film [27]. The silicon film was 0.4 μm thick for both S1 and S3, while S2 was 0.5 μm thick. All samples were on 0.5 mm thick [1$\bar{1}$02]-oriented sapphire (Al_2O_3) substrates. The small difference in Si film thickness did not affect our measurements since the optical penetration depth of the 400 nm pump beam (0.082 μm in c-Si and 0.0145 μm in a-Si [1, 84]) is much smaller than the thickness of the silicon films. Thus the pump beam was completely absorbed in the samples.

No phase shift was apparent in the THz waveform when transmitted through the excited sample, as is shown in Figure 4.2, implying $\omega\tau_d < 1$. (Recall that τ_d is the scattering time constant, as was described in Section 1.2.) This allowed the monitoring of the THz peak amplitude without scanning the entire THz pulse for each pump-probe time delay increment.
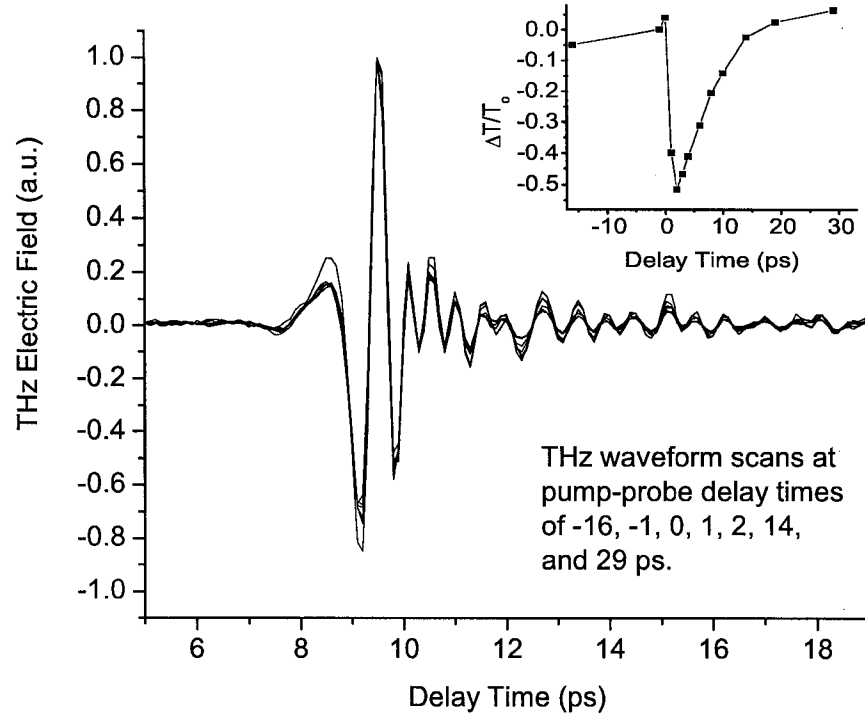
Figure 4.2: THz wave forms transmitted through the RD-SOS sample for delay times of the peak of the THz-probe pulse with respect to the pump pulse of -16, -1, 1, 2, 14, and 29 ps. The wave forms are normalised to unity. No phase shift is apparent in the THz wave form transmitted through the excited sample at positive probe time delays. The pump fluence was approximately 800 μJ/cm^2. The inset displays the differential transmission of the positive peak of the THz pulses (points) from the main figure, giving a visual representation of $\Delta T/T_o$ data. The solid line in the inset is simply a guide for the eye.

4.3 Cryostat

An optical cryostat (Oxford Instruments Optistat Bath) was used to vary the temperature of the sample from 5 K to 300 K. This is a continuous-flow cryostat,

where the sample chamber contains helium vapour. The pump and probe beams pass through two glass windows prior to arrival at the sample. The pump beam is absorbed in the sample, while the THz beam continues past the sample and travels through a glass window and a polypropylene window. The sample is mounted onto a 1 mm aperture, which is then clamped into the cryostat sample stick; both the pump and THz beams arrive at normal incidence on the sample.

The cryostat glass windows prevent the higher frequencies from reaching the sample, as seen in Figure 4.1. Careful attention was made towards calibrating pump intensity losses due to the cryostat windows and reflection off the front face of the sample. For reference, the 400 nm and THz transmission coefficients were measured for a variety of possible cryostat window materials. These are presented in Table 4.1.

Table 4.1:   Transmission coefficients for the passage of 400 nm and THz beams through various possible cryostat window materials. RMPP: Polypropylene from a Rubber Maid container; TRANS: overhead transparency; CPP: polypropylene windows provided by Oxford Instruments; GLASS: glass windows provided by Oxford Instruments.

	RMPP	TRANS	CPP	GLASS
400 nm	0.515 ± 0.011	0.784 ± 0.020	0.504 ± 0.012	0.912 ± 0.022
THz	0.991 ± 0.107	0.845 ± 0.091	0.792 ± 0.085	0.763 ± 0.082

4.4 Data Acquisition with LabVIEW

The differential transmissivity, $\Delta T = T - T_o$, as a function of pump-THz time delay, t, where T_o is the transmissivity of the positive peak of the THz pulse during negative times (when the THz pulse arrives at the sample before the pump pulse), is acquired by the LabVIEW program mentioned in Section 3.2. These data are normalised to T_o and is plotted as a function of the delay time t. Figure 4.3 shows an example of a $\Delta T/T_o$ plot for sample S1 pumped at 344 μJ/cm^2 in an ambient environment.
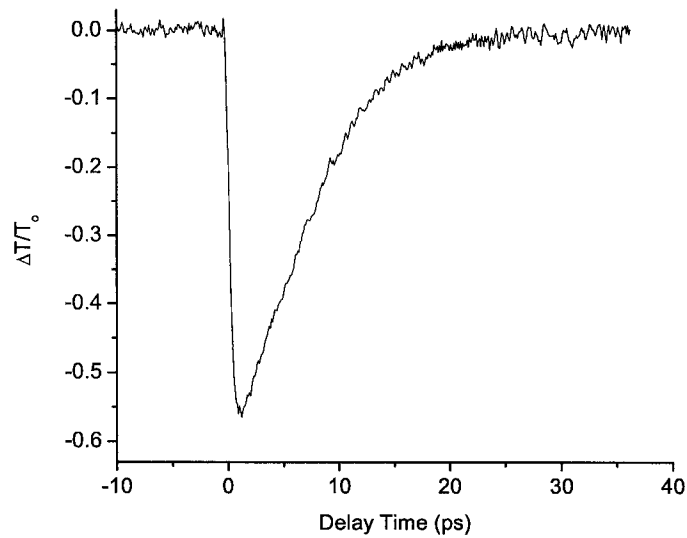
Figure 4.3: THz peak transmissivity as a function of delay time between pump and THz pulses for sample S1, which was pumped at a wavelength of 400 nm with a fluence of 344 μJ/cm^2 at room temperature.

To reduce baseline noise, five consecutive scans were taken and averaged point-by-point. Figure 4.4 illustrates the improvement to the signal-to-noise

ratio for an example.
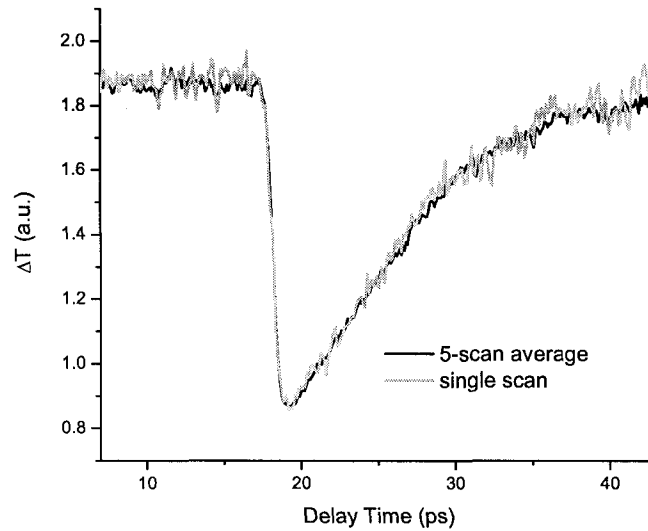
Figure 4.4: Normalised differential transmission curves for a single scan (grey line) and for a five-scan average (black line). Data mentioned in this document are averages of five scans to reduce baseline noise.

To further test the system, normalised differential transmission traces were obtained for various pump fluences on polycrystalline *CdTe* (Figure 4.5). Note the rapid decrease in THz transmission, followed by a slower rise time constant. Similar transients have been observed in other bulk semiconductors, including *GaAs* and *InP* [39], and *ZnTe* and *CdTe* [41]. The initial fast response is due to photogeneration of free carriers; these relax from the low mobility L-valley to the higher mobility Γ-valley, resulting in the slower THz transmission drop [39].
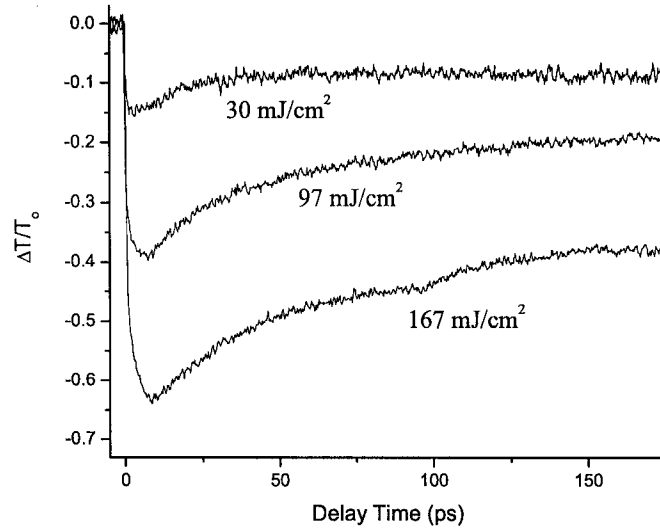
Figure 4.5: 400 nm pump – THz probe data on polycrystalline $CdTe$. The roundedness of the initial drop in the $\Delta T/T_o$ traces is a result of the charge carriers relaxing from the low mobility L-valley to the higher mobility Γ-valley.

4.5 Transmission through Thin Films

The transmission of a far-infrared wavelength λ through a thin film of thickness $d \ll \lambda$ situated on a thick substrate such that the optical penetration depth δ is $d \ll \delta < \lambda$ can be considered by a boundary value problem [85]. The thin film is idealised as a surface current where the current density is constant throughout the thickness of the sheet. With normal incidence, the amplitude coefficient of transmittance, T, and reflectance, R, are related through the following equations:

$$1 + R - T = 0,$$

$$1 - R - NT = \frac{4\pi}{c}\sigma_s dT, \tag{4.1}$$

where σ_s is the sheet current density, and the non-absorbing substrate index of refraction is N. Solving Eqs. 4.1 gives

$$T = \frac{2}{1+y+N}$$
$$R = \frac{1-(y+N)}{1+y+N}, \tag{4.2}$$

where $y = Z_o \sigma d$ is the dimensionles complex admittance for the thin film, and $Z_o = 377\Omega = 4\pi/c \ (c.g.s.) = \sqrt{\mu_o/\epsilon_o} \ (SI)$ is the impedance of free space.

Although the conductivity, σ is a complex quantity, it can be simplified to the low-frequency value, $\sigma_o = n_c e\mu$, in these experiments since $\omega\tau_d < 1$. In this case, n_c is the carrier density, and the effective carrier mobility is given by $\mu = e\tau_d/m^*$, where m^* is the carrier effective mass. At negative times, no conductivity is present (since the sample returns to equilibrium between pump pulses), and the transmissivity is simply $T = 2/(1+N)$. The normalised transmissivity as a function of positive time delay $t > 0$ is thus [1, 48, 49]

$$\frac{T(t) - T_o}{T_o} = \frac{\Delta T(t)}{T_o} = \frac{1+N}{1+N+Z_o n_c(t)e\mu(t)\delta} - 1. \tag{4.3}$$

In Eq. 4.3, the thickness of the thin film is replaced with the optical penetration depth of the pump beam into the film, δ; this simplification assumes a uniform photoexcited carrier density within the optical penetration depth. For RD-SOS, the substrate is Al_2O_3 and has a refractive index of $N = 3.1$ in the THz region.

4.6   Fitting the Drude Model to the Data

The maximum carrier density generated in the Si thin film by the pump pulse is given by:

$$n_{max} = \frac{(1-R)F}{\delta \hbar \omega}, \tag{4.4}$$

where $R = 0.48$ is the reflectance of the Si thin film, F is the incident pump fluence, and $\hbar \omega = 3.1$ eV is the energy of the pump beam photons [48]. The maximum carrier density is assumed to occur when the entire pump pulse has arrived at the sample. Using the simplest case of a single relaxation process, with time constant τ, the carrier density is modelled by $n_c(t) = n_{max} exp(-t/\tau)$.

Assuming a time-independent carrier mobility, μ, $\Delta T/T_o(t)$ is calculated for $n_c(t)$ using Eq. 4.3. Figure 4.6(a) shows examples of this model with different pump fluences, using a constant carrier mobility of $\mu = 440$ cm^2/Vs and a carrier relaxation time constant of $\tau = 5\,ps$. Although the carrier density decays with a single exponential, it is clear from Figure 4.6(a) that the $\Delta T/T_o$ curves look exponential for only low pump fluences; at moderate pump fluences, the decay appears linear with time, while the highest pump fluences yield a sigmoidal shape. Note that the maximum $\Delta T/T_o$ does not vary linearly with pump fluence. The effect of carrier mobility is shown in Figure 4.6(b) for a pump fluence of 500 $\mu J/cm^2$ and a relaxation time of 5 ps.

The Drude model was fit to the $\Delta T/T_o$ data, with only the effective carrier mobility, μ, and the carrier relaxation time constant, τ, as fitting parameters. Figures 4.7 and 4.8 illustrate the uniqueness of the two parameters and give an indication for uncertainties in the fits.

4.7 Precautions

To be certain that the observed THz transmissivity signals were indeed due to the sample and were not due to spurious effects, a few precautionary steps were taken.
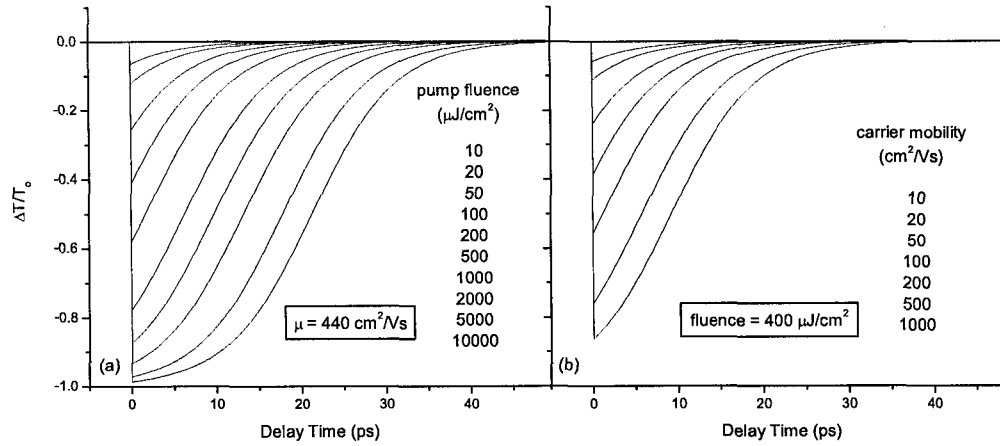
Figure 4.6: Simulation of the normalised differential THz transmission traces as a function of (a) pump fluence and (b) effective carrier mobility. Carrier density is assumed to decay with a single exponential time constant of 5 ps. The effective carrier mobility is 440 cm^2/Vs in (a), while the pump fluence is 400 $\mu J/cm^2$ in (b).

The substrate was considered for possible THz absorption. A piece of sample S1 was etched in KOH to remove the Si layer, leaving the sapphire substrate unaffected. Using THz spectroscopy, it was determined that the substrate did not absorb any THz wavelengths, as shown in Figure 4.9. The sample S1 was also found to have no absorption in the THz regime.

Data for all three SOS samples will be presented and analysed in the next chapter using the ideas presented in this chapter.
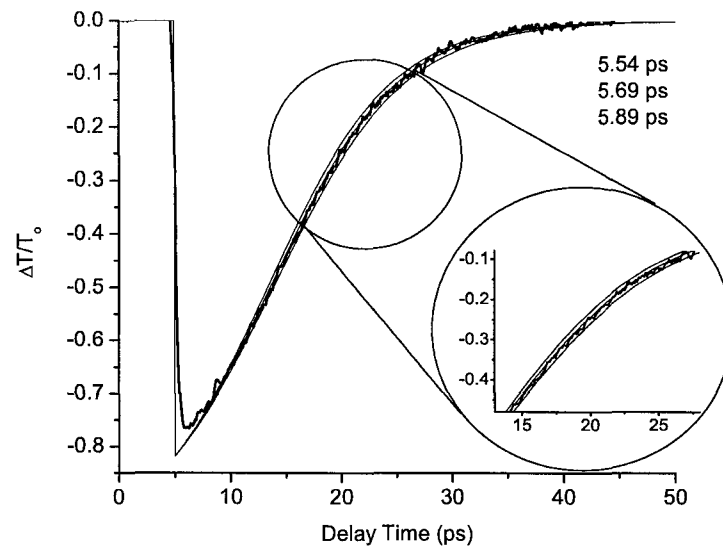
Figure 4.7: Fitting the relaxation time constant τ in the simple Drude model to acquired data for an effective carrier mobility of $\mu = 457\ cm^2/Vs$.
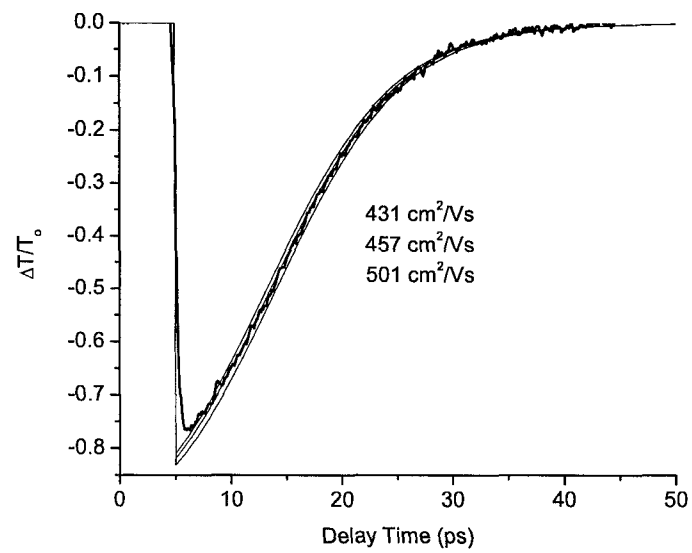
Figure 4.8: Fitting the effective carrier mobility μ in the simple Drude model to acquired data for a carrier relaxation time constant of $\tau = 5.69 \ ps$.
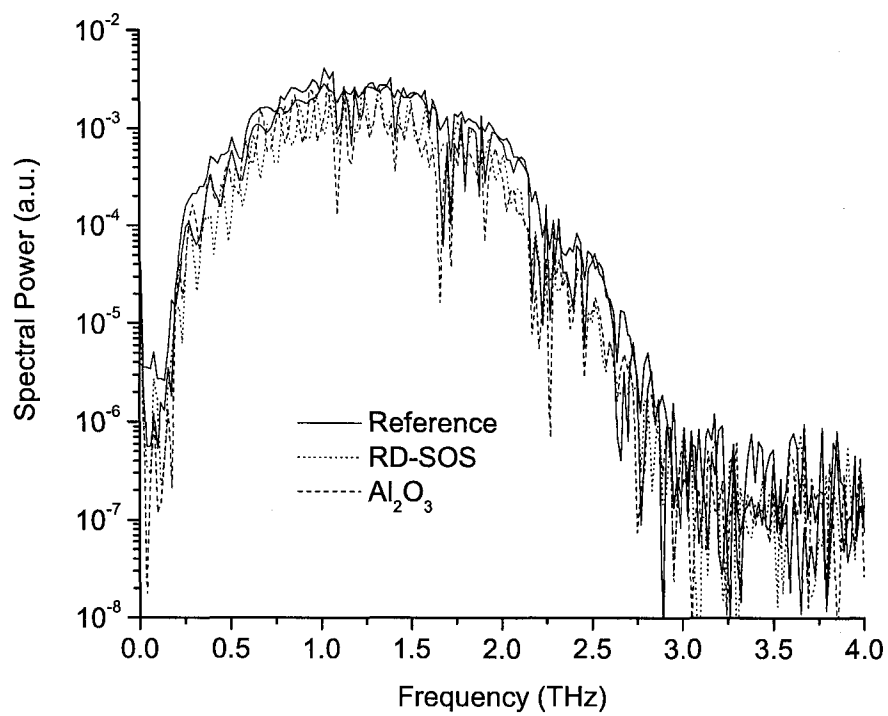
Figure 4.9: THz spectra showing no absorption in the far infrared of the electromagnetic spectrum in either sample S1 or in the sapphire (Al_2O_3) substrate.

Chapter 5

Results and Discussion

The work presented in this chapter has been published in *Applied Physics Letters* [1] and the *Journal of Applied Physics* [49].

5.1 Damage Dependence

Figure 5.1(a) shows the normalised differential transmissivity $(\Delta T/T_o)$ for the three samples described in Section 4.2. These traces were taken at room temperature at a pump fluence of ~ 1000 $\mu J/cm^2$ (corresponding to an injected carrier density of $n_c \sim 7.4 \times 10^{20}$ cm^{-3}). The transients for S2 and S3 are on the order of a picosecond, and are therefore convolved with the THz pulse which has a detection response time of approximately 0.5 ps full-width at half-maximum.

5.2 Relaxation Time Constants

To deconvolve the $\Delta T/T_o$ signals and the THz pulses, the THz detection response was modelled as a low-pass Butterworth filter of order 10, with the cut-off frequency at 2 THz (Figure 5.2). While a larger order in the Butterworth filter would have matched the THz spectrum better, only the order 10 filter was able
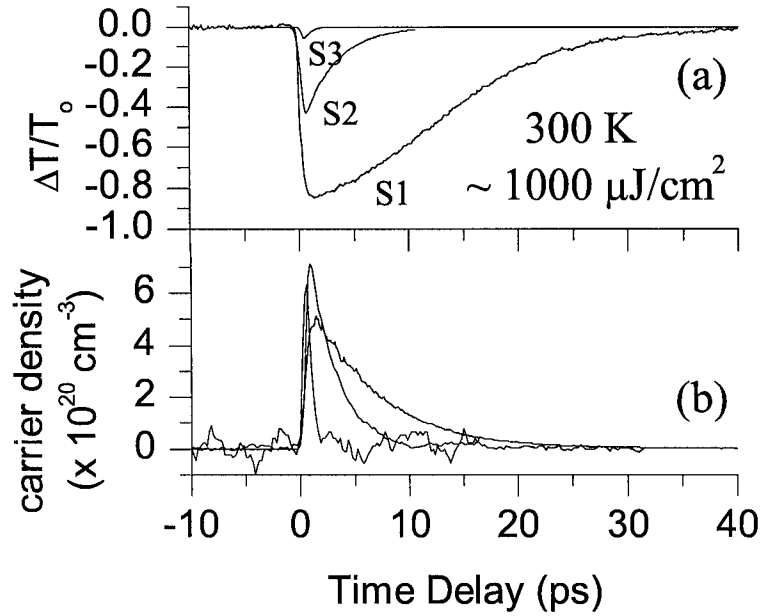
Figure 5.1: Comparison of S1 (moderately-damaged silicon-on-sapphire), S2 (heavily-damaged silicon-on-sapphire), and S3 (amorphous silicon thin film on saphire) at room temperature with a pump fluence of 1000 μJ/cm^2 (carrier density $\sim 7.4 \times 10^{20}$ cm^{-3}). (a) The normalised amplitude transmission of the THz peak as a function of time relative to the arrival of the pump beam is used in a Drude model to extract (b) the transient photogenerated carrier density, as discussed in Section 5.4.

to reproduce the rise and fall times in the data consistently (Figure 5.3). Ideal $\Delta T/T_o$ traces were generated with a Gaussian shape for the rise of the signal, exp($-t^2/\tau_R^2$), mimicking the pump pulse shape, and a single exponential fall time constant, exp($-t/\tau$), where τ_R is the risetime constant, and τ the fall time constant. These ideal traces were filtered with the Butterworth filter, and the

characteristic rise and fall times for the Gaussian and exponential fits, respectively, were adjusted so as to match the filtered $\Delta T/T_o$ traces with the raw data. The data for S1 were also filtered and compared to the original data to verify that these $\Delta T/T_o$ traces were not affected by the short THz detection response time (Figure 5.5(f)). An example of the raw data, the generated ideal trace, and the filtered trace for S3 is shown in Figure 5.4. Note that only one exponential fall time constant was necessary to match the filtered traces to the data. The ideal $\Delta T/T_o$ traces were used in the subsequent analysis. The single-exponential time constants for the relaxation of the signals in Figure 5.1(a) are 6.0 $\pm$ 0.6 ps, 2.2 $\pm$ 0.1 ps, and 0.59 $\pm$ 0.05 ps for S1, S2 and S3, respectively. The uncertainty values are representative of the uniqueness of the fit between the filtered traces and the data.

These results agree with other experiments. For example, a 625 nm pump-probe experiment demonstrated decreasing carrier relaxation time constant with increasing damage [24]. This all-optical pump-probe setup showed a saturation of the carrier relaxation time constant of approximately 0.6 ps with O^+ implantation doses $\geq 10^{15}$ cm^{-2}, consistent with amorphization of c-Si with Si^+ implantation at doses of 10^{14} cm^{-2} [23]. Other measurements of τ have been reported to be between 240 fs and 4 ps for a-Si [23, 34, 35, 86], hydrogenated a-Si [35, 87–89], nanocrystalline silicon [90], and microcrystalline silicon [91].

Relaxation time constants were related to the average displacement-per-atom (DPA) in B^+- and Si^+-implanted SOS samples [92]. The authors used a modified Kinchin-Pease model to calculate the DPA for a given ion dose, and demonstrated that the carrier relaxation time scales inversely with DPA, saturating at ~ 0.5 ps. Stolk $et.$ $al.$ conclude that the density of electrical defects saturate near 0.02 DPA, although full amorphization of a crystalline lattice occurs for much higher (0.3–1) DPA. Based on the characteristic measured relaxation times, the
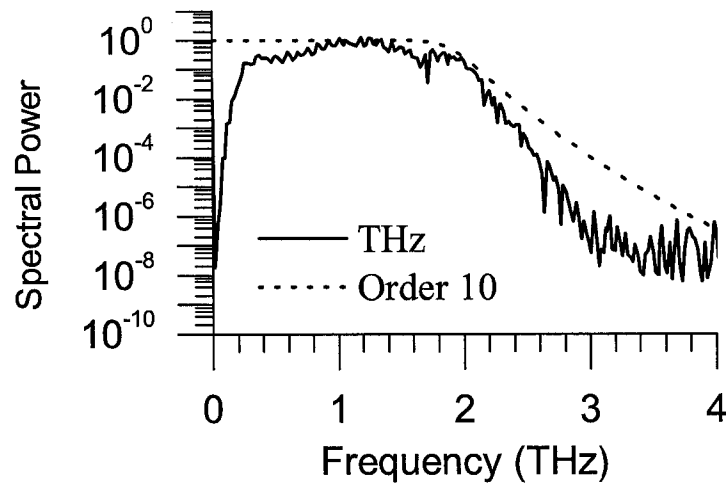
Figure 5.2: THz spectrum indicating useful bandwidth between 0.5-2.5 THz. Also shown is the order 10 Butterworth filter with a cut-off frequency of 2.0 THz.

DPA of the O^+-implanted samples can be predicted by interpolation between B^+ and Si^+ implantation in Figure 7 of Ref. [21]. Defect densities of 0.003 ± 0.001 DPA, 0.03 ± 0.01 DPA, and > 0.1 DPA for S1, S2, and S3, respectively, were found.

5.3 Effective Carrier Mobility

While a hopping-tunneling model was proposed for hydrogenated a-Si [92], a simple Drude model can be used in the non-hydrogenated a-Si sample. This is due to the continuous bonding in non-hydrogenated a-Si [21], where transport does not rely on tunneling, unlike transport in hydrogenated a-Si. Also, transport
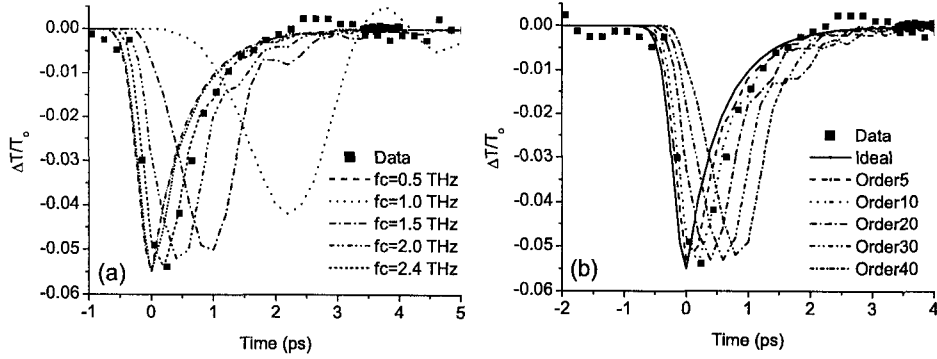
Figure 5.3: Comparison of the Butterworth filter of order 10 with (a) different cut-off frequencies f_c and (b) different filter orders. Time-domain data are shown for sample S3 pumped with a fluence of 881 $\mu J/cm^2$ at room temperature.

due to carrier diffusion in a-Si is expected to be unimportant on picosecond timescales [21, 22]. The Drude model simulated the transmissivity of the peak of the THz pulse, with μ and the maximum $\Delta T/T_o$ as fitting parameters. For the transients in Figure 5.1(a), mobility values, μ, were found to be 501 ± 9 cm^2/Vs, 46 ± 2 cm^2/Vs, and 4.7 ± 0.4 cm^2/Vs for S1, S2 and S3, respectively. The uncertainty values represent the range in which the model matched the data (for an example, see Figure 4.8).

Care should be taken when considering carrier mobility values. The *free carrier conduction mobility* (μ) is conceptually different from the *drift mobility* (μ_{drift}) [93]. The conduction mobility is used in the Drude model and is proportional to the conductivity of the sample, $\sigma = n_c e \mu$, where n_c is the carrier density, while the drift mobility, $\mu_{drift} = d^2/Vt$, is dependent on the applied voltage bias, V, the transit time across patterned electrodes, t, and the distance
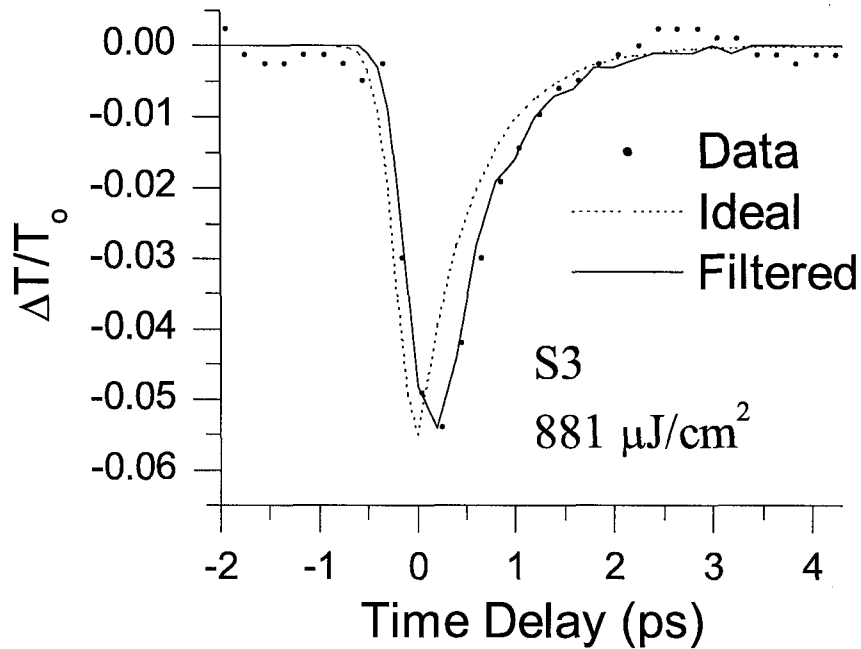
Figure 5.4: A comparison of the ideal and filtered traces with the data is shown for a pump fluence of 881 $\mu J/cm^2$ (carrier density $\sim 6.5 \times 10^{20}$ cm^{-3}) incident on the amorphous silicon thin film (S3) at room temperature.

between electrodes, d. In the presence of trapping centers, the drift mobility is expected to be significantly smaller than the conduction mobility of the free carriers [93]. The drift mobility is often reported simply as the free carrier mobility; hence the confusion. Conduction mobilities for a-Si and a-Si:H, both measured and calculated, are expected to be 1–10 cm^2/Vs [35,87,88], while drift mobilities have been reported to be 0.02–0.1 cm^2/Vs [27,94]. Measured conduction mobilities have been shown to be independent of preparation method and experimental conditions [35,89]. Previous reports on damaged SOS mobility values

(10–100 cm^2/Vs) [95] have been lower than the measurements on S1, but agree well with measurements on S2.

The damping time, τ_d, is related to the carrier conduction mobility through the Drude model: $\mu = e\tau_d/m$, where e is the elementary charge, and $m = 0.2m_e$ is the charge carrier effective mass in amorphous silicon. From the effective carrier mobility values, corresponding damping times of 57 ± 1 fs, 5.2 ± 0.2 fs, and 0.53 ± 0.04 fs for S1, S2, and S3, respectively, were deduced. This is consistent with reported values for τ_d of approximately 100 fs for crystalline Si [21], and less than 1 fs for a-Si [21,86], measured in transient reflectivity experiments.

5.4 Time-Dependence in Carrier Density

Using the fitting procedure outlined in Chapter 4, the time-dependent carrier density, $n_c(t)$, can be found for each data set. Eq. 4.3 was inverted to evaluate the carrier density given the $\Delta T/T_o$ data acquired for the samples:

$$n_c(t) = \frac{1+N}{Z_o \delta e \mu} \left[\frac{1}{\Delta T/T_o(t) + 1} - 1 \right], \qquad (5.1)$$

where $N = 3.1$ is the refractive index for sapphire in the THz range, $\delta = 0.0145 \ \mu m$ is the optical penetration depth of 400 nm light in damaged and amorphous silicon [1] and $Z_o = 377 \ \Omega$ is the impedance of free space. No phase shift of the THz pulse was observed in the excited samples (Figure 4.2), hence $\omega\tau_d < 1$, and $\sigma = n_c e \mu$ for the sample conductivity can be used in this analysis. Figure 5.1(b) shows time-resolved carrier densities for the $\Delta T/T_o$ traces given in Figure 5.1(a). The single-exponential behaviour of all three samples is consistent with non-Auger recombination dynamics [96]. Previous reports indicate a transition from trap-dominated dynamics to Auger-like recombination processes for carrier densities greater than 10^{20} cm^{-3} [97] in a-Si. My results show non-

Auger behavior at carrier densities slightly higher than this threshold, but the discrepancy may be attributed to differing degrees of amorphisation.

5.5 Fluence Dependence

Pump fluence dependences on relaxation time constant and mobility were studied in each sample at room temperature for the range 200–1000 $\mu J/cm^2$, corresponding to injected carrier densities of 1.5–7.4 $\times$ 10^{20} cm^{-3}. The $\Delta T/T_o$ traces for all three samples are shown in Figure 5.5(a), including the ideal (*i.e.* "deconvolved") $\Delta T/T_o$ traces for S2 and S3. The procedure outlined in the previous section was used to deduce exponential relaxation time constants for each sample with various carrier injections. A slight increase in the characteristic relaxation time constant was observed to increase with pump fluence for all three samples (Figure 5.6). Average relaxation time constants were 4.9 $\pm$ 0.9 ps, 1.7 $\pm$ 0.6 ps and 0.57 $\pm$ 0.05 ps for S1, S2 and S3, respectively. The lack of significant dependence of relaxation time on pump fluence indicates a single carrier relaxation pathway in these three samples for all injected carrier densities investigated, justifying the use of a single exponential time constant in the ideal $\Delta T/T_o$ traces. Carriers are believed to be trapped in mid-gap states resulting from dangling Si bonds.

The effective carrier mobility values, μ, were deduced from the $\Delta T/T_o$ traces using the Drude model, as described in Section 4.5. These values are shown for all three samples in Figure 5.6(b). The effective mobility appears to have no dependence on the injected carrier density. The average carrier mobility values were found to be 422 $\pm$ 79 cm^2/Vs, 40 $\pm$ 12 cm^2/Vs, and 4.4 $\pm$ 0.4 cm^2/Vs for S1, S2, and S3, respectively. Table 5.1 summarizes these findings.

Table 5.1: Summary of average relaxation time constants (τ), effective mobilities (μ), and damping times (τ_d) for all three samples under different pump fluences and at various temperatures. The uncertainties are one standard deviation from the average value. *S1* is the moderately-damaged silicon-on-sapphire sample, *S2* is the heavily-damaged silicon-on-sapphire sample, and *S3* is the amorphous silicon-on-sapphire sample. Since neither temperature nor fluence dependence was observed in these measurements, a total average summary is also given. In addition, the rise time constants (τ_r) for the three samples are given in the total average summary.

		Sample S1	Sample S2	Sample S3
200–1000	τ(ps)	4.9 ± 0.9	1.7 ± 0.6	0.57 ± 0.05
μJ/cm^2	μ(cm^2/Vs)	422 ± 79	40 ± 12	4.4 ± 0.4
300 K	τ_d(fs)	48 ± 9	4.6 ± 1.4	0.50 ± 0.05
5–300 K	τ(ps)	6.1 ± 0.8	1.1 ± 0.1	0.59 ± 0.12
1000 μJ/cm^2	μ(cm^2/Vs)	343 ± 109	48 ± 10	4.5 ± 0.9
	τ_d(fs)	39 ± 13	5.5 ± 1.2	0.51 ± 0.11
	τ(ps)	5.5 ± 0.9	1.4 ± 0.4	0.58 ± 0.09
Total	μ(cm^2/Vs)	383 ± 94	44 ± 11	4.4 ± 0.7
Averages	τ_d(fs)	44 ± 11	5.1 ± 1.3	0.51 ± 0.08
	τ_r(ps)	0.82 ± 0.15	0.52 ± 0.05	0.26 ± 0.03

5.6 Temperature Dependence

The procedure for finding μ and τ from the $\Delta T/T_o$ data described previously was used to interpret the temperature-dependent data. Average relaxation time constants of 6.1 ± 0.8 ps, 1.1 ± 0.1 ps, 0.59 ± 0.12 ps for S1, S2 and S3,

respectively were found (Figure 5.7(a)). No apparent temperature-dependence is seen in the characteristic relaxation times for any of the samples between 5 K and 300 K. This lends evidence to non-thermally-activated carrier transport in the samples, consistent with other reports. For instance, a temperature-independent trap capture coefficient in a-Si:H was postulated by Hattori $et.$ al. [98]. Steady-state photocurrents measured using transmission line experiments on a-Si were found to be temperature independent as well [99]. Heavily-irradiated samples of $GaAs$ were shown to exhibit temperature-independent relaxation times [100]. In addition, Pässler showed that neutrally-charged deep trap states should have no temperature dependence in capture coefficients [101–103]. Note that it is the re-emission of carriers from trap states which is thermally-activated, and may be observable in drift mobility experiments.

The effective mobility also appears to have no obvious temperature dependence (Figure 5.7(b)). Average mobility values were deduced to be 343 ± 109 cm²/Vs, 48 ± 10 cm²/Vs, and 4.5 ± 0.9 cm²/Vs for S1, S2, and S3, respectively. While at first surprising, it is possible that the effect of impurity scattering (where the mobility increases algebraically with increasing temperature [27]) may cancel that of acoustic phonon scattering (where the mobility decreases algebraically with increasing temperature). Optical phonons, which are excited during hot carrier thermalization, are expected to decay to acoustic phonons in less than 100 fs [87,89], which is less than the time resolution of the THz detection system. (Because of the small energy of the THz pulse, no phonon excitation is expected from the THz probe [104]; thus phonon generation is expected to be a result only of thermalization of photogenerated carriers.) Thus it is possible that the temperature effects of impurity scattering cancel that of acoustic phonons, yielding a temperature-independent mobility. The temperature studies on these samples are summarized in Table 5.1.

5.7 Risetimes

The fluence- and temperature-independent average risetime for S1 was measured to be 0.82 ± 0.15 ps. In addition, the Gaussian fits for the risetimes in the deconvolution algorithm were found to be independent of temperature and pump fluence for samples S2 and S3. These were measured to be 0.52 ± 0.05 ps and 0.26 ± 0.03 ps for S2 and S3, respectively (Table 5.1).

Since the pump pulse was on the order of 100 fs, the $\Delta T/T_o$ risetimes τ_R are a measure of thermalization times in these samples. These results agree with previously reported thermalization times of less than 1 ps [35].

5.8 Thermal Annealing

Pulsed laser annealing has been used to reduce stress in thin films, thereby increasing the mobility of the sample [105]. We tested this in our system and found no annealing effects due to the pump beam (Figure 5.8). On the other hand, thermally annealing sample S1 was found to significantly increase the relaxation time constant from 6.0 to 95 ps and the mobility from 343 to 650 cm^2/Vs. (Figure 5.9). The sample was annealed in vacuum at 300 and 800 °C for 20 min at each temperature. The increase in relaxation time constant and effective carrier mobility is indicative of lattice relaxation, thus reducing the density of lattice defects [95].
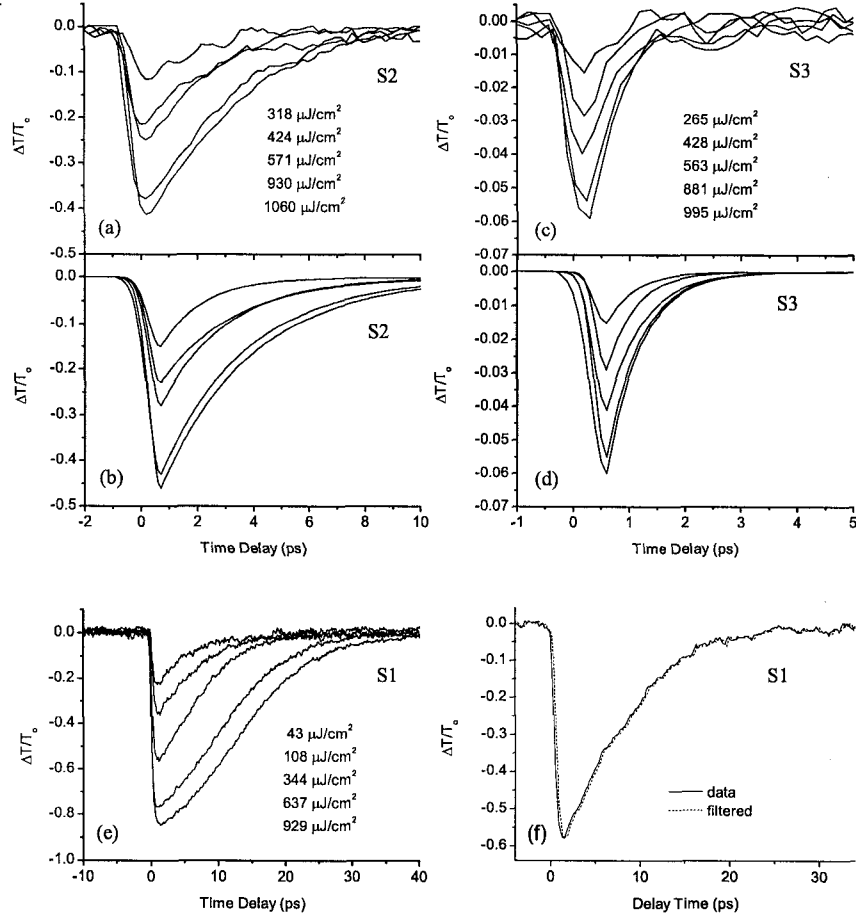
Figure 5.5: The normalised change in amplitude transmission of the THz peak $(\Delta T/T_o)$ is shown as a function of pump-probe time delay for all three samples at room temperature. (a),(c) Room temperature data and (b),(d) the corresponding ideal transients are shown for S2 and S3, respectively, for a variety of pump fluences. (e) Note the change in signal shape for a variety of pump fluences for S1; the transients are exponential at low fluences, linear at moderate fluences, and sigmoidal at high fluences. However, the excess carrier density decays with a single exponential for all fluences [1]. (f) Data for S1 was filtered with the Butterworth filter to ensure that convolution with the THz probe did not affect these traces.
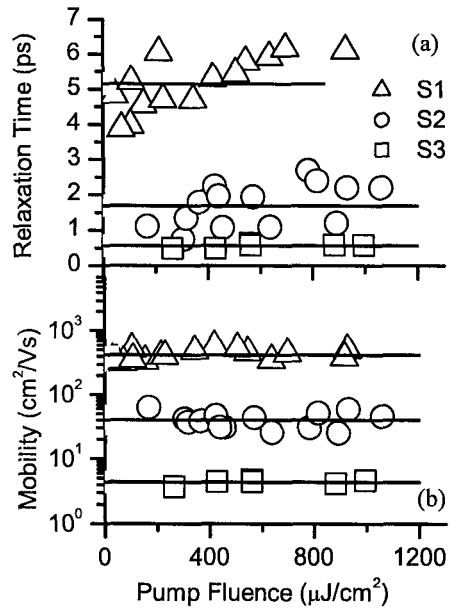
Figure 5.6:   (a) Relaxation time constants and (b) effective carrier conduction mobilities are shown as a function of pump fluence at room temperature for all three samples. The solid lines indicate the average values for each sample. Avrage relaxation times were found to be 4.9 ± 0.9 ps, 1.7 ± 0.6 ps, and 0.57 ± 0.05 ps for S1, S2, and S3, respectively. Average mobility values were deduced to be 422 ± 79 cm²/Vs, 40 ± 12 cm²/Vs, and 4.4 ± 0.4 cm²/Vs for the three samples respectively. The symbol size is representative of the uncertainties in the measurements in (a).
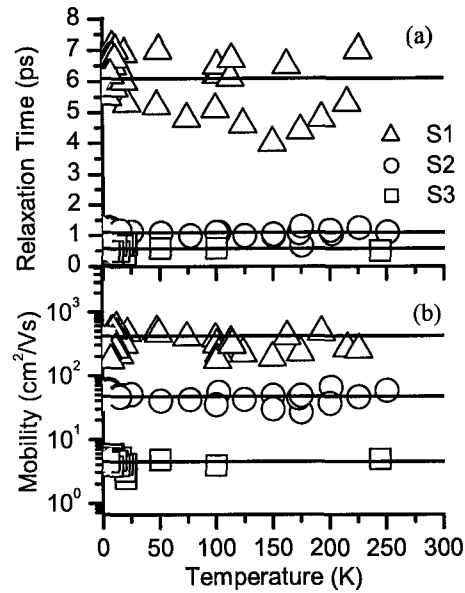
Figure 5.7: (a) Relaxation time constants and (b) effective carrier conduction mobilities are shown as a function of temperature for all three samples. The solid lines indicate the average values for each sample. Average relaxation times and mobilities were found to be 6.1 ± 0.8 ps, 1.1 ± 0.1 ps, and 0.59 ± 0.12 ps for S1, S2, and S3, respectively. Average mobility values were deduced to be 343 ± 109 cm^2/Vs, 48 ± 10 cm^2/Vs, and 4.5 ± 0.9 cm^2/Vs for the three samples respectively. The symbol size is representative of the uncertainties in the measurements in (a). Data were taken at fluences of 200 μJ/cm^2 and 400 μJ/cm^2 for S1, 300 μJ/cm^2 and 700 μJ/cm^2 for S2, and 600 μJ/cm^2 for S3.
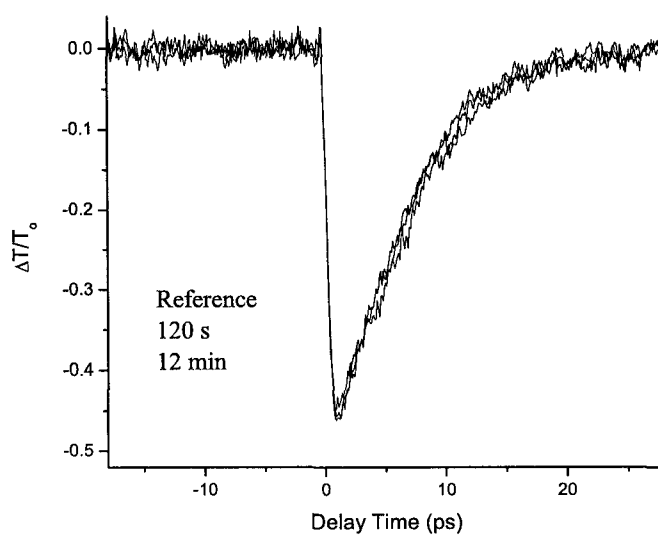
Figure 5.8: $\Delta T/T_o$ traces of S1 showing no observable annealing occurred with exposure to the pump beam for 120 s and 12 minutes.
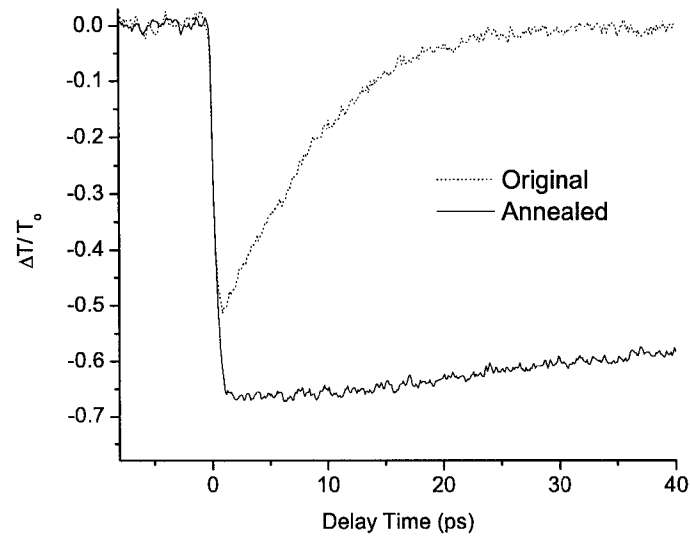
Figure 5.9: $\Delta T/T_o$ traces for sample S1 before and after thermal annealing in vacuum at 300 and 800 °C for 20 min each on the same sample. The relaxation time constant increased from 6.0 to 95 ps, while the effective carrier mobility increased from 343 to 650 cm^2/Vs.

Chapter 6

Silicon Nanocrystals in Sapphire

As size dimensions shrink, quantum effects become apparent in bulk properties, including a band gap increase and a blue-shift of absorption and luminescence spectra [106]. Furthermore, as volume decreases, surface effects become increasingly important [107]. Conductivity in nanocrystals is dependent on two length scales [106]: the Bohr radius, $a_B = \hbar^2 \epsilon / (m^* e^2)$, and the bulk mean free path, $\ell_{mfp} = v\tau_d$, where v is the carrier velocity, and τ_d is the carrier scattering time. When the length scales r are comparable to the mean free path, an effective mean free path must be considered: $\ell^{-1} = r^{-1} + \ell_{mfp}^{-1}$. If the carrier velocity in the nanocrystal is the same as that of the bulk material, then decreasing the radius of the nanocrystal, r, will decrease the carrier collision time τ_d. Since carrier mobility is proportional to τ_d, mobility is expected to decrease with decreasing size. More background information on size-dependent effects in semiconductor nanocrystals and their optical properties can be found in Appendix A.

Beard *et. al.* [106] investigated $CdSe$ nanoparticles in toluene solvent via 400 nm pump – THz probe experiments; the only published report of ultrafast dynamics in semiconductor nanocrystals using a visible pump – THz probe technique. A bi-exponential decay was observed in the relaxation time of the

nanocrystals. Their observations are consistent with other time-resolved studies of nanocrystals, where 1–3 relaxation time constants have been observed [106], and where the number of relaxation time constants does not change with nanocrystal size. The source of multiple relaxation time constants is currently under investigation. Although both electron and hole dynamics contribute to relaxation mechanisms, only holes are thought to be probed by THz radiation [108]. Thermal smearing at room temperature may contribute to the nanocrystal signal, while surface defects provide a significant source of carrer trap sites. Furthermore, carriers are governed by ballistic transport, and scatter many times before trapping by surface states. Note that visible pump – THz probe experiments on nanocrystals in solution are sensitive only to dynamics within the nanocrystal and not to those between adjacent nanocrystals [106].

Preliminary pump-probe experiments on carrier relaxation time constants in Si nanocrystals embedded in a sapphire substrate have been conducted in a manner similar to that described in Chapter 4. As far as I am aware, this is the first visible pump – THz probe study of semiconductor nanocrystals embedded in a crystalline substrate.

A change in experimental procedure was made for these experiments: the 400 nm pump beam was chopped at 540 Hz (in lieu of chopping the THz generation beam). While this improves the signal-to-noise ratio, it does not give an absolute value for the transmissivity data. Instead, ΔT is recorded; the method described in Chapter 4 would be used to record the maximum $\Delta T/T_o$ value in order to scale appropriately the ΔT data. The Si nanocrystal signal is so small as to be undetectable using the original data acquisition method. Presented here are preliminary data acquired using both methods.

Nanocrystals were formed through Si^+-implantation into a sapphire substrate at a dose of 3×10^{17} cm^{-2} and an energy of 400 keV. The substrate was kept at

$500^{o}C$ during implantation. The sample was then cut into several pieces, one of which was annealed in an Ar atmosphere at $950^{o}C$ for one hour. Other studies of Si implantation into sapphire demonstrated nanocrystal size of 4 nm when annealed at 900 ^{o}C for 30 min [109], platelets were observed after annealing a 1100 ^{o}C for 2 h.

The as-implanted sample, NC1, was investigated using the traditional pump-probe method, as described in Chapter 4, while the annealed sample, NC2, was studied using the new, chopped pump beam, setup. Approximately 8 ± 2 mW of the 400 nm pump beam was absorbed by the sample (no pinhole was used). No signal was discernible in the annealed sample (NC2) using the traditional pump-probe method (as described in Chapter 4).

Figure 6.1 shows the normalised differential transmission data for the as-implanted sample, NC1. While the signal-to-noise ratio of this data is too low for definitive results, one can see a single exponential with a time constant of 1.1 $\pm$ 0.5 ps provides the best fit to the data.

From the ΔT data for NC2 shown in Figure 6.2, taken with the pump beam chopped, several time constants can be detected. A double exponential was fitted to this data, giving a short time constant of 6.5 $\pm$ 0.4 ps and a long time constant of 75 $\pm$ 25 ps. The presence of two time constants is indicative of two carrier relaxation modes; published reports indicate the presence of 1–3 relaxation times in semiconductor nanocryrstals [106]. The slight discontinuity at 12.6 ps, as seen in the inset of Figure 6.2, is due to a backreflection of the pump beam in the sample; it was removed by subtracting the short exponential trace at time $= 0$ from the data after 12.5 ps. Since the sample will likely be used in further experiments, transmission electron microscopy has not yet been used to characterise the nanocrystal size and distribution.

As ion implantated nanocrystals tend to have a wide distribution in crystal
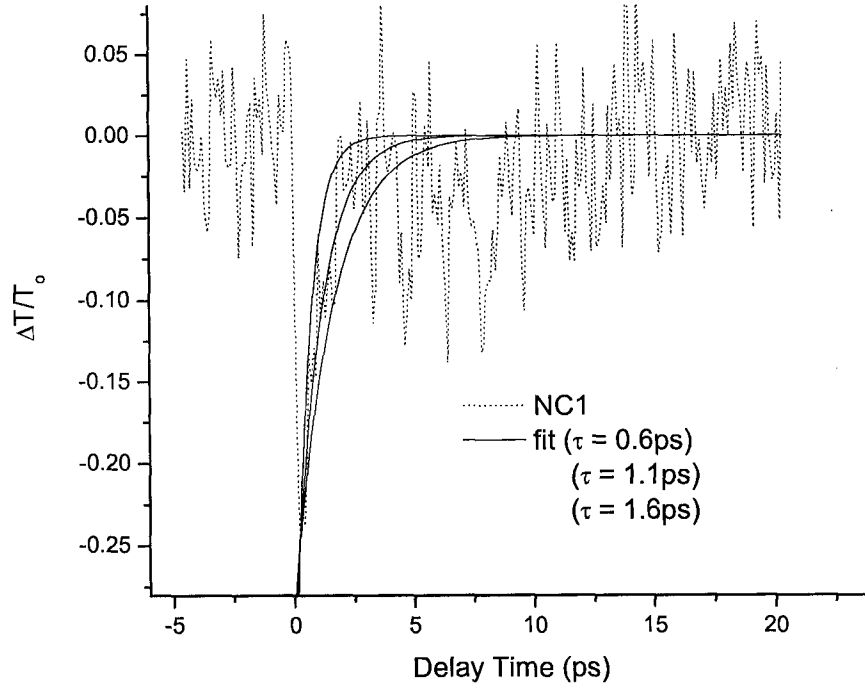
Figure 6.1: Differential transmission of the THz probe beam through as-implanted Si nanocrystals (sample NC1). Data was acquired in the traditional pump-probe method, as described in Chapter 4. A single relaxation time constant of 1.1 ± 0.5 ps was found; the single time constant is likely due to a highly amorphous, very thin Si film embedded in the sapphire substrate.

sizes, it is not surprising that a range of relaxation time constants are found for both NC1 and NC2. Since the nanocrystals are embedded within a crystalline substrate, the NCs are crystallographically aligned [109, 110]. However, the Drude model is too simplistic for nanoscale systems, thus the analysis procedure developed in Chapters 4 and 5 cannot be used to extract properties such as the relaxation time constant τ and the effective carrier mobility μ.
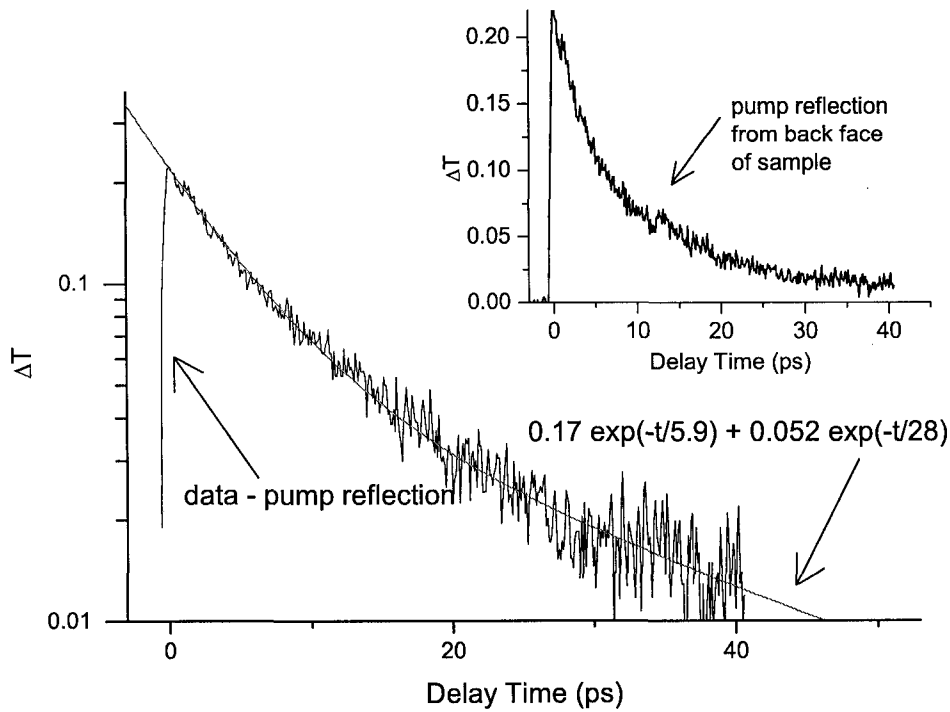
Figure 6.2:   Differential transmission of the THz probe beam through Si-implanted Al_2O_3 annealed for 1 hour at 950 $^\circ$C (sample NC2). Data was taken with the pump beam chopped at 540 Hz [2]. This sample contains two carrier relaxation mechanisms, as evidenced by the two relaxation time constants of 6.5 $\pm$ 0.5 ps and 75 $\pm$ 25 ps. The inset shows the "re-pumping" of the sample at 12.6 ps caused by reflection of the pump beam at the back face of the Al_2O_3 substrate.

While these results are preliminary, they encourage further study of the carrier dynamics in Si nanocrystals in sapphire using the 400 nm pump – THz probe experimental setup described in this document.

Chapter 7

Summary

Using a 400 nm pump - THz probe configuration in transmission mode, the carrier dynamics in radiation-damaged silicon-on-sapphire and in amorphous silicon were investigated. Since neither temperature nor pump fluence dependences were observed, the average risetime, mobility and relaxation time values are reported. Measured thermalization times were found to be 0.82 $\pm$ 0.15 ps, 0.52 $\pm$ 0.05 ps and 0.26 $\pm$ 0.03 ps for the moderately-damaged SOS (O^+-implantated at 100 keV and 200 keV, dose 1×10^{13} cm^{-2}), heavily-damaged SOS (O^+-implanted at 100 keV, dose 1×10^{15} cm^{-2}, and at 200 keV, dose 2×10^{15} cm^{-2}), and amorphous Si, respectively. Approximately decade decreases in effective carrier mobilities for the three samples were found, specifically 383 $\pm$ 94 cm^2/Vs for the moderately-damaged silicon-on-sapphire sample, 44 $\pm$ 11 cm^2/Vs for the heavily-damaged silicon-on-sapphire sample, and 4.4 $\pm$ 0.7 cm^2/Vs for the amorphous silicon sample. Carrier relaxation time constants were also found to depend on the degree of lattice damage, giving values of 5.5 $\pm$ 0.9 ps for the first sample, 1.4 $\pm$ 0.4 ps for the second sample, and 0.58 $\pm$ 0.09 ps for the third sample. While a slight increase in relaxation time was observed with increase in injected carrier density, no pump fluence dependence was seen in the carrier mobility

values for fluences between 200 and 1000 $\mu J/cm^2$. These results point to the presence of only one carrier relaxation channel in the SOS samples for injected carrier densities $< 10^{21}$ cm^{-2}. These results lend support to the deep trap model in lattice-damaged thin film systems, whereby carrier transport is influenced by lattice defects and dangling bonds acting as deep trap sites. Furthermore, the deconvolution approximation using the Butterworth filter to mimic the THz detection bandwidth limitations has been shown to be a viable technique.

In this document, I have outlined terahertz generation and detection processes, and described research projects which have used terahertz methods as a probe beam in pump-probe experiments. Furthermore, I have developed and characterised a useful terahertz system for use in the Ultrafast Spectroscopy Laboratory. Using this system, I have analysed a series of silicon-on-sapphire systems, including moderately- and heavily-damaged silicon-on-sapphire, amorphous silicon thin film on sapphire, and silicon nanocrystals. Results from the silicon nanocrystals encourage further investigation into this system. Specifically, a physical model needs to be developed to describe ultrafast carrier dynamics in these systems so as to better understand the terahertz transmission data acquired thus far. Further, a greater store of data can be collected, including varying the annealing temperature (which will change the nanocrystal size) and considering the nanocrystal samples at various temperatures. These results, however, provide a strong basis on which to continue visible pump - terahertz probe experiments in the Ultrafast Spectroscopy Laboratory.

Bibliography

[1] K.P.H. Lui and F.A. Hegmann. Ultrafast carrier relaxation in radiation-damaged silicon on sapphire studied by optical-pump terahertz-probe experiments. *Applied Physics Letters*, 78:3478–3480, 2001.

[2] D. Cooke, 2002. Private communication.

[3] C.A. Brau. Free-electron lasers. *Science*, 239:1115–1121, 1988.

[4] N.A. Ebrahim and C.R.J. Hoffman. A far-infrared free-electron laser facility for applications in basic and applied research. Technical report, Accelerator Physics Branch, Atomic Energy of Canada, Ltd., Chalk River Laboratories, 1995.

[5] D.M. Mittleman, M. Gupta, R. Neelamani, R.G. Baraniuk, J.V. Rudd, and M. Koch. Recent advances in terahertz imaging. *Applied Physics B*, 68:1085–1094, 1999.

[6] Q. Chen and X.-C. Zhang. Polarization modulation in optoelectronic generation and detection of terahertz beams. *Applied Physics Letters*, 74:3435–3437, 1999.

[7] M. Nuss. Chemistry is right for T-ray imaging. *IEEE Circuits and Devices*, March:25–30, 1996.

[8] K. Kincade. Terahertz technology may improve medical imaging. *Laser Focus World*, May:123–125, 2000.

[9] D.H. Auston. Picosecond optoelectronic switching and gating in silicon. *Applied Physics Letters*, 26:101–103, 1975.

[10] D. Côté, M. Fraser, M. DeCamp, P.H. Bucksbaum, and H.M. van Driel. THz emission from coherently controlled photocurrents in GaAs. *Applied Physics Letters*, 75:3959–3961, 1999.

[11] N.W. Ashcroft and N.D. Mermin. *Solid State Physics*. Saunders College Publishing, Orlando, Florida, 1976.

[12] S.E. Ralph, S. Perkowitz, N. Katzenellenbogen, and D. Grischkowsky. Terahertz spectroscopy of optically thick multilayered semiconductor structures. *Journal of the Optical Society of America B*, 11:2528–2532, 1994.

[13] D. Grischkowsky, S. Keiding, M. van Exter, and C. Fattinger. Far-infrared time-domain spectroscopy with terahertz beams of dielectrics and semiconductors. *Journal of the Optical Society of America B*, 7:2006–2015, 1990.

[14] M.C. Nuss, K.W. Goossen, J.P. Gordon, P.M. Mankiewich, and M.L. O'Malley. Terahertz time-domain measurement of the conductivity and superconducting band gap in niobium. *Journal of Applied Physics*, 70:2238–2241, 1991.

[15] B.I. Greene, P.N. Saeta, D.R. Dykaar, S. Schmitt-Rink, and S.L. Chuang. Far-infrared light generation at semiconductor surfaces and its spectroscopic applications. *IEEE Journal of Quantum Electronics*, 29:2302–2312, 1992.

[16] S.E. Ralph, Y. Chen, J. Woodall, and D. McInturff. Subpicosecond photoconductivity of $In_{0.53}Ga_{0.47}As$: Intervalley scattering rates observed via THz spectroscopy. *Physical Review B*, 54:5568–5573, 1996.

[17] S.S. Prabhu, S.E. Ralph, M.R. Melloch, and E.S. Harmon. Carrier dynamics of low-temperature-grown GaAs observed via THz spectroscopy. *Applied Physics Letters*, 70:2419–2421, 1997.

[18] M.C. Nuss and J. Orenstein. Terahertz time-domain spectroscopy. *MILLIMETER AND SUBMILLIMETER WAVE SPECTROSCOPY OF SOLIDS: Topics in Current Chemistry*, 74:7–50, 1998.

[19] M.C. Beard, G.M. Turner, and C.A. Schmuttenmaer. Transient photoconductivity in GaAs as measured by time-resolved terahertz spectroscopy. *Physical Review B*, 62:15764–15777, 2000.

[20] M.C. Beard, G.M. Turner, and C.A. Schmuttenmaer. Subpicosecond carrier dynamics in low-temperature grown GaAs as measured by time-resolved terahertz spectroscopy. *Journal of Applied Physics*, 90:5915–5923, 2001.

[21] P.A. Stolk, F.W. Saris, A.J.M. Berntsen, W.F. van der Weg, L.T. Sealy, R.C. Barklie, G. Krötz, and G. Müller. Contribution of defects to electronic, structural, and thermodynamic properties of amorphous silicon. *Journal of Applied Physics*, 75:7266–7286, 1994.

[22] A. Esser, H. Heesel, H. Kurz, C. Wang, G.H. Parsons, and G. Lucovsky. Femtosecond spectroscopic study of ultrafast carrier relaxation in hydrogenated amorphous silicon a-Si:H. *Journal of Applied Physics*, 73:1235–1239, 1993.

[23] X. Liu, R.O. Pohl, and R.S. Crandall. Lattice vibration of amorphous and disordered crystalline silicon. *Physica B*, 280:251–252, 2002.

[24] F.E. Doany, D. Grischkowsky, and C.-C. Chi. Carrier lifetime versus ion-implantation dose in silicon on sapphire. *Applied Physics Letters*, 50:460–462, 1987.

[25] Ch. Fattinger and D. D. Grischkowsky. Terahertz beams. *Applied Physics Letters*, 54:490–492, 1989.

[26] A.V. Shah, R. Platz, and H. Keppner. Thin-film silicon solar cells: A review and selected trends. *Solar Energy Materials and Solar Cells*, 38:501–520, 1995.

[27] D. Adler. *Amorphous Semiconductors*. CRC Press, Cleveland, Ohio, 1971. pages 27-38.

[28] A.S. Ferlauto, G.M. Ferreira, J.M. Pearce, C.R. Wronski, R.W. Collins, X. Deng, and G. Ganguly. Analytical model for the optical functions of amorphous semiconductors from the near-infrared to ultraviolet: Applications in thin film photovoltaics. *Journal of Applied Physics*, 92:2424–2436, 2002.

[29] N.A. Schultz and P.C. Taylor. Temperature dependence of the optically induced production and annealing of silicon dangling bonds in hydrogenated amorphous silicon. *Physical Review B*, 65:235207–1–8, 2002.

[30] S. Sriraman, S. Agarwal, E.S. Aydil, and D. Maroudas. Mechanism of hydrogen-induced crystallizaton of amorphous silicon. *Nature*, 418:62–65, 2002.

[31] C.W. Myles, B.C. Ha, and Y.K. Park. Large supercell molecular dynamics study of defect formation in hydrogenated amorphous silicon. *Journal of Physical Chemistry of Solids*, 63:1691–1698, 2002.

[32] Journal of Non-Crystalline Solids. *19th International Conference on Amorphous and Microcrystalline Semiconductors*, volume 299, 2002.

[33] G. Yue, D. Han, L.E. McNeil, and Q. Wang. Characteristics of the low energy photoluminescence in μc-Si films. *Journal of Applied Physics*, 88:4904–4906, 2000.

[34] S. Roorda, R.A. Hakvoot, A. van Veen, P.A. Stolk, and F.W. Saris. Structural and electrical defects in amorphous silicon probed by positrons and electrons. *Journal of Applied Physics*, 72:5145–5152, 1992.

[35] A.M. Johnson, D.H. Auston, P.R. Smith, J.C. Bean, J.P. Harbison, and A.C. Adams. Picosecond transient photocurrents in amorphous silicon. *Physical Review B*, 23:6816–6819, 1981.

[36] J.T. Kindt and C.A. Schmuttenmaer. Theory for the determination of the low-frequency time-dependent response function in liquids using time-resolved terahertz pulse spectroscopy. *Journal of Chemical Physics*, 110:8589–8596, 1999. and references therein.

[37] B.I. Greene, J.F. Federici, D.R. Dykaar, A.F.J. Levi, and L. Pfeiffer. Picosecond pump and probe spectroscopy utilizing freely propagating terahertz radiation. *Optics Letters*, 16:48–49, 1992.

[38] M.C. Nuss, D.H. Auston, and F. Capasso. Direct subpicosecond measurement of carrier mobility of photoexcited electrons in gallium arsenide. *Physical Review Letters*, 58:2355–2358, 1987.

[39] P.N. Saeta, J.F. Federici, B.I. Greene, and D.R. Dykaar. Intervalley scattering in GaAs and InP probed by pulsed far-infrared transmission spectroscopy. *Applied Physics Letters*, 60:1477–1479, 1992.

[40] M. Schall and P. Uhd Jepsen. Photoexcited GaAs surfaces studied by transient terahertz time-domain spectroscopy. *Optics Letters*, 25:13–15, 2000.

[41] M. Schall and P. Uhd Jepsen. Above-band gap two-photon absorption and its influence on ultrafast carrier dynamics in ZnTe and CdTe. *Applied Physics Letters*, 80:4771–4773, 2002.

[42] R.H.M. Groeneveld and D. Grischkowsky. Picosecond time-resolved far-infrared experiments on carriers and excitons in GaAs-AlGaAs multiple quantum wells. *Journal of the Optical Society of America B*, 11:2502–2507, 1994.

[43] R.D. Averitt and A.J. Taylor. Ultrafast optical and far-infrared quasiparticle dynamics in correlated electron materials. *Journal of Physics: Condensed Matter*, 14:R1357–R1390, 2002.

[44] R.D. Averitt, G. Rodriguez, J.L.W. Siders, S.A. Trugman, and A.J. Taylor. Conducitivity artifacts in optical-pump thz-proe measurements of $YBa_2Cu_3O_7$. *Journal of the Optical Society of America B*, 17:327–331, 2000.

[45] R.D. Averitt, G. Rodriguez, A.I. Lobad, J.L.W. Siders, S.A. Trugman, and A.J. Taylor. Nonequilbrium superconductivity and quasiparticle dynamics in $YBa_2Cu_3O_{7-\delta}$. *Physical Review B*, 63:140502, 2001.

[46] R.D. Averitt, V.K. Thorsmolle, Q.X. Jia, S.A. Trugman, and A.J. Taylor. Nonequilibrium superconductivity in $Y_{1-x}Pr_xBa_2Cu_3O_7$ thin films. *Physica B*, 312-313:86–87, 2002.

[47] F.A. Hegmann, R.R. Tykwinski, K.P.H. Lui, J.E. Bullock, and J.E. Anthony. Picosecond transient photoconductivity in functionalized pentacene molecular crystals probed by terahertz pulse spectroscopy. *Physical Review Letters*, 89:227403, 2002.

[48] F.A. Hegmann and K.P.H. Lui. Optical pump - terahertz probe investigation of carrier relaxation in radiation-damaged silicon-on-sapphire. In *Proceedings*, pages 31–41. SPIE, 2002.

[49] K.P.H. Lui and F.A. Hegmann. Fluence- and temperature-dependent studies of carrier dynamics in radiation-damaged silicon-on-sapphire and amorphous silicon. *Journal of Applied Physics*, 93:9012–9018, 2003.

[50] I. Brener, D. Dykaar, A. Frommer, L.N. Pfeiffer, J. Lopata, J. Wynn, K. West, and M.C. Nuss. Terahertz emission from electric field singularities in biased semiconductors. *Optics Letters*, 21:1924–1926, 1996.

[51] D. Grischkowsky. An ultrafast optoelectronic THz beam system. *Optics and Photonics News*, May:21–28, 1992.

[52] A.M. Johnson and D.H. Auston. Microwave switching by picosecond photoconductivity. *IEEE Journal of Quantum Electronics*, 11:283–287, 1975.

[53] P. LeFur and D.H. Auston. A kilovolt picosecond optoelectric switch and Pockel's cell. *Applied Physics Letters*, 28:21–23, 1976.

[54] G. Mourou, C.V. Stancampiano, A. Antonetti, and A. Orszag. Picosecond microwave pulses generated with a subpicosecond laser-driven semiconductor switch. *Applied Physics Letters*, 39:295–297, 1981.

[55] R.W. McGowan and D. Grischkowsky. Experimental time-domain study of THz signals from impulse excitation of a horizontal surface dipole. *Applied Physics Letters*, 74:1764–1766, 1999.

[56] J. Engholm Pedersen, S. Rud Keiding, C.B. Sørensen, P.E. Lindelof, W.W. Rühle, and X.Q. Zhou. 5-THz bandwidth from a GaAs-on-silicon photoconductive receiver. *Journal of Applied Physics*, 74:7022–7024, 1993.

[57] A. Nahata, A.S. Weling, and T.F. Heinz. A wideband coherent terahertz spectroscopy system using optical rectification and electro-optic sampling. *Applied Physics Letters*, 69:2321–2323, 1996.

[58] M. Bass, P.A. Franken, J.F. Ward, and G. Weinreich. Optical rectification. *Physical Review Letters*, 9:446–448, 1962.

[59] D.H. Auston, K.P. Cheung, J.A. Valdmanis, and D.A. Kleinman. Cherenkov radiation from femtosecond optical pulses in electro-optic media. *Physical Review Letters*, 53:1555–1558, 1984.

[60] S.L. Chuang, S. Schmitt-Rink, B.I. Greene, P.N. Saeta, and A.F.J. Levi. Optical rectification at semiconductor surfaces. *Physical Review Letters*, 68:102–105, 1992.

[61] Y.H. Jin and X.-C. Zhang. Terahertz optical rectification. *Journal of Nonlinear Optical Physics and Materials*, 4:459–495, 1995.

[62] Z. Jiang, F.G. Sun, Q. Chen, and X.-C. Zhang. Electro-optic sampling near zero optical transmission point. *Applied Physics Letters*, 74:1191–1193, 1999.

[63] G. Gallot and D. Grischkowsky. Electro-optic detection of terahertz radiation. *Journal of the Optical Society of America B*, 16:1204–1212, 1999.

[64] G. Gallot, J. Zhang, R.W. McGowan, J.-I. Jeon, and D. Grischkowsky. Measurements of the THz absorption and dispersion of ZnTe and their relevance to the electro-optic detection of THz radiation. *Applied Physics Letters*, 74:3450–3452, 1999.

[65] A. Nahata, D.H. Auston, C. Wu, and J.T. Yardley. Generation of terahertz radiation from a poled polymer. *Applied Physics Letters*, 67:1358–1360, 1995.

[66] H. Xie, W.-Y. Hsu, and R. Raj. Nonlinear optical properties of epitaxial lithium tantalate thin films. *Journal of Applied Physics*, 77:3420–3425, 1995.

[67] R. Huber, A. Brodschelm, F. Tauser, and A. Leitenstorfer. Generation and field-resolved detection of femtosecond electromagnetic pulses tunable up to 41 THz. *Applied Physics Letters*, 76:3191–3193, 2000.

[68] A. Nahata, D.H. Auston, T.F. Heinz, and C. Wu. Coherent detection of freely propagating terahertz radiation by electro-optic sampling. *Applied Physics Letters*, 68:150–152, 1996.

[69] A. Leitenstorfer, S. Hunsche, J. Shah, M.C. Nuss, and W.H. Knox. Detectors and sources for ultrabroadband electro-optic sampling: Experiment and theory. *Applied Physics Letters*, 74:1516–1518, 1999.

[70] Q. Wu and X.-C. Zhang. Ultrafast electro-optic field sensors. *Applied Physics Letters*, 68:159–161, 1996.

[71] P.Y. Han, M. Tani, F. Pan, and X.-C. Zhang. Use of the organic crystal DAST for terahertz beam applications. *Optics Letters*, 25:675–677, 2000.

[72] S.-G. Park, M.R. Melloch, and A.M. Weiner. Comparison of terahertz waveforms measured by electro-optic and photoconductive sampling. *Applied Physics Letters*, 73:3184–3186, 1998.

[73] H. Hamster, A. Sullivan, S. Gordon, W. White, and R.W. Falcone. Sub-picosecond, electromagnetic pulses from intense laser-plasma interaction. *Physical Review Letters*, 71:2725–2728, 1993.

[74] T. Löffler, F. Jacob, and H.G. Roskos. Generation of terahertz pulses by photoinization of electrically biased air. *Applied Physics Letters*, 77:453–455, 2000.

[75] H.G. Roskos, M.C. Nuss, J. Shah, K. Leo, D.A.B. Miller, A.M. Fox, S. Schmitt-Rink, and K. Köhler. Coherent submillimeter-wave emission from charge oscillations in a double-well potential. *Physical Review Letters*, 68:2216–2219, 1992.

[76] P.C.M. Planken, M.C. Nuss, K. Brener, K.W. Goossen, M.S.C. Luo, S.L. Chuang, and L. Pfeiffer. Terahertz emission in single quantum wells after coherent optical excitation of light hole and heavy hole excitons. *Physical Review Letters*, 69:3800–3803, 1992.

[77] S. Ono, T. Tsukamoto, M. Sakai, Z. Liu, H. Ohtake, H. Sarukura, S. Nishizawa, A. Nakanishi, and M. Yoshida. Compact THz-radiation source consisting of a bulk semiconductor, a mode-locked fiber laser, and

a 2 T permanent magnet. *Review of Scientific Instruments*, 71:554–556, 2000.

[78] J.N. Heyman, P. Neocleous, D. Hebert, P.A. Crowell, T. Müller, and K. Unterrainer. Terahertz emission from GaAs and InAs in a magnetic field. *Physical Review B*, 64:085202, 2001.

[79] D. Hashimshony, A. Zigler, and K. Papadopoulos. Miniature photoconducting capacitor array as a source for tunable THz radiation. *Review of Scientific Instruments*, 71:2380–2385, 2000.

[80] J. Stollery. Large aperture terahertz emitter. Technical report, Univeristy of Alberta, Physics Department 499 Report, 2001.

[81] C. Rønne, P.-O. Åstrand, and S.R. Keiding. THz spectroscopy of liquid H_2 and D_2O. *Physical Review Letters*, 82:2888–2891, 1999.

[82] P.C.M. Planken, H.-K. Nienhuys, H.J. Bakker, and T. Wenckebach. Measurement and calculation of the orientation dependence of terahertz pulse detection in ZnTe. *Journal of the Optical Society of America B*, 18:313, 2001.

[83] A.D. Slepkov, F.A. Hegmann, Y. Zhao, R.R. Tykwinski, and K. Kamada. Ultrafast optical kerr effect measurements of third-order nonlinearties in cross-conjugated *iso*-polydiacetyelen oligomers. *Journal of Chemical Physics*, 116:3834–3840, 2002.

[84] E.D. Palik. *Handbook of Optical Constants of Solids*. Academic Press, London, 1998.

[85] F. Gao, G.L. Carr, C.D. Porter, D.B. Tanner, G.P. Williams, C.J. Hirschmugl, B. Dutta, X.D. Wu, and S. Etemad. Quasiparticle damping

and the coherence peak in $YBa_2Cu_3O_{7-\delta}$. *Physical Review B*, 54:700–710, 1996.

[86] P.A. Stolk, L. Calcagnile, S. Roorda, W.C. Sinke, A.J.M. Berntsen, and W.F. van der Weg. Defects in amorphous silicon probed by subpicosecond photocarrier dynamics. *Applied Physics Letters*, 60:1688–1690, 1992.

[87] J.O. White, S. Cuzeau, D. Hulin, and R. Vanderhaghen. Subpicosecond hot carrier cooling in amorphous silicon. *Journal of Applied Physics*, 84:4984–4991, 1998.

[88] H. Fritzsche. Low temperature electronic transport in non-crystalline semi-conductors. *Journal of Non-Crystalline Solids*, 114:1–6, 1989.

[89] P.M. Fauchet, D. Hulin, R. Vanderhaghen, A. Mourchid, and W.L. Nighan, Jr. The properties of free carriers in amorphous silicon. *Journal of Non-Crystalline Solids*, 141:76–87, 1992.

[90] K.E. Myers, Q. Wang, and S.L. Dexheimer. Ultrafast carrier dynamics in nanocrystalline silicon. *Physical Review B*, 64:161309(R)-1-4, 2001.

[91] P. Uhd Jepsen, W. Schairer, I.H. Libon, U. Lemmer, N.H. Hecker, M. Birkholz, K. Lips, and M. Schall. Ultrafast carrier trapping in microcrystalline silicon observed in optical pump - terahertz probe measurements. *Applied Physics Letters*, 79:1291–1293, 2001.

[92] C.M. Fortmann. Atomic vibration mediated electronic transport in amorphous silicon. *Applied Physics Letters*, 64:3024–3027, 1994.

[93] R.H. Bube. *Electronic Properties of Crystalline Solids*. Academic Press, Orlando, Florida, 1974. pages 367-368.

[94] P.G. Le Comber and W.E. Spear. Electronic transport in amorphous silicon films. *Physical Review Letters*, 25:509–511, 1970.

[95] D.H. Auston. *Ultrafast Optoelectronics*, page 188. Springer, Berlin, 2 edition, 1993. W. Kaiser, Editor.

[96] J. Linnros. Carrier lifetime measurements using free carrier absorption transients. I Principle and injection dependence. *Journal of Applied Physics*, 84:275–283, 1998.

[97] A. Esser, K. Seibert, H. Kurz, G.N. Parsons, C. Wang, B.N. Davidson, G. Lucovsy, and R.J. Nemanich. Ultrafast recombinatio and trappig in amorphous silicon. *Physical Review B*, 41:2879–2884, 1990.

[98] K. Hattori, Y. Adachi, M. Anzai, H. Okamoto, and Y. Hamakawa. Modulated photoconductivity study of charged and neutral defects in undoped amorphous silicon. *Journal of Applied Physics*, 76:2841–2850, 1994.

[99] P. Popović, E. Bassanese, F. Smole, J. Furlan, S. Grebner, and R. Schwarz. Numerical analysis of the transient response in amorphous silicon. *Journal of Applied Physics*, 82:4504–4507, 1997.

[100] J. Mangeney, N. Stelmakh, F. Aniel, P. Boucaud, and J.-M. Lourtioz. Temperature dependence of the absorption saturation relaxation time in light- and heavy-ion-irradiated bulk GaAs. *Applied Physics Letters*, 80:4711–4713, 2002.

[101] R. Pässler. Temperature dependences of nonradiative multiphonon carrier capture and ejection properties of deep traps in semiconductors .1. theoretical results. *Physica Status Solidi B*, 85:203–215, 1978.

[102] R. Pässler. Intermediate-temperature dependences of the nonradiative multiphonon carrier-capture cross-sections of deep traps in semiconductors. *Physica Status Solidi B*, 86:K39–K44, 1978.

[103] R. Pässler. Simple approximation for temperature dependences of nonradiative multiphonon carrier-capture cross-sections of deep traps in semiconductors. *Physica Status Solidi B*, 86:K45–K47, 1978.

[104] A. Debernardi, M. Bernasconi, M. Cardona, and M. Parrinello. Infrared absorption in amorphous silicon from *ab initio* molecular dynamics. *Applied Physics Letters*, 71:2692–2694, 1997. and references therein.

[105] Y. Kobayashi, M. Nakamura, and T. Suzuki. Effect of heat treatment on residual stress and electron Hall mobility of laser annealed silicon-on-sapphire. *Applied Physics Letters*, 40:1040–1042, 1982.

[106] M.C. Beard, G.M. Turner, and C.A. Schmuttenmaer. Size-dependent photoconductivity in CdSe nanoparticles as measured by time-resolved terahertz spectroscopy. *Nano Letters*, 2:983–987, 2002.

[107] V.I. Klimov, Ch.J. Schwarz, D.W. McBranch, C.A. Leatherdale, and M.G. Bawendi. Ultrafast dynamics of inter- and intraband transitions in semiconductor nanocrystals: Implications for quantum-dot lasers. *Physical Review B*, 60:R2177–R2180, 1999.

[108] C. Schmuttenmaer, 2003. Private communication.

[109] S. Yanagiya and M. Ishida. Optical and electrical properties of Al_2O_3 films containing silicon nanocrystals. *Journal of Electronic Materials*, 28:496–502, 1999.

[110] C.W. White, J.D. Budai, S.P. Winthrow, S.J. Pennycook, D.M. Hembree, D.S. Zhou, T. Vo-Dinh, and R.H. Magruder. Oriented Si and Ge nanocrystals formed in Al_2O_3 by ion implantation and annealing. *Materials Research Society Symposium Proceedings*, 316:487–491, 1994.

Appendix A

Semiconductor Nanocrystals

Nonlinear Optical Properties

This appendix originally appeared as a paper for the class EE644: Nonlinear Optics. It is included here as background for semiconductor nanocrystals and possible future research of their nonlinear optical properties in the Ultrafast Spectroscopy Laboratory. As far as I know, it is the only comprehensive review of nonlinear optical properties of semiconductor nanocrystals.

A.1 Introduction

Small crystallites of both metals and semiconductors provide a physical size regime between that of atomic systems and bulk matter, where the carrier concentration is inherently limited to very low densities [1]. Figure A.1 shows a transmission electron microscope photograph of a semiconductor nanocrystal [2]. While nanocrystals have been unknowingly used for centuries to add colour to

stained glass [3], it was not until the last few decades that nanocrystals have been studied for their interesting physical properties.
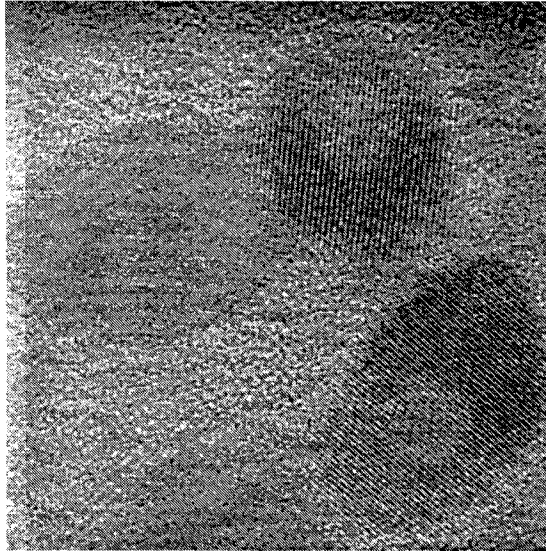
Figure A.1:   A transmission electron microscope image of CdSe nanocrystals in a glass host. The nanocrystals are approximately 10 nm across [2].

Both metal and semiconductor nanocrystals were predicted to have enhanced optical nonlinearities due to quantum confinement [4]. However, metal nanocrystals exhibit surface plasmon resonance at the same energies as those which produce enhanced nonlinearities. This makes metal nanocrystals less useful for applications.

In 1982, Efros and Efros [5] predicted the blueshift of the energy gap of quantum confined semiconductors. This paved the way for further investigation of small physical systems. Other work indicated enhanced nonlinearities in these microcrystallites [6–8]. Energy gap shifts, induced absorption, photobleaching, and other unexpected nonlinear effects were already being measured [3, 9].

A working definition for nanocrystals requires quantum confinement and crystalline alignment of the atoms within a nanoparticle [8]. Generally speaking, the size of the nanocrystal is on the order of an excited electron-hole pair (*exciton*) Bohr radius, a_{exc} [1]. Nanocrystals are also referred to as quantum dots, quantum crystals and microcrystallites in published literature; for the purposes of this review, these terms will be used interchangeably and the subtle differences in the meaning of these terms will be ignored.

This appendix reviews nonlinear optical studies of semiconductor nanocrystals. It will begin with a brief overview of some methods used to fabricate semiconductor nanoparticles. The predicted third order nonlinearities will be outlined for various important size regimes. Experiments which measure third order nonlinearities will be described, and some current research will be summarised. Optical nonlinearities not described by the suspectibility representation will also be introduced. Some final words on the current status and future directions of this research area will conclude the appendix.

A.2 Fabrication Techniques for Nanocrystals

Many techniques have been adopted to produce nanometer-scale semiconductor crystals. Several methods will be described briefly in this section.

Nanocrystals were made from powdered mixtures of the host and semiconductor material in early works (for example, see Refs. [3] and [10]). The powders used the Bridgman method to melt and form crystals. For an example [10], $CuCl$ nanocrystals in a $NaCl$ host were made using this technique.

Magnetron sputtering ejects material from a target through ion bombardment, typically using Ar ions, to form thin films [11]. A target containing $InAs$ and SiO_2 was radio-frequency sputtered and thermally annealled to form nanocrystals [12, 13]. This sample contained a large size distribution. Films with

a smaller size distribution were produced by sputtering a target of SiO_2 containing a fixed volume percent of polycrystalline $InAs$ and the film was not treated thermally [12].

Gas phase condensation precipitated GaAs nanocrystals into porous Vycor glass [14]. Gaseous trimethylgallium was introduced into the porous glass (with pore sizes of 40 $\overset{\circ}{A}$), followed by the introduction of arsine with heat. The gases flow into the pores of the glass host, and react chemically to form GaAs upon further heating. Metal-organic chemical vapour deposition has also been used to form nanocrystals in Vycor glass [15].

Laser ablation has also been used to make nanocrystalline samples [16]. A laser is focused onto a target of the material to be used in the sample, creating a small plasma in the region near the incident spot. [17] This technique can be used to form thin films or nanocrystals of almost any material, unlike more conventional processes. However, the size distribution of nanocrystals made using laser ablation tends to be quite large [16].

Thin films grown with molecular beam epitaxy are patterned and lithographed to form nanocrystals [18]. For example, a thin layer of $ZnSe$ was deposited onto a $GaAs$ substrate, followed by a 10 nm layer of $Cd_{0.20}Zn_{0.80}Se/$ $ZnSe$, and capped with a final layer of $ZnSe$. Conventional lithographic techniques was used to etch the quantum dots into the layered structure.

Ion-implantation can produce nanocrystals within a variety of host materials [4]. Ions of almost any material are bombarded at doses of 10^{13} cm^{-2} to 10^{20} cm^{-2} into any other material host. Thermal annealing bonds small clusters of these ions into crystallites. Ion-implantation is a versatile technique in that any material could be used; however, large size distributions of nanocrystals result from this process.

A.3 General Features of Nanocrystals

A.3.1 Quantum Confinement

The small size of nanocrystals necessitates the use of quantum mechanics in the description of their properties. Indeed, quantum confinement is the dominant source of unique properties for nanocrystals. Energy transitions within isolated atoms appear as sharp spectral lines [19] and are described by the archetypal particle-in-a-box quantum mechanical model. In bulk solid materials, on the other hand, interactions with neighboring atoms give rise to bands of allowed energies where individual levels overlap and form a near-continuous range of states. Band theory is used for bulk systems, introducing near-parabolic conduction and valence bands near wave vector $\vec{k} = 0$ which are separated by an energy gap E_g [20]. The effective electron (hole) mass, m_e (m_h), is defined by the curvature of the parabolic conduction (valence) band. Semiconductor nanocrystals embedded in an insulating matrix experience a potential barrier at the interface, and so the energy levels within a nanocrystal are quantised. However, because of atom-atom interactions within a nanoparticle, these discrete energy levels are smeared in a bulk-like manner.

While the eigenstates for electron-hole pairs in a rigid spherical potential are not analytically solveable [6], Efros and Efros [5] used a centre-of-mass approximation to derive general results due to quantum confinement. Excitations which create excitons have an energy in the quantum confined system of: [6, 7]

$$E = E_g - E_{exc} + A \left(\frac{\pi}{a}\right)^2 \frac{\hbar^2}{2(m_e + m_h)}. \tag{A.1}$$

E_{exc} is the bulk exciton binding energy [1]. The blueshift of the energy level, given in the third term on the right-hand side of equation A.1, depends on the effective masses of the electrons and holes and on the nanocrystal size a. For

spheres, a is the radius, while for a cubic box, a is the length of one side. The coeffecient A is a parameter which accounts for size distribution; $A = 1$ for a single size of nanocrystals, while $A < 1$ for a range of sizes. The size extensions (*i.e.* the Bohr radii) of the electron and hole are given by: [5]

$$a_e = \frac{\hbar^2 \epsilon}{m_e e^2},$$ (A.2)

$$a_h = \frac{\hbar^2 \epsilon}{m_h e^2},$$ (A.3)

where ϵ is the dielectric function for wave vector $k = 0$. There was some experimental indication that the nanocrystalline effective masses are not equal to that of the bulk case [21]. However, most groups have used only the bulk effective masses in subsequent analyses.

Several sources for optical nonlinearity in nanocrystals have been proposed. A very large optical nonlinearity in semiconductor nanocrystals is attributed to the competition between the size quantisation of the excitons and the deviation of the energy bands from the ideal harmonic oscillator representation [7]. The anharmonic oscillator source of nonlinearity dominates for smaller crystallites, leading to an increasing nonlinearity for decreasing nanoparticle size. An enhanced nonlinearity was expected to be less significant for III-V than for II-VI semiconductors. The larger effective mass, and therefore a larger deviation from an ideal harmonic oscillator band, and smaller gap energy for II-VI semiconductors are thought to contribute to the large nonlinearity. On the other hand, Schmitt-Rink, Miller and Chemla [8] discuss a strong optical nonlinearity given for very small nanocrystals due to saturation of the upper energy level in a two-energy-level model for a single nanocrystal. This *saturation nonlinearity* was expected to be more readily achievable for III-V semiconductors. These materials have larger bulk exciton Bohr radii, allowing for larger absolute nanocrystal

sizes while maintaining the 'smallness' of the nanocrystal.

It is interesting to note that the inclusion of the Stark Effect, where Coulomb and surface energies are considered, the large expected shift in the energy band is significantly reduced [9]. However, the electro-optic effect in nanocrystals remains a poorly understood phenomenon.

A.3.2 Energy Level Broadening

Sources of Level Broadening

For nanocrystals, the atomic energy levels are broadened by the crystallite structure, but not to the degree of creating the bulk energy bands. The natural linewidth of a nanocrystal will increase with decreasing size [8]. Perturbations to the band structure of nanocrystals may lead to further broadening of energy levels. Examples of perturbations include irregular nanocrystal shape, random crystallographic orientation of crystallites, stoichiometric fluctations, and surface impurities. The dominant sources of level broadening are electron-phonon coupling and size distribution. This discussion will be restricted to spherical nanocrystals with isotropic crystallographic orientation.

Electron-phonon coupling introduces a *homogeneous level broadening* [3, 8]. This is an intrinsic source of level broadening and is temperature-dependent. The strength of the electron-phonon coupling is characterised by the Huang-Rhys parameter, $S = \Delta E / \hbar \omega_{LO}$, where ΔE is the energy shift between the electronic level and the hole level, and $\hbar \omega_{LO}$ is the energy of the optical phonon [22]. For $S \gg 1$ a strong coupling exists, while for $S \ll 1$ there is weak coupling between the electron and the phonon. The smaller a crystallite is, the greater the overlap between the electron and hole wavefunctions, decreasing the electron-phonon coupling strength [3]. However, reducing the nanocrystal size also increases electron coupling to shorter wavelength phonons. Thus S is size independent when

the phonon quantisation is taken into account. The creation of phonon sidebands in the energy spectrum, which tends to be masked by the band structure in bulk systems, is expected to be important in the case of nanocrystals. A quantum mechanical model for the phonon contribution to homogeneous line broadening was first introduced by Schmitt-Rink, Miller, and Chemla [8].

A natural size distribution for nanocrystals results from the fabrication process. This size distribution leads to an *inhomogenous broadening* of energy levels. Inhomogeneous broadening is inversely proportional to the size of the nanocrystal [1]. Different subbands in the energy spectrum are broadened by different amounts, leading to a more pronounced overall smearing of the exciton bands.

Measurements of Level Broadening

Spectal hole burning experiments have been widely used to measure the amount of homogeneous level broadening [10, 23, 24]. It is characterised by a dip in the absorption spectrum at a particular energy [10] (Fig. A.2(a)). The broadness of an energy level is indicative of the characteristic exciton lifetime in that level [10]. Figs. A.2(b) and (c) indicate that the homogeneous linewidth, Γ_{hom} is proportional to the square of the temperature T and to the inverse square of the nanocrystal radius a, $\Gamma_{hom} \propto T^2/a^2$.

Since inhomogeneous level broadening is temperature-independent, it can be isolated from the temperature-dependent electron-phonon coupling in luminescence or Raman experiments [1]. Furthermore, an overal broadening of the absorption peak as compared with the bulk case is indicative of the amount of inhomogeneous broadening.

Because the majority of the spectral weight for III-V semicondcutors rests mainly in the zero-optical phonon line, rather than in sidebands, Schmitt-Rink and colleagues speculated [8] that the strong confinement regime is more real-
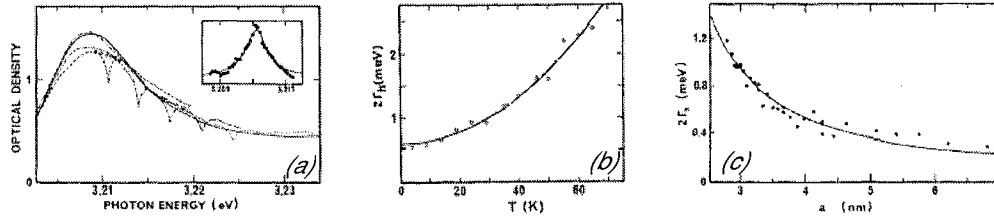
Figure A.2: (a) Spectral hole burning, characterised by depressions in the absorption spectrum of CuCl nanoparticles, are apparent in five locations labelled A - E. The solid line is the linear absorption spectrum. The homogeneous linewidth $(2\Gamma_h)$ was measured to be proportional to the square of the temperature (b), and to the inverse square of the nanocrystal size (c) as shown by solid lines. From [10].

isable than for other semiconductors. A larger absolute nanocrystal size would still exhibit quantum confinement properties. Furthermore, they had estimated that for 50 $\mathring{A}$ GaAs nanocrystals the linewidth due to phonon-coupling at room temperature should be nearly the same as that of the bulk.

A.4 Nonlinear Susceptibility

A.4.1 Confinement Regimes

For bulk semiconductors, carrier interaction must be phonon-mediated to conserve momentum [20]. In nanocrystals, however, a finite confinement potential at the nanocrystal-matrix interface allows for forbidden transitions [8] since the electron and hole wavefunctions penetrate this barrier by different amounts. Non-phonon-mediated transitions are therefore allowed in nanoparticles.

Consider a spherical nanocrystal with radius a. Three distinct size regimes can be defined [3], each having different sources of optical nonlinearities. In

the *strong confinement regime*, where $a < a_h < a_e$, the electron and hole wave-functions are decoupled, leaving them as nearly free particles. The *intermediate confinement regime*, $a_h < a < a_e$, couples the electron and hole states; the electron remains in the strong confinement regime. Finally, the *weak confinement regime*, $a_h < a_e < a$, has some similarities to the bulk properties. Sources of nonlinearities differ between these different size regimes.

Main sources of optical nonlinearities include saturation, Coulomb-mediated and impurity-mediated nonlinearities [3]. These sources of nonlinearity will be examined in the following sections within each of the confinement regimes. Because it is not quantatively well-understood, impurity-mediated nonlinearity will be neglected. For isotropic nanocrystals (samples without long-range ordering) the second order nonlinearity averages to zero. Therefore, only the third order nonlinearity $\chi^{(3)}$ will be considered here. Predictions for $\chi^{(3)}$ are mostly based on a two-energy level system, with the unexcited ground state, $|0\rangle$, and the excited state, or the exciton, $|1\rangle$.

A.4.2 Strong Confinement and Saturation Nonlinearity

In the strong confinement regime, large gaps exist between allowed energy levels. Screening is more difficult in this case. Moreover, nanocrystals are so small in this regime that polarisation of the exciton is difficult [8]. Therefore Coulomb effects are less important here, and will be neglected in the ensuing discussion. In this size regime, the energy band gap shift given in Eq. A.1 is characterised by $A = 0.71$ [5]. The third order susceptibility, $\chi^{(3)}$, is dominated by a saturation nonlinearity [3]: for isolated transitions between electron states and hole states, the purely two-level system can be saturated, yielding a bleached state.

Consider energies near the 1s-1s transition (the first electron-hole excited state) in a two-level system and a nanocrystal with size a. Ignoring line broad-

ening and Coulomb effects, the general susceptibility $\chi(\omega, I)$ can be written as: [3]

$$\chi(\omega, I) = \frac{1}{V} \left| \frac{ep_{cv}}{m\omega} \right|^2 \frac{1}{\hbar} \frac{1}{\omega_1 - \omega - i/T_2} \frac{1 + (\omega_1 - \omega)^2 T_2^2}{1 + (\omega_1 - \omega)^2 T_2^2 + I/I_s}, \tag{A.4}$$

where the first excited state energy $\hbar\omega_1$ is shifted from the bulk band gap energy E_g because of quantum confinement by:

$$\hbar\omega_1 = E_g + \hbar^2\pi^2/2\mu a^2. \tag{A.5}$$

Note that this derivation does not account for the exciton binding energy as was the case in Eq. A.1. Further more, the reduced mass, μ is considered, not the total electron and hole masses, in the strong confinement regime. The total mass is used in the case of weak confinement (Sec. A.4.4). In Eq. A.4, I_s is the saturation intensity:

$$I_s = \left| \frac{m\hbar\omega}{ep_{cv}} \right|^2 \frac{nc}{8\pi T_1 T_2}. \tag{A.6}$$

In these expressions, p_{cv} is the momentum coupling matrix element between the electron and the hole, μ is the electron and hole reduced mass, T_1 is the energy lifetime and T_2 is the excited energy level dephasing time. A low intensity Taylor expansion of Eq. A.4 around $I = 0$ yields the linear and the nonlinear susceptibilities, $\chi^{(1)}$ and $\chi^{(3)}$:

$$\chi^{(1)}(\omega) = \frac{1}{V} \left| \frac{ep_{cv}}{m\omega} \right|^2 \frac{1}{\hbar(\omega_1 - \omega - i/T_2)}, \tag{A.7}$$

$$\chi^{(3)}(\omega) = \frac{-i}{V} \left| \frac{ep_{cv}}{m\omega} \right|^4 \frac{T_1 T_2^2}{\hbar^3 (1 + i(\omega_1 - \omega)T_2)(1 + (\omega_1 - \omega)^2 T_2^2)}. \tag{A.8}$$

Around each resonant energy level in the nanocrystal $\hbar\omega_{1s}$, there is one contribution of Eq. A.8. This can be summed up for all resonances with a degeneracy

weighting factor to give the total third order nonlinear susceptibility. The real and imaginary parts of $\chi^{(3)}$ are shown in Fig. A.3(a).

(a)   (b)

(c)   (d)
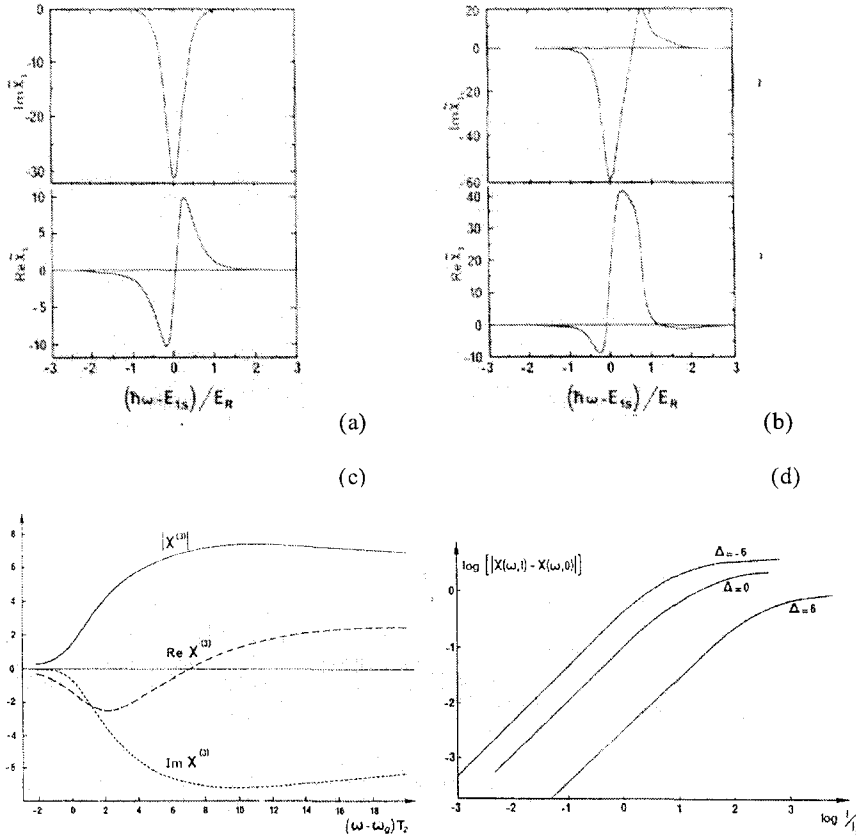
Figure A.3:   Real and imaginary parts of the third order susceptibility $\chi^{(3)}$ for (a) strong confinement $(a < a_h < a_e)$, (b) intermediate confinement $(a_h < a < a_e)$, and (c) weak confinement $(a_h < a_e < a)$ size regimes for a single quantum crystal as a function of energy. E_{1s} is the energy of a single exciton state, E_R is the exciton binding energy, and T_2 is the dephasing time of the exciton level. Coulomb effects in the intermediate confinement regime changes the shape of $\chi^{(3)}$ drastically when compared with the pure saturated nonlinearity case in the strong confinement regime. (d) Intensity saturation of $\chi(\omega, I)$ for various laser detunings, $\Delta = (E_g/\hbar - \omega)T_2$. From [3].

A.4.3 Intermediate Confinement Regime

In the *intermediate confinement regime* $a_h < a < a_e$, the nanocrystal size is between the Bohr radii of the eletrons and holes. The kinetic energy of the electron is quantized due to confinement, and interactions between a hole and the electron potential confines the hole to a well-localised area within the crystal [7]. In other words, the barrier at the nanocrystal-host interface causes a standing wave electronic state, which in turn localises the hole [25]. The inclusion of Coulomb interaction between electrons and holes are important effects in this size regime. Coulomb interaction between two photoexcitation states, *bi-excitons*, cannot be derived analytically. However, the problem can be simplified by neglecting the size-dependent lattice structure rearrangements and the surface states [25], giving a useful expression for $\chi^{(3)}$ for energies near the 1s-1s transition: [3]

$$\chi^{(3)} = -\frac{i\tau^3}{4V} \left(\frac{4A^2}{[1 + iC\tau][1 + C^2\tau^2]} - B^2 \left[\frac{2}{[1 + iD\tau][1 + C^2\tau^2]} \right. \right.$$
$$\left. \left. + \frac{1}{[1 + iC\tau][1 + iE\tau]} \left(\frac{1}{1 + iD\tau} - \frac{1}{1 + iC\tau} \right) \right] \right),$$

$$(A.9)$$

where τ is the phenomenological relaxation time, and A and B are the dipole matrix elements coupling the ground state with the one-exciton level $|1\rangle$ and two-excitons $|2\rangle$ levels, respectively:

$$A = |\langle 0|P|1\rangle|^2, \qquad (A.10)$$

$$B = |\langle 0|P|1\rangle\langle 1|P|2\rangle|, \qquad (A.11)$$

and energy differences are given by C, D, and E:

$$C = \omega_1 - \omega, \tag{A.12}$$

$$D = \omega_2 - \omega_1 - \omega, \tag{A.13}$$

$$E = \omega_2 - 2\omega, \tag{A.14}$$

where ω_1 and ω_2 are the transitions for one and two excitons, respectively. The linear susceptibility $\chi^{(1)}$ for the intermediate case is similar to Eq. A.7.

Note that τ is a phenomenological parameter which is used to simplify Coulomb interactions. Also B and ω_2 are difficult to evaluate and to measure. The crux of Eq. A.9 is the asymmetry introduced above and below the first exciton energy, $\hbar\omega_1$, as seen in Fig. A.3(b). To understand the dynamics in the intermediate confinement range, the two-level model must be extended to include bi-excitonic states.

A.4.4   Weak Confinement Regime and Coulomb-Mediated Nonlinearity

For the *weak confinement regime* $a_h < a_e < a$ the confinement pontential becomes important when compared with the electron-hole interaction energies. The band energy shift given in Eq. A.1 is characterised by $A = 0.67$ [5] in this case. Recall that the equation is similar to that of the strong confinement case, except that the total electron and hole mass is important here. The shape of the crystal is less important and one can simply use a particle-in-a-box quantum mechanical model to represent the system [3]. The energy levels are quantised, and are blueshifted with respect to the bulk energy bands according to Eq. A.1.

Considering only transitions conserving the wave vector $\vec{k}$ (momentum conservation), the susceptibility is given by: [3]

$$\chi(\omega, I) = \left| \frac{ep_{cv}}{m\omega} \right|^2 \frac{1}{\hbar \pi^2} \int_0^\infty \frac{p_v(k) - p_c(k)}{\omega_{cv}(k) - \omega - i/T_2} g(k) k^2 dk, \qquad (A.15)$$

where the Fermi-Dirac populations are given by $p_v(k)$ for holes and $p_c(k)$ for electrons. The real and imaginary susceptibilities are shown in Fig. A.3(c). In the weak confinement regime, the susceptibility saturates at the same intensity as the for the strong confinement regime, given by Eq. A.6. This is illustrated in Fig. A.3(d). Coulomb interactions would redshift the energy bands and would change the relaxation times because of Auger processes [3]. Belleguie and Banyai reported previously derived $\chi^{(3)}$ with Coulomb interactions between excitons [6].

Hanamura considered only Coulomb-mediated nonlinearities [7] and showed that enhanced nonlinearity could be achieved only for the weak-confinement case. Furthermore the exciton-exciton interaction energies had to be significant, $\hbar\omega_{int} > |\hbar\omega - \hbar\omega_o|$, where $\hbar\omega_o$ is the 1s-1s transition energy, and $\hbar\omega$ is the pump energy. A strong nonlinearity dependence on the concentration of nanocrystals exists in the weak confinement regime; the other regimes were found to be independent of concentration. Further details of the quantum mechanical derivation of the nonlinear susceptibility can be found in Ref. [7].

Interestingly an ideal-boson model for excitons in nanocrystals leads exactly to a zero nonlinearity [6]; nonlinear effects can only occur through the recognition of the exciton as a composite particle with a binding energy and a bond length. Furthermore, a numerical difference between a single-beam excitation situation and a pump-probe setup were predicted [6]. Fig. A.4 shows these two cases and includes exciton-exciton interactions. Note that the qualitative nature of both the real and imaginary parts for all cases are similar. Belleguie and Banyai caution that the predictive ability of the theory for weak confinement is tenuous

because of its sensitivity to volume-dependent parameters.
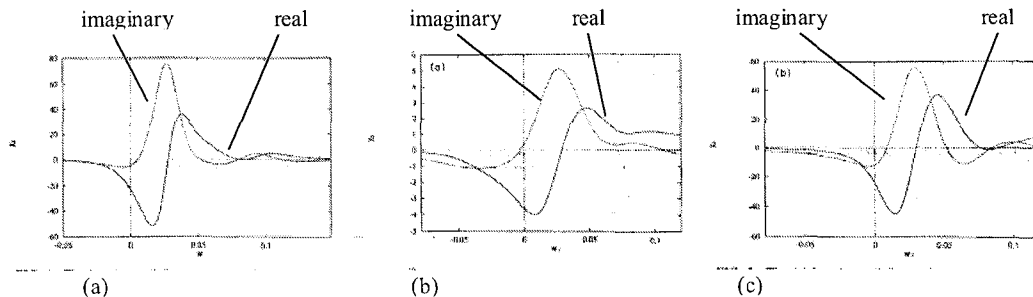
Figure A.4: Real (solid lines) and imaginary (dotted lines) for $\chi^{(3)}$ including exciton-exciton interactions for single-beam excitation (a), and pump-probe setup with pump energies of $w_{pump} = -0.5$ (b) and $w_{pump} = +1.0$ (c). Pump energies are normalised to the bulk excitonic binding energy such that $w_{pump} = (\hbar\omega - (E_g - E_{exc})/E_{exc}$. The particle size in each case is $a = 10a_{exc}$. From [6].

A.4.5 Local Field Effects

It should be noted that in the derivations above, a uniform field was assumed inside the nanocrystal. For semiconductor spheres, this is a valid assumption [8]; however, deviations from a spherical nanocrystal will affect the local electric field inside the nanocrystal, and thus alter its nonlinear optical response. No analytical solution for the field inside an arbitrary shape is possible, but the field can be approximated for some simple shapes using a local field factor F: [8]

$$F = |1 + f(\epsilon - 1)|^{-2}, \qquad (A.16)$$

where f is a parameter containing depolarisation effects. Changes in the incident intensity will affect the local field inside the nanocrystal. This will then affect the

induced nonlinearity, further altering the local field. This feedback mechanism can lead to optical bistability within nanocrystals, approximated by:

$$\frac{\epsilon_{2_0} - \epsilon_2}{\epsilon_2} = \frac{FI}{(1 + \delta^2)I_s}.$$

(A.17)

In other words, the normalised change in the imaginary dielectric function is related to the effective intensity inside the nanocrystal, FI normalised to the saturation intensity $I_s(\delta)$ at the detuning frequency δ. Non-uniform fields are suspected to contribute to energy level broadening [9].

A.4.6 Techniques to Measure $\chi^{(3)}$

Z-Scan Measurements

Two techniques commonly used to measure nonlinear coefficients are *Z-scan* and *degenerate four-wave mixing* (DFWM). The Z-scan technique, shown in Fig. A.5(a), measures the two-photon absorption coefficient and the nonlinear refractive index. [26, 27] In this experiment, phase distortion transforms into an amplitude distortion as the sample passes through the focus of a Gaussian beam. The intensity irradiating the sample is dependent on the sample location with respect to the focal point of the beam, $z = 0$ for samples thinner than the diffraction length of the focused beam. The transmittance is measured through an aperture beyond the focal point. Before the focus, at $-z$, self-focussing in a sample with $n_2 < 0$ collimates the beam, while after the focus, $+z$, self-focussing diverges the beam [26]. A lower transmittance would be measured for the $+z$ case than for the $-z$ case, so the shape of the signal as a function of z indicates the sign of the nonlinearity. Calculated traces for a third order nonlinearity are given in Fig. A.5(b). The near-field and far-field transmittance can be monitored through open-aperture and a closed-aperture detection, respectively [27]. The

peak-to-valley transmittance ΔT is related to the change in the nonlinear index Δn for the case of small phase distortion and a small aperture by:

$$\Delta T \simeq 0.406(1 - s)^{0.25} k \Delta n \left(\frac{1 - e^{-\alpha L}}{\alpha} \right).$$ (A.18)

where s is the aperture size; for example, $s = 1$ indicates an open aperture, and $s = 0.35$ indicates a 35% open aperture. The effective length is given by the linear absorption coefficient, α, and the actual length of the sample, L, in $(1 - e^{-\alpha L})/\alpha$. The change in refractive index is given by $\Delta n = \gamma I$. In the case of no multiphoton absorption and no absorption saturation, there will be inversion symmetry about the $z = 0$ point in the transmittance plot. Fifth order effects were derived to have to be of the same form as Eq. A.18 but with a prefactor 0.21. Asymmetrical z-scans indicates the presence of absorption effects [26]. The two photon absorption coefficient, β, can be calculated from the measured transmittance using numerical analysis methods. Several components of the nonlinear susceptibility can be measured by changing the polarisation (linear or circular) of the Z-scan beam.

Degenerate Four-Wave Mixing Measurements

DFWM uses four waves to extract nonlinear properties [28]. A schematic of this experiment is shown in Fig. A.6(a). This technique can be thought of as the creation of a standing wave in the sample by two counter-propagating waves of the same frequency ω [29]. A third beam, also at ω, is used to probe the amount of diffraction induced by this standing wave. The intensity of the outgoing beam, whose wave vector must be such that momentum is conserved ($\vec{k_4} = \vec{k_1} - \vec{k_2} + \vec{k_3}$), is then recorded. The third order susceptibility is related to the measured intensity by: [28]
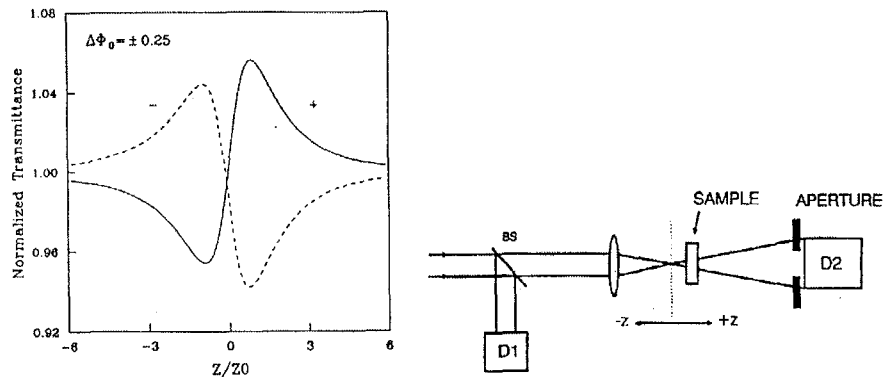
Figure A.5: (a) Experimental set-up for the Z-scan technique. The presence or absence of the aperture before detector D2 gives far-field/near-field information. From [27]. (b) Calculated z-scans for $n_2 < 0$ (dotted line) and $n_2 > 0$ (solid line) for a small aperture ($s = 0.01$) and assuming no absorption effects. From [26].

$$I_D(\omega) = \frac{\omega^2 d^2}{\epsilon_o^2 n_o^2 c^4} |\chi^{(3)}|^2 \left(\frac{1 - e^{-\alpha d}}{\alpha d} \right) e^{-\alpha d} I_1 I_2 I_3. \qquad (A.19)$$

An example of the intensity-time profile in a DFWM experiment is given in Fig. A.6(b).

Since Z-scan uses a single beam, it is much simpler than the four-beam DFWM method. However, Z-scan is very sensitive to alignment and therefore requires very carefully maintained experimental setups. Pulsed laser systems used with either Z-scan or DFWM can yield time-resolved information the induced optical nonlinearities. [30]

A.4.7 Measurements of Nonlinear Optical Coefficients

Many types of semiconductor nanocrystals have been measured for their nonlinear properties using Z-scan and DFWM experiments. Table A.1 summarises
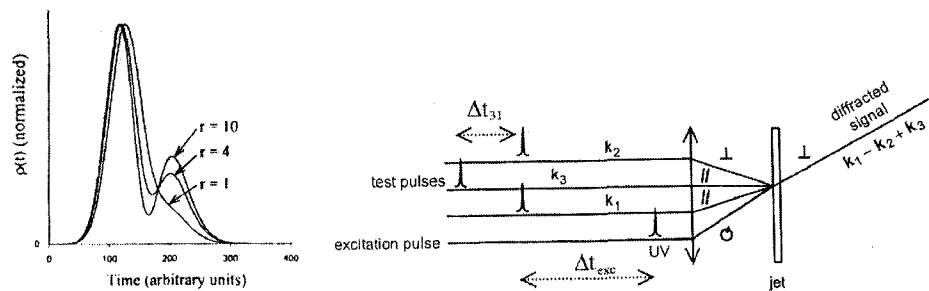
Figure A.6: (a) Schematic of the degenerate four-wave mixing technique, where all frequencies are equal. From [28]. (b) Calculated reflectivity profile of a time-resolved DFWM setup for various real and imaginary $\chi^{(3)}$ ratios r. From [30].

some of the nonlinearities measured in a variety of semiconductors by these two methods. Optical filters from Corning and Schott companies are semiconductor nanoparticles embedded in glass. Typically the semiconductors used are $Cd(S, Se)$ or $Cd(S, Se, Te)$ [31].

Aggregation effects from laser annealing are expected to affect the nonlinearity as compared with ion-implantation samples for Si nanocrystals [16]. The exciton binding energy is significantly higher in II-VI than in III-V semiconductor nanocrystals; this may cause large differences in measured optical nonlinearities between these two classes of semiconductors.

Generally, measurements of absolute nonlinearities are highly dependent on experimental conditions, even in the case of bulk materials or samples in solution [32]. However, $\chi^{(3)}$ is on the order of 10^{-23} m^2/V^2 for glass, 10^{-21} m^2/V^2 for CS_2 (an classic third order nonlinear inorganic), and 10^{-18} m^2/V^2 for nonlinear polymers [32].

Note that the various research groups have measured different nonlinear op-

tical coefficients, thereby complicating direct comparisons between experiments. The relations between the third order susceptibility $\chi^{(3)}$, the nonlinear refractive index n_2 and γ, and the absorption nonlinearity β are given by: [26]

$$\alpha = \alpha_o + \beta I, \tag{A.20}$$

$$n = n_o + n_2|E|^2/2 = n_o + \gamma I_o, \tag{A.21}$$

$$n_2(esu) = \frac{cn_o}{40\pi}\gamma(m^2/W), \tag{A.22}$$

$$Re[\chi^{(3)}] = 2n_o^2\epsilon_o c\gamma, \tag{A.23}$$

$$Im[\chi^{(3)}] = \frac{n_o^2\epsilon_o c^2}{\omega}\beta, \tag{A.24}$$

NC:host	size nm	λ_{exc} nm	τ_{pulse} ns	I_o MW/cm^2	nonlinearity	Ref.
Corning1	-	1047	-	0.07	β = 16 - 110 cm/nW	[33]
Corning2	-		-		β = 18 - 290 cm/nW	
Schott1	-		-		β = 54 - 520 cm/nW	
Schott2	-		-		β = 60 - 550 cm/nW	
CdSSe:glass	3.5 -	1060	-	-	$\mathrm{Re}[\chi^{(3)}]$ = -0.1 - -1m^2/V^2	[31]
CdSSeTe:glass	6.0		-	-	$\mathrm{Im}[\chi^{(3)}] \approx 0.1 \times 10^{-20}m^2/V^2$	
CdSe (bulk)	-	1064	-	-	β = 1400 cm/pW	[40]
	-	1320	-	-	β = 20 cm/pW	
InAs:glass [a]	3.3	633	-	0.0384	β = 0.82 cm/W	[13]
			-		$\mathrm{Im}[\chi^{(3)}]$ = 23.9 m^2/V^2	
	3.6				β = 0.26 cm/W	
			-		$\mathrm{Im}[\chi^{(3)}]$ = 7.51 m^2/V^2	
	4.1		-		β = -0.012 cm/W	
			-		$\mathrm{Im}[\chi^{(3)}]$ = -0.34 m^2/V^2	
	5.3		-		β = -0.077 cm/W	
			-		$\mathrm{Im}[\chi^{(3)}]$ = -2.21 m^2/V^2	
InP:Vycor [b]	4 - 15	850	8	340	$n_2 = 2.6 cm^2/TW, \gamma > 0$	[15]

Continued on next page.

NC:host	size	λ_{exc}	τ_{pulse}	I_o	nonlinearity	Ref.
	nm	nm	ns	MW/cm^2		
GaAs:Vycor [b]	-	1064	0.1	-	$\beta \approx 8cm/GW$	[41]
	-			-	$\gamma \approx -1.3cm^2/TW$	
	5	-	-	-	$\beta = 30cm/GW$	
	-			-	$\gamma = -5.6cm^2/TW$	[14]
GaAs (bulk)	-	-	-	-	$\beta \approx 26cm/GW$	[14, 41]
	-	-	-	-	$\gamma \approx -0.41cm^2/TW$	
Si:glass [c]	3-4	355	-	35	$\gamma = 9.6 \pm 2.5cm^2/GW$	[16]
[c]	5-6	532	-	15	$\gamma = 37 \pm 9cm^2/GW$	
[d]	4-5	355	-	6	$\gamma = 7 \pm 2cm^2/GW$	
[d]		532	-	6	$\gamma = -5.0 \pm 1.3cm^2/GW$	
[d]			-	0.03	$\gamma = -6000 \pm 1500cm^2/GW$	
Ge:glass [c]	3	800	0.0002	-	$n_2 = 0.14cm^2/TW$	[42]
			.0006	-	$n_2 = 0.30cm^2/TW$	
			.00018	$2.3\mu J/m^2$	$n_2 = 0.30cm^2/TW$	
			.0006		$n_2 = 0.90cm^2/TW$	
[a]	6	532	0.035	20 000	$n_2 = 2.6 - 8.2cm^2/TW$	[43]

Table A.1: (Continued from previous page.) *Summary of some measured nonlinear optical coefficients in II-VI, III-V and IV semiconductor nanocrystals embedded in a dielectric host, delineated by double horizontal lines. λ_{exc}, τ_{pulse} and I_o are the excitation wavelength, pulse width, and intensity, respectively. Several bulk values are included for reference.* [a]*magnetron co-sputtering* [b]*gas phase condensation* [c]*ion-implantation* [d]*laser ablation*

Inconsistencies in Table A.1 may be due to unknown or unreported sample-dependent or experiment-dependent parameters. The wavelength dependence of the nonlinearities needs to be further investigated, as well as more systematic studies on the nonlinear dependences on excitation intensity, average size and size distribution, shape and possible nanocrystal-host effects. Furthermore, numerical values were measured to differ drastically with repeated exposure to pump beams [33]. In some cases n_2 changed sign after several experiments.

Several other types of nanocrystals have been studied besides the conventional model of a two-element crystal embedded in a dielectric matrix. Porous silicon has been used as a nanoparticle-like material [34]; it contains interconnected nanometre-sized wires and dots, and so is not strictly a nanocrystal. However, since zero-dimensional confinement is evident in this material, it is included in this appendix. Porous Si is formed by HF-etching bulk silicon wafers, leaving a surface with many defect areas. Regions of nanoscale Si may be found around the etched holes in this sample. Typical sizes range from 2-5 nm. A variational approach was used to predict an enhancment in $\chi^{(3)}$ by four orders of magnitude [35]. Lettieri *et al.* measured n_2 values for various pump wavelengths: $-1.08 \pm 0.12 \times 10^{-8}$, $-3.4 \pm 0.5 \times 10^{-10}$, and $-4.8 \pm 0.6 \times 10^{-10}$ esu for $\lambda_{exc} = 532, 737$, and 1064 nm, respectively.

Insulators have been studied as nanocrystals and found to have high optical nonlinearities as well [36]. For example, nanoparticles of Fe_2O_3 were studied using the Z-scan technique. A large nonlinear coefficient of $n_2 = -800 \ cm^2/GW$ was measured using a continuous-wave $HeNe$ laser ($\lambda_{exc} = 632.5$ nm).

Finally, organic-capped semiconductor nanocrystals are being investigated for further enhancement of nonlinear optical properties [37-39]. The coupling of the Wannier-Mott excitons in the nanocrystal to the Frenkel excitons in the organic layer leads to a further nolinearity enhancement [37]. A weak confinement

regime model was used to derive the ratio of the hybrid (semiconductor + organic capping layer) to the uncapped nanocrystal:

$$\frac{P_{hybrid}^{(3)}}{P_{NC}^{(3)}} \sim \left(\frac{d_o}{a}\right)^2 \left(\frac{a_{exc}}{a_{org}}\right)^6, \tag{A.25}$$

where d_o is the thickness of the organic capping layer, a_{exc} is the exciton Bohr radii in the semiconductor nanocrystal, and a_{org} is the lattice constant for the organic layer. An enhancement of 10^6 was expected for $a_{org} \sim 5$ $\overset{\circ}{A}$. Recently, a sample of CdS nanocrystals in a polydiacetylene host was studied experimentally [44]. Alternatively, the nanocrystals could be capped with another organic molecule, thiophenol. At an excitation wavelength of 530 nm, $n_2 = 3 \times 10^{-8} cm^2/MW$ was measured for the uncapped sample, and $n_2 = 11 \times 10^{-8} cm^2/MW$ for the capped sample. It is interesting to note that polydiacetylene and its derivatives also exhibit nonlinear optical effects. The constructive addition of nonlinear properties of the host and nanocrystalline material appears to be a possible method by which to improve optical nonlinearities.

Bindra *et al.* analysed the Z-scan technique for the case of quantum dots and found several inconsistencies [45]. In particular, two-photon absorption ($\chi^{(5)}$) processes were found to interfere with the Z-scan interpretation based on the original Z-scan work by Sheik-Bahae *et al.* [26]. While this was addressed in the original demonstration of the Z-scan technique, it is often disregarded in the interpretation of Z-scan measurements. This is indicative of the ambiguity of the measurements of nonlinear optical coefficients at the present time.

A.4.8 Comparison of Theoretical and Experimental Results

Real systems are much more complicated than the simple two-level model described in Sec. A.4.1, making comparison between theory and experiment dif-

ficult. Indeed, very few groups have attempted to bridge this gap. In one study, Cotter *et al.* [31] studied the Corning and Schott glasses referred to in Table A.1. Their experiments showed that for excitation energies $\hbar\omega$ less than the absorption edge E_{abs}, the real part of $\chi^{(3)} < 1$ in all cases. A two-band model using bulk effective electron and hole masses and the Stark Effect was sufficient to reproduce their experimental results to an order of magnitude (Fig. A.7). Sample-dependent parameters such as stoichiometry, size distribution, and volume fraction fluctuations were neglected. Note that $Re[\chi^{(3)}] \gg Im[\chi^{(3)}]$, from the first data set in Table A.1. The imaginary third order susceptibility is significant only for higher pump energies ($\hbar\omega > E_{abs}/2$), and the magnitude is significant compared with the host ($Re[\chi^{(3)}]_{host} \sim 10^{-22}m^2/V^2$). Most importantly, their relatively simple model gave $Re[\chi^{(3)}] < 1$ for a range of pump energies and nanocrystal sizes.

A.5   Photobleaching and Induced Absorption

While this review has focussed on the susceptibility representation to discuss optical nonlinearities, *photobleaching* and *induced absorption* are more widely investigated in publications on optical nonlinearities in semicondcutor nanocrystals. These two processes are presented in this section.

Photobleaching occurs in high intensity experiments when possible absorption channels are saturated, allowing an increase in probe signal when compared with the equilibrium case [46]. In other words, the presence of an exciton changes the excitation spectrum for a second exciton; this exciton-exciton Coulomb interaction is responsible for bleaching. Peyghambariam *et al.* [46] argued that mechanisms other than a common electronic state may contribute to photobleaching.

Induced absorption occurs when two excitons are created from one pump and
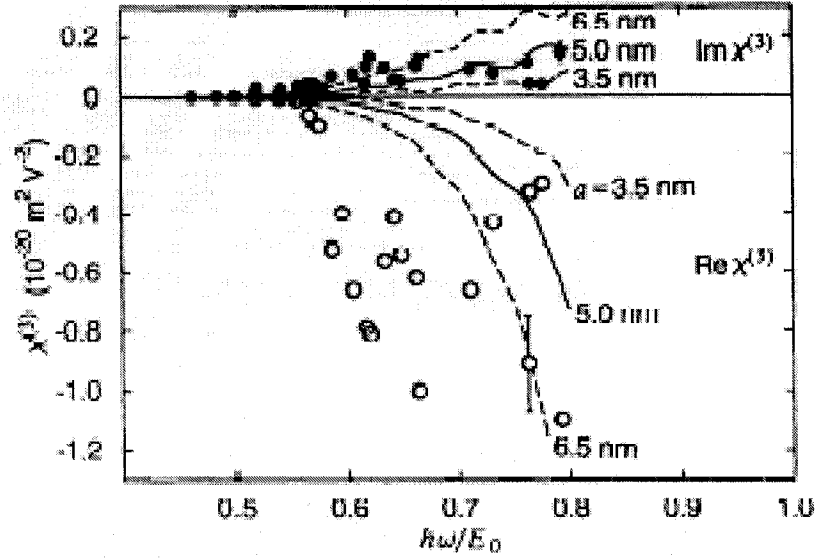
Figure A.7: Comparison of measured (circles) and calculations (lines) $\chi^{(3)}$ for $Cd(S, Se, Te)$ nanocrystals in a glass host. The numbers to the right of the data indicates the average nanocrystal radius used in the calculations. (From [31])

one probe photon [46]. The first exciton bleaches an absorption state, allowing new transitions for the second exciton. These transitions can be observed by monitoring the differential transmission in pump-probe experiments [47]. Two bleaching bands (positive differential transmission) and a single induced absorption band (negative differential transmission) can be seen in Fig. A.8(a).

The two-level model on which the theoretical development of the nonlinear susceptibility in Section A.4 was based is oversimplified. To explain photobleaching and induced absorption, a six-level system must be introduced [46, 47] to include one ground state, two one-exciton states, and three two-exciton states (Fig. A.8(b)). This was mentioned earlier to describe the susceptibility in Sec. A.4.3. The one-exciton states include the 1s-1s transition $|1s_e, 1s_h\rangle$ and the

1p-1p transition $|1p_e, 1p_h\rangle$. Since p-state transitions are higher in energy than s-state transitions, the shorter wavelength bleaching band is attributed to the $|1p_e, 1p_h\rangle$ state, while the longer wavelength band corresponds to the $|1s_e, 1s_h\rangle$ state in Fig. A.8(a). The states are coupled through dipole-moments [46], and by assuming equal energy spaces for each of the transitions and the same population decay rates, third-order nonlinearities were computed. Biexcitonic states considered in the derivation couple $1s$ and $1p$ electron-hole pairs to give three possible states: $|1p_e, 1p_h; 1p_e, 1p_h\rangle$, $|1s_e, 1s_h; 1p_e, 1p_h\rangle$, and $|1s_e, 1s_h; 1s_e, 1s_h\rangle$ in decreasing energy. The calculations reproduce the essential features observed in experimental results, as shown in Fig. A.8(a) and (c), indicating that a discrete six-level system can successfully model the effects of photobleaching and induced absorption.
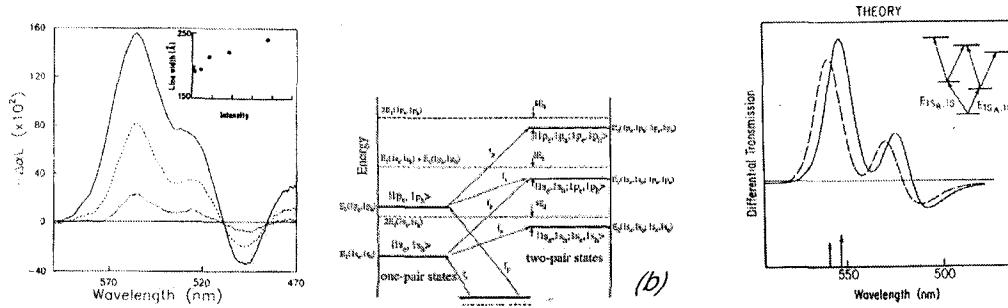
Figure A.8: (a) Photobleaching (positive differential transmission) and induced absorption (negative differential transmission) are observed in experiment. From [46]. (b) A six-level model, which includes bi-excitonic states, are coupled by dipole transitions as indicated by arrows. From [47]. (c) Calculations using the six-level model reproduce experimental results. From [46].

The $|1p_e, 1p_h\rangle$ level was observed to recover from bleaching faster than the lower energy state $|1s_e, 1s_h\rangle$ [46]. The p-state wavefunctions extend further past

the semiconductor-dielectric barrier than the s-state wavefunctions, and therefore the former can recombine faster. Time-resolved experiments support this conjecture [46]. Trapping sites from Se anions at the surfaces of $CdSe$ nanocrystals in this experiment are the proposed recombination channel for the $|1p_e, 1p_h\rangle$ excitons. Furthermore, Klimov, Hunsche, and Kurz calculated [47] a much larger bi-exciton binding energy for nanocrystals than for bulk $CdSe$, ranging from 0.8 to 1.4 times the binding energy within a single exciton.

The amount of photobleaching and inducted absorption was found to be correlated with injected carrier density (*i.e.* pump intensity) [48]. However, Tamulaitis *et al.* attribute a broad-band induced absorption in PbS (extending from 1.45 beyond 2.05 eV) to electronic transitions to higher excited states rather than to biexcitonic states [48]. Because the induced absorption band for PbS is much broader than that observed in the $CdSe$ mentioned above, this conclusion is not necessarily inconsistent with those mentioned earlier. [46, 47]. Tamulaitis *et al.* were able to dismiss other possible mechanisms for induced absorption, including: ensemble excitons and dense electron-hole plasmas, thermal processes, Auger processes, and the Stark effect, and conclude that higher electronic excited states can be responsible for induced absorption.

A.6 Future Directions

Quantum confinement of semiconductors has been shown both theoretically and experimentally to have impressive optical nonlinear properties. Better computation of expected results would help in furthering this research. An understanding of the effect of impurities on optical nonlinearities is necessary before these systems can be fully understood. More investigation into the impact of multiple excitation levels should be considered in simulations and theoretical models.

It is interesting to note that most of this literature has been done with

nanocrystals embedded in amorphous material (with silica being the most popular). Much of the theoretical work to date has also concentrated on isotropic samples, where the nanocrystals are not crystallographically aligned with one another. Since ion implantation allows for the formation of nanocrystals in a crystalline material (e.g. alumina or sapphire, Al_2O_3) [4], this is a promising technique to form crystallographically aligned quantum dots. It would be interesting to conduct a systematic study of the nonlinear optical properties of these crystallographically aligned nanocrystals. One might expect second order nonlinearities to be present in such ordered samples if the semiconductor material has no inversion symmetry. Since the second order susceptibility in bulk semicondcutors [49] are on the same order of magnitude as those of the measured third order values in nanocrystals, one may expect enhanced $\chi^{(2)}$ in nanoparticle samples. This is promising for potential applications research.

Surface effects need to be well-investigated since nearly 1/3 of the atoms in a nanocrystal are in contact with the host. Furthermore, the measurements summarised here include only ensemble-averaged results. Other types of measurements, such as photoluminescence experiments, have used apertures to single out individual nanocrystals [50]. It would be interesting to apply this technique to study nonlinear optical coefficients of single quantum dots. However, the weak intensity of the signal from a single quantum dot may make these experiments very difficult. Better enhancement of the quantum and electromagnetic effects in nanocrystals would be achieved if the intrinsic broadening could be reduced [9]; narrower size distributions and better surface chemistry are needed to take advantage of these effects. Interfacial doping of $GaAs/AlGaAs$ quantum dots with Si ions has been modeled as a method to control level broadening due to size distribution [51].

Within the scope of this appendix, many related topics could not be covered.

The origins of photoluminescence, for instance, is an interesting open question [4, 52]. As well, early experiments focused on $CuCl$ and $CuBr$ nanocrystals, which were not discussed in this appendix [3]. Furthermore, nonlinear optical properties of metal nanocrystals is an entire review itself, and so was not dealt with here. It would also have been interesting to investigate the time-dependences of these nonlinearities. Time-resolved Z-scan and DFWM experiments have already been performed [41–43]; the important time constants for these processes may help elucidate the underlying physics responsible for optical nonlinearities in these materials.

While more work is necessary before the processes driving these nonlinearities are understood, the investigation to date has provided promising results. The study of semiconductor nanocrystals is important from a fundamental standpoint as well as from a technological point of view. With enhanced nonlinearities over bulk values, potential device applications are motivating the fundamental research into this new physical size regime [31]. Possible quantum dot lasers using electroluminescence are currently investigated in organic-capped CdS and $CdSe$ quantum dot structures [53], where the luminescent energy was found to be tunable over a few hundred meV using varying bias voltages. As well, third order optical nonlinearities have been used as a probe to study interface effects [27]. Further enhancement of optical nonlinearities by embedding quantum confined crystals in a nonlinear host is also of great techological interest [44].

To conclude, the investigation of nonlinear optical properties in semiconductor nanocrystals is a current and exciting field of investigation. With its enhanced nonlinearities over bulk values, and with more emerging techniques to produce better, more consistent samples, one can imagine optical devices using these materials in the near future.

Bibliography

[1] Gaponenko, S.V., *Optical Properties of Semiconductor Nanocrystals*, Cambridge University Press, Cambridge, U.K., (1998).

[2] Meldrum, A., private communication.

[3] Flytzanis, C., F. Hache, M.C. Klein, D. Ricard, and Ph. Roussignol, *Nonlinear Optics in Composite Materials: I. Semiconductor and Metal Crystallites in Dielectrics*, Elsevier Science Publishers, (1991).

[4] Meldrum, A., C.W. White, L.A. Boatner, I.M. Anderson, R.A. Zuhr, E. Sonder, J.D. Budai, and D.O. Henderson, "Microstructure of sulfide nanocrystals formed by ion-implantation", *Nuc. Instr. Meth. B*, **148**, 957-963, (1999).

[5] Efros, Al.L., and A. L. Efros, "Interband absorption of light in a semiconductor sphere", *Sov. Phys. Semicond.* **16** (7), 772-778, (1982).

[6] Belleguie, L., and L. Banyai, "Third-order nonlinear susceptibility of large semiconductor microcrystallites", *Phys. Rev. B* **47** (8), 4498-4507, (1993).

[7] Hanamura, E., "Very large optical nonlinearity of semiconductor microcrystallites", *Phys. Rev. B* **37** (3), 1273-1279, (1988).

[8] Schmitt-Rink, S., D.A.B. Miller, and D.S. Chemla, "Theory of the linear and nonlinear optical properties of semiconductor microcrystallites", *Phys. Rev. B* **35** (15), 8113-8125, (1987).

[9] Brus, L., "Quantum crystallites and nonlinear optics", *Appl. Phys. A* **53**, 465-474, (1991).

[10] Wamura, T., Y. Masumoto, and T. Kawamura, "Size-dependent homogeneous linewidth of Z_3 exciton absorption spectra in CuCl microcrystals", *Appl. Phys. Lett.* **59** (14), 1758-1760, (1991).

[11] Brett, M., *EE602 Thin Film Technology*, class notes (1999).

[12] Shi, J.Z., K.G. Zhu, Q.Q. Zheng, L.D. Zhang, L. Ye, J.X. Wu, and J. Zuo, "Ultraviolet (340-390 nm), room temperature, photoluminescence from InAs nanocrystals embedded in SiO_2 matrix", *Appl. Phys. Lett.* **70** (19), 2586-2588, (1997).

[13] Shi, J., K. Zhu, and L. Zhang, "Nonlinear optical absortpion of InAs nanocrystals embedded in SiO_2 thin films", *Solid State Commun.* **110**, 645-649, (1999).

[14] Justus, B.L., R.J. Tonucci, and A.D. Berry, "Nonlinear optical properties of quantum-confined GaAs nanocrystals in Vycor glass", *Appl. Phys. Lett.* **61** (26), 3151-3153, (1992).

[15] Hendershot, D.G., D.K. Gaskill, B.L. Justus, M. Fatemi, and A.D. Berry, "Organometallic chemical vapor deposition and characterization of indium phosphide nanocrystals in Vycor porous glass", *Appl. Phys. Lett.* **63** (24), 3324 (1993).

[16] Vijayalakshmi, S., H. Grebel, Z. Iqbal, and C.W. White, "Artificial dielectrics: Nonlinear properties of Si nanoclusters formed by ion implantation in SiO_2 glassy matrix", *J. Appl. Phys.* **84** (12), 6502-6506, (1998).

[17] Willmott, P.R., and J.R. Huber, "Pulsed laser vaporization and deposition", *Rev. Mod. Phys.* **72** (1), 315-328, (2000).

[18] Herz, K., G. Bacher, A. Forchel, H. Straub, G. Brunthaler, W. Faschinger, G. Bauer, and C. Vieu, "Recombination dynamics in dry-etched (Cd,Zn)Se/ZnSe nanostructures: Influence of exciton localization", *Phys. Rev. B* **59** (4), 2888-2893, (1999).

[19] Bransden, B.H., and C.J. Joachim, *Physics of Atoms and Molecules*, Longman Scientific and Technical, Essex, England (1983).

[20] Ashcroft, N.W., and N.D. Mermin, *Solid State Physics*, Saunders College Publishing, Orlando, FL (1976).

[21] Ekimov, A.I., and A. A. Onushchenko, *Sov. Phys. Semicond.* **16** (7), 775 (1982).

[22] Huang, K., and A. Rhys, "Theory of light absorption and non-radiative transitions in F-centres", *Proc. Royal Soc. London A* **204** (1078), 406-423, (1950).

[23] Spiegelberg, C., F. Henneberger, and J. Puls, "Spectral hole-burning in quantum confined semiconductor microcrystals", *Superlatt. Microstruct.* **9** (4), 487-491, (1991).

[24] Uhrig, A., L. Banyai, S. Gaponenko, A. Worner, N. Neuroth, C. Klingshirn, "Linear and nonlinear optical studies of $CdS_{1-x}Se_x$ quantum dots", *Z. Phys. D* **20**, 345-348, (1991).

[25] Brus, L., "Electron-electron and electron-hole interactions in small semiconductor crystallites: The size dependence of the lowest excited electronic state", *J. Chem. Phys.* **80** (9), 4403 (1984).

[26] Sheik-Bahae, M., A.A. Said, T.H. Wei, D.J. Hagan, and E.W. van Stryland, "Sensitive measurement of optical nonlinearities using a single beam", *IEEE J. Quantum Elec.* **26** (4), 760-769, (1990).

[27] Yang, L., D.H. Osborne, R.F. Haglund, Jr., R.H. Magruder, C.W. White, R.A. Zuhr, and H. Hosono, "Probing interface properties of nanocomposites by third-order nonlinear optics" *Appl. Phys. A* **62**, 403-415, (1996).

[28] Rulliere, C. (ed.) *Femtosecond Laser Pulses: Principles and Experiments*; Springer-Verlag, Berlin, Germany (1999); Ch.8.

[29] Butcher, P.N. and D. Cotter, *The elements of Nonlinear Optics*, Cambridge University Press, Cambridge, U.K. (1990), p188-196.

[30] Kurzyk, M.G., and C.W. Dirk (ed.), *Characterization, Techniques, and Tabulations for Organic Nonlinear Optical Materials*, Marcel Dekker, Inc., New York, NY (1998).

[31] Cotter, D., M.G. Burt, and R.J. Manning, "Below-band-gap third-order optical nonlinearity of nanometer-size semiconductor crystallites", *Phys. Rev. Lett.* **68** (8), 1200-1203, (1992).

[32] Agullo-Lopez, F., J.M. Cabrera, and F. Agullo-Rueda, *Electrooptics: Phenomena, Materials, and Applications*, Academic Press, New York, NY (1994).

[33] Duarte, A.S., H.L. Fragnito, and E. Palange, "Light induced permanent modifications of the nonlinear optical properties of semicondcutor doped glasses", *Solid State Commun.* **100** (7), 463-466, (1996).

[34] Lettieri, S. P. Maddalena, L.P. Odierna, D. Ninno, V. la Ferrara, and G. di Francia, "Measurements of the nonlinear refractive index of free-standing porous silicon layers at different wavelengths", *Philos. Mag. B* **81** (2), 133-139, (2001).

[35] Lettieri, S., O. Fiore, P. Maddelena, A. Morra, and D. Ninno, "Third-order nonlinear refraction in porous silicon: theory versus experiment", *Philos. Mag. B* **80** (4), 587-597, (2000).

[36] Yu, B.L., C.S. Zhu, and F.X. Gan, "Large nonlinear optical properties of Fe_2O_3 nanoparticles", *Physica E* **8**, 360-364, (2000).

[37] Engelmann, A., V.I. Yudson, and P. Reineker, "Enhanced optical nonlinearity of hyrid excitons in an inorganic semiconducting quantum dot covered by an organic layer", *Phys. Rev. B* **57** (3), 1784-1790, (1998).

[38] Mattoussi, H., L.H. Radzilowski, B.O. Dabbousi, D.E. Fogg, R.R. Schrock, E.L. Thomas, M.F. Rubner, and M.G. Bawendi, "Composite thin films of CdSe nanocrystals and a surface passivating/electron transporting block copolymer: Correlations between film microstructure by transmission electron microscopy and electroluminescence", *J. Appl. Phys.* **86** (8), 4390-4399, (1999).

[39] Mylnikov, V.S., *Advances in Polymer Science 115: Photoconducting Polymers*; Springer-Verlag, Berlin, Germany (1994).

[40] Dmitriev, V.G., G.G. Gurzadyan, D.N. Nikogosyan, *Handbook of Nonlinear Optical Crystals*, Second Edition, Spring-Verlag, Berlin (1997).

[41] Dvorak, M.D., B.L. Justus, and A.D. Berry, "Pump/probe Z-scan studies of GaAs nanocrystals grown in porous glass", *Opt. Commun.* **116**, 149-152, (1995).

[42] Dowd, A., M. Samoc, B. Luther-Davies, and R.G. Elliman, "Nonlinear optical properties of semiconducting nanocrystals in fused silica",*Nuc. Instr. Meth. B* **148**, 964-968, (1999).

[43] Jie, Y.X., Y.N. Xiong, A.T.S. Wee, C.H.A. Huan, and W. Ji, "Dynamics of optical nonlinearity of Ge nanocrystals in a silica matrix", *Appl. Phys. Lett.* **77** (24), 3926-3928, (2000).

[44] Schwerzel, R.E., K.B. Spahr, J.P. Kurmer, V.E. Wood, and J.A. Jenkins, "Nanocomposite photonic polymers. 1. Third-order nonlinear optical properties of capped cadmium sulfide nanocrystals in an ordered polydiacetylene host", *J. Phys. Chem. A* **102**, 5622-5626, (1998).

[45] Bindra, K.S., S.M. Oak, and K.C. Rustagi, "Intensity dependence of Z-scan in semiconductor-doped glasses for separation of third and fifth order contributions in the below band gap region", *Opt. Commun.* **168**, 219-225, (1999).

[46] Peyghambarian, B. Fluegel, D. Hulin, A. Migus, M. Joffre, A. Antonetti, S.W. Koch, and M. Lindberg, "Femtosecond optical nonlinearities of CdSe quantum dots", *IEEE J. Quantum Electr.* **25** (12), 2516-2522, (1989).

[47] Klimov, V., S. Hunsche, and H. Kurz, "Biexciton effects in femtosecond nonlinear transmission of semiconductor quantum dots", *Phys. Rev. B* **50** (11), 8110-8113, (1994).

[48] Tamulaitis, G., V. Gulbinas, G. Kodis, A. Dementjev, L. Valkunas, I. Motchalov, and H. Raaben, "Optical nonlinearities of glass doped with PbS nanocrystals", *J. Appl. Phys.* **88** (1), 178-182, (2000).

[49] Boyd, R.W., *Nonlinear Optics*, Academic Press, Boston, MA (1992).

[50] Zwiller, V., M.E. Pistol, D. Hessman, R. Cederstrom, W. Seifert, and L. Samuelson, "Time-resolved studies of single semiconductor quantum dots", *Phys. Rev. B* **59** (7), 5021-5025, (1999).

[51] Shi, J.M., V.N. Freire, and G.A. Farias, "Energy level broadening control in quantum dots by interfacial doping", *Solid State Commun.* **113**, 115-119, (2000).

[52] White, C.W., J.D. Budai, S.P. Withrow, J.G. Zhu, E. Sonder, R.A. Zuhr, A. Meldrum, D.M. Hembree, Jr., D.O. Henderson, and S. Prawer, "Encapsulated semiconductor nanocrystals formed in insulators by ion beam synthesis", *Nucl. Instr. Meth. B* **141** 228-240, (1998).

[53] Klingshirn, C., "Linear and nonlinear optics of wide-gap II-VI semiconductors", *Phys. Stat. Sol. (b)* **202**, 857-871, (1997).

Appendix B

Information on Crystalline ZnTe

This Appendix is a collection of information relating to the crystal $ZnTe$, which is used to generate and detect THz emission in the Ultrafast Spectroscopy Laboratory.

B.1 $ZnTe$ Thickness

Various thicknesses of $ZnTe$ were sampled for the THz emitter and detector. The least noisy THz traces were obtained with a 0.5 mm $ZnTe$ emitter and a 2 mm $ZnTe$ detector. However, the thicker detector decreases the bandwidth of the THz pulses, cutting off the high frequency components. Comparisons of the bandwidths and waveforms are given in Figure B.1.

B.2 Optical Properties

Nahata *et. al.* [57] gives for refractive indices in $ZnTe$ for optical wavelengths, λ (in μm),

$$n^2 = 4.27 + 3.01\lambda^2/(\lambda^2 - 0.142), \quad\quad\quad \text{(B.1)}$$
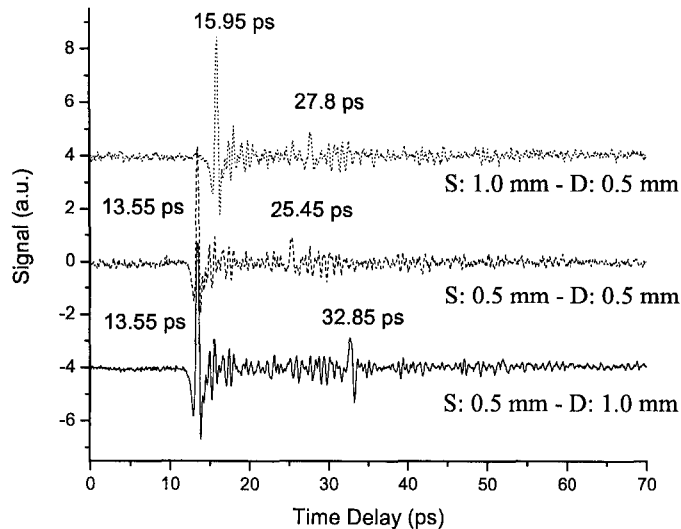
Figure B.1: Comparison of THz waveforms for various $ZnTe$ thicknesses used in the optical rectification and electro-optic sampling processes. The signals are offset vertically for clarity. Times for the main peak and reflections in the detector crystal are labelled next to the peaks. S: source $ZnTe$ crystal thickness, D: detector $ZnTe$ crystal thickness.

and for far-infrared frequencies, f (in THz),

$$n^2 = (289.27 - 6f^2)/(29.16 - f^2). \qquad (B.2)$$

The two-photon fluorescence of $ZnTe$ peaks at 554 nm, measured using a TRIAX spectrometer. This is shown in Figure B.2. The two-photon fluorescence appears on the crystal as a bright green spot when illuminated with a wavelength of

Table B.1: Physical properties of crystalline *ZnTe*, from http:// www.princesci.com/ crystal/ zinctel.html.

density	6.34 g/cm^3	melting point	1568 °C
hardness	6 Mhos	thermal conductivity	108 mWcm^{-1}K^{-1}
band gap (300 °C)	2.26 eV	specific heat capacity	264 Jkg^{-1}K^{-1}
Hall mobility (300 K)	130 cm^{2}V^{-1}s^{-1}	specific resistivity	$> 1 \times 10^5$ Ω·cm
Hall mobility (80 K)	2600	effective hole mass	0.6 m$_e$
space group	$\bar{4}$3m	lattice constant	6.1034 Å

800 nm. The spot makes for easy alignment of the THz and gating beams on the *ZnTe* detection crystal. The polyethylene beam block can be removed from the generation 800 nm beam. The green spot from the detection beam can then be moved so as to overlap with that from the generation beam on the surface of the detection crystal. Be sure, however, to decrease the intensity of the generation beam as it may cause damage when focussed onto the *ZnTe* detection crystal.
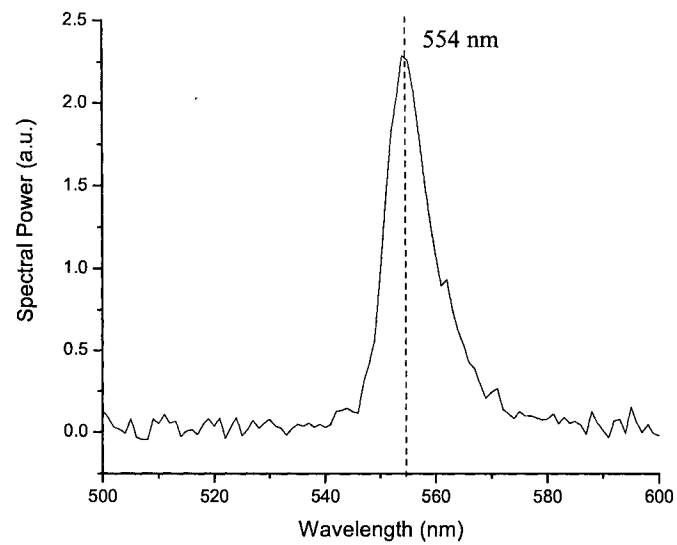
Figure B.2: Two-photon fluorescence from a *ZnTe* crystal at 554 nm (pumped at 800 nm). The spectrum was acquired using a TRIAX spectrometer. This fluorescence is visible on the crystal face with the naked eye, and appears as a light green spot.